Production of Titanium Metal by an Electrochemical Molten Salt Process

Submitted in partial fulfillment of the requirements for

the degree of

Doctor of Philosophy

in

Materials Science and Engineering

Farzin Fatollahi-Fard

B.S., Mechanical Engineering, University of California, Berkeley
M.S., Materials Science and Engineering, Carnegie Mellon University

Carnegie Mellon University

Pittsburgh, PA

May, 2017

0.1 Abstract

Titanium production is a long and complicated process. What we often consider to be the standard method of primary titanium production (the Kroll process), involves many complex steps both before and after to make a useful product from titanium ore. Thus new methods of titanium production, especially electrochemical processes, which can utilize less-processed feedstocks have the potential to be both cheaper and less energy intensive than current titanium production processes. This project is investigating the use of lower-grade titanium ores with the electrochemical MER process for making titanium via a molten salt process. The experimental work carried out has investigated making the MER process feedstock (titanium oxycarbide) with natural titanium ores—such as rutile and ilmenite—and new ways of using the MER electrochemical reactor to "upgrade" titanium ores or the titanium oxycarbide feedstock. It is feasible to use the existing MER electrochemical reactor to both purify the titanium oxycarbide feedstock and produce titanium metal.

0.2 Acknowledgments

The information, data or work presented herein was funded in part by the Advanced Research Projects Agency-Energy (ARPA-E), U.S. Department of Energy, under Award Number DE-AR0000516.

The author acknowledges use of the Materials Characterization Facility at Carnegie Mellon University supported by grant MCF-677785.

Special thanks to the creators, programmers, and maintainers of the software used to conduct this research. Image analysis was performed with ImageJ[1]. X-ray diffraction analysis and compound identification was performed using QualX[2].

Extra special thanks to the creators of FactSage[3], as well as Cao et al. for optimizing the Ti-C-O system[4].

The author would like to thank those who provided us with various samples: Professor Xuewei Lyu for providing us with a sample of Panzhihua ilmenite mineral sand, Iluka for providing us with some Australian rutile and leucoxene samples, and Rio Tinto Iron and Titanium for providing us with some ilmenite, titaniferous slag, and upgraded slag samples.

I would like to thank my advisor, Professor P. C. Pistorius for providing invaluable support and guidance throughout this project. Additionally, I would like to acknowledge the support and assistance of Professor Jie Dang, who performed research parallel to my own during his visit to CMU from 2014-2015.

The help and suggestions of Dr. James Withers of ATS-MER LLC. have helped us investigate

[1] Caroline A Schneider, Wayne S Rasband, and Kevin W Eliceiri. "NIH Image to ImageJ: 25 years of image analysis". In: *Nature Methods* 9.7 (2012), pp. 671—675. doi: 10.1038/nmeth.2089

[2] Angela Altomare et al., "QUALX2.0: a qualitative phase analysis software using the freely available database POW_ COD". In: *J. Appl. Crystallogr.* 48.2, pp. 598—603, doi: 10.1107/S1600576715002319

[3] Christopher W. Bale et al. "FactSage thermochemical software and databases". In: *Calphad* 26.2 (2002), pp. 189–228. doi: 10.1016/S0364-5916(02)00035-4

[4] Zhanmin Cao et al. "Critical Evaluation and Thermodynamic Optimization of the Ti-C-O System and Its Applications to Carbothermic TiO2 Reduction Process". In: *Met. Trans. B* 46.4, pp. 1782–1801. doi: 10.1007/s11663-015-0344-8

new avenues of research that have greatly benefited this project.

I would like to thank the MSE staff, especially Roxann Eckman, Adam Wise, Jason Wolf, Elizabeth Clark, William Pingitore, and Tom Nuhfer for their invaluable help, as well as other CMU staff who have assisted this project, mainly Lawrence Hayhurst (ChemE) and Bernard Carter (Drama) for fabricating many of the reactor parts.

I would also like to acknowledge all the members of the Pistorius Research Group—especially Dr. Jorge Gibson for help explaining reaction kinetics and letting me use his nitrogen tank (despite his misgivings towards my new methods for ironmaking).

Last, but not least, I would like to acknowledge the help and support of my friends and family, especially when they provided me with food! Also Uma the cat, who still hates me.

Contents

List of Tables

List of Figures

Chapter 1

Introduction

Titanium metal is currently made using the Kroll process, developed by Wilhelm Kroll [1] in the 1940s. However, it is widely reported that Kroll himself said that his process was inefficient and would likely be replaced by an electrochemical process. Although many different electrochemical processes have been developed, none have been able to compete with the Kroll process in terms of large-scale commercialization yet. This short introduction will describe the Kroll process and other electrochemical processes (including the MER process, which is the focus of this research).

1.1 The Kroll Process

The Kroll process uses titanium(IV) chloride ($TiCl_4$, or often referred to as "tickle" in industry)—it does not directly use titanium ores. In order to produce $TiCl_4$, titanium ores with low levels of impurities need to be put through a process called chlorination. Only certain grades of ores can be used in chlorination, such as very high-grade titaniferous slags, leucoxene mineral sands, and natural and synthetic rutile (TiO_2)—these will be discussed in more detail in Chapter 6.

While the main point of chlorination is to convert the titanium dioxide in the ore to titanium(IV) chloride—using a carbo-chlorination reaction described in Reaction (1.1)—it also serves the function of removing most of the impurity elements as well. The chlorination process chlorinates most of the elements in the raw ore, resulting in what is called "crude" $TiCl_4$, and as such it contains impurities such as $SiCl_4$, $FeCl_3$, and $AlCl_3$ [1, 2]. These impurity chlorides can be removed, using a careful sequence of distillation and precipitation, yielding purified titanium(IV) chloride, as shown in Figure 1.1.

$$TiO_2 + 2\,Cl_2 + 2\,C \longrightarrow TiCl_4 + 2\,CO \qquad (T = 800 - 1200\,^\circ C) \qquad (1.1)$$

After pure titanium(IV) chloride is ready, the next step is to begin the actual Kroll process,

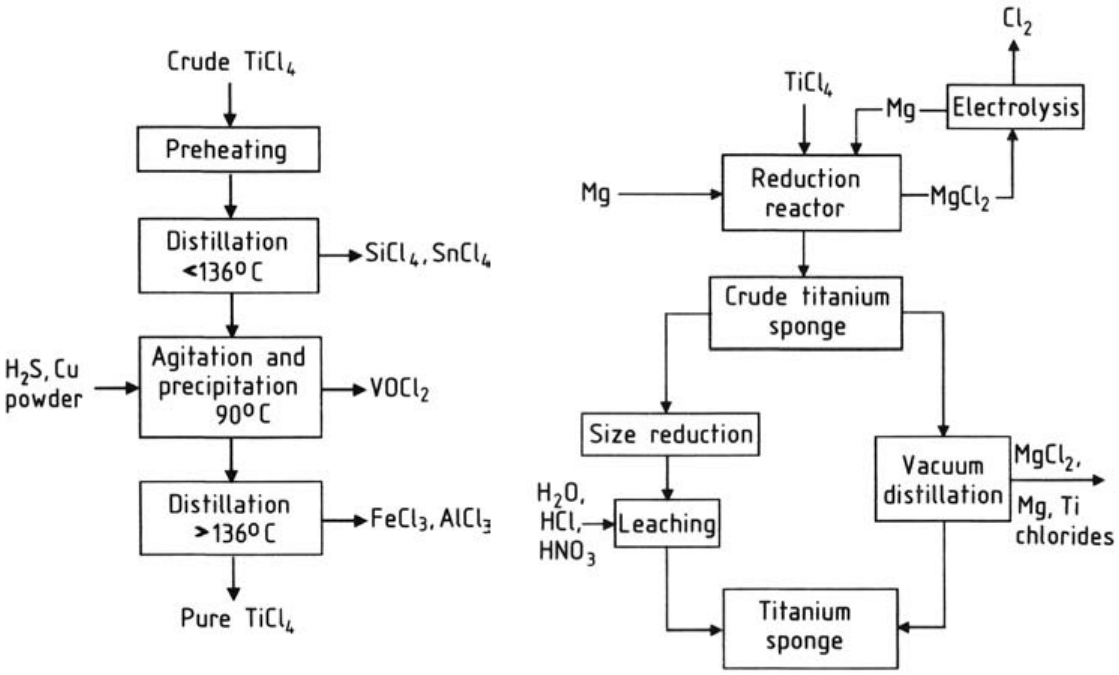

Figure 1.1: Schematic of $TiCl_4$ purification (left) and the Kroll process (right) [1].

where $TiCl_4$ gas is bubbled into a sealed stainless steel vessel containing molten magnesium. The resulting reaction (Reaction (1.2)), produces solid titanium "sponge" and magnesium chloride ($MgCl_2$). After the reaction is complete, the sponge is removed from the reactor vessel, and the magnesium chloride needs to be removed. This often entails either washing

accompanied by leaching and/or vacuum distillation to remove any remaining chlorides. This sponge is then ready to be further processed (i.e. remelted and alloyed) into usable titanium products. This process is also outlined in Figure 1.1

$$\mathrm{TiCl}_{4(g)} + 2\,\mathrm{Mg}_{(l)} \longrightarrow \mathrm{Ti}_{(s)} + 2\,\mathrm{MgCl}_{2(l)} \qquad (\mathrm{T} = 850 - 950\,^{\circ}\mathrm{C}) \qquad (1.2)$$

It is interesting to note that while the above description of the process makes it seem like the process is purely chemical, it is in fact electrochemical in nature. The Kroll process is actually an electronically-mediated reaction, so the reaction takes place due to charge transfer with the reactor vessel itself [3]—magnesium oxidation and titanium reduction actually occur at different sites.

1.2 The FFC Process

One of the first electrochemical processes for titanium production that received widespread attention was the FFC (Fray-Farthing-Chen) Process [4]. The process is essentially an electro-deoxidation process. TiO_2 pellets are placed into a calcium chloride ($CaCl_2$) electrolyte on a conductive cathode. When the correct potential is applied, the oxygen from the titanium is transferred to the electrolyte as oxygen anions, reducing the titanium to metal through several intermediate phases [5]. At the anode, oxygen anions react with the graphite anode, and leave the system as CO or CO_2. After all the oxygen leaves the system, only titanium will remain at the cathode.

While this is an interesting process, it has a few issues [6]. Attaining low oxygen concentrations in the titanium product relies on solid-state diffusion. Given the high solubility of oxygen in titanium, it is not easy to reach low oxygen levels usually required for most titanium alloys. Dissolution of CO_2 at the anode and subsequent reduction at the cathode further lowers current efficiency [7, 8]. Also, the potentials required for this reaction to occur

is near the decomposition potential of the calcium chloride electrolyte. The feedstock for FFC needs to be pure (the process has traditionally used TiO_2 pigments). Recent efforts to use other materials [9] have shown that any impurity elements present in the material will also be deoxidized and would eventually diffuse into and contaminate the titanium product.

1.3 The MER Process

The MER process was developed by Materials and Electrochemical Research (MER) Corporation [10, 11, 12, 13, 14, 15, 16], and has been studied extensively in the literature [17, 18, 19] under different names, such as the Chinuka process [20] and the USTB process [21, 22, 23]. The process begins with a source of titanium dioxide, which is then reduced with carbon in an inert atmosphere (usually argon) to produce a material known as titanium oxycarbide (Ti_2OC) by Reaction (1.3). This titanium oxycarbide is pressed into a pellet and inserted as an anode into a molten salt electrolyte (usually eutectic NaCl-KCl) in an "anode basket" made of an electrochemically inert but conductive material, such as graphite. Titanium oxycarbide is electrically conductive, and when the right potential is applied, it can begin to dissolve, putting titanium ions into solution and producing carbon monoxide, as per Reaction (1.4). With the right cathode potential, titanium ions can be plated out as a cathode deposit, as per Reaction (1.5). Put together Reactions (1.4) and (1.5) yield the full cell-reaction, shown by Reaction (1.6) (potentials were calculated from Gibbs free energy and the the Nernst equation). The use of titanium oxycarbide effectively removes both carbon and oxygen from the reactor, unlike previous similar attempts using titanium carbide anodes [24].

$$2\,TiO_2 + 4\,C \longrightarrow Ti_2OC + 3\,CO \qquad (T > 1300\,^{\circ}C) \tag{1.3}$$

$$\mathrm{Ti_2OC} + 4\,\mathrm{Cl^-}\,2 \longrightarrow 2\,\mathrm{TiCl_2} + \mathrm{CO} + 4\,\mathrm{e^-} \qquad (\mathrm{V_{Cl_2}} = -0.61\,\mathrm{V}) \tag{1.4}$$

$$2\,\mathrm{TiCl_2} + 4\,\mathrm{e^-} \longrightarrow 2\,\mathrm{Ti} + 4\,\mathrm{Cl^-} \qquad (\mathrm{V_{Cl_2}} = -1.79\,\mathrm{V}) \tag{1.5}$$

$$\mathrm{Ti_2OC} \longrightarrow 2\,\mathrm{Ti} + \mathrm{CO} \qquad (\mathrm{V} = 1.17\,\mathrm{V}) \tag{1.6}$$

The MER process has some practical advantages. Kroll is by its very nature a batch process—removing solid titanium from the reactor is a process which cannot be done at temperature. On the other hand, the MER process can change electrodes "on the fly", as titanium oxycarbide anode pellets can be added at any time, and removing the titanium can be as easy as removing and replacing the cathode with a clean one, or harvesting titanium powder from the bottom of the reactor. The sponge titanium of Kroll is also not very useful in its as-produced form. It has to be remelted into other products to be useful. The product of the MER process can be tuned (with the right current density) to be a powder which, once washed, can be used in near-net-shape processing such as traditional powder metallurgy or additive manufacturing processes. Also, unlike the FFC process, the electrolyte has very little solubility for oxygen [25], so the product ends up being very low in oxygen. The process parameters of the electrochemical reaction might also be tuned so that instead of pure titanium, alloys can be made directly (with the right additions to the molten salt).

Chapter 2

Motivation

Titanium is one of the most useful engineering materials, as its low density and high strength provide it with one of the highest strength-to-weight ratios of any metal. Also, its excellent corrosion resistance can make it a competitor with stainless steels. However, its use in industry has been hampered by its high cost [26].

In order to become competitive with other similar materials (stainless steel is used as a benchmark here), multiple aspects of titanium production need to be changed. As seen in Table 2.1, the energy required for the Kroll process alone is approximately 5 times that for stainless steel. This is also reflected in the mass of CO_2 produced for each process, as well as cost (and titanium sponge has to be processed further to become a useful product like a sheet or billet).

Table 2.1: Strength, energy, emissions, and cost, for titanium and stainless steel [26].

	Titanium	Stainless Steel
Strength-to-Weight Ratio	120	77
Processing Energy (kWh/kg)	Kroll: 100	21
Emissions ($kgCO_2/kg$)	Kroll: 36	6.8
Domestic Production ($/kg)	Sponge: 9.00	2.40

It is clear that in order for titanium to become competitive with similar engineering materials, titanium production processes need to change. Therefore, there is significant research taking place to develop new processes that could replace the Kroll process altogether [6]. Electrochemical processes have always been of interest because of what happened to aluminum after the Hall-Héroult process was developed. Before the Hall-Héroult process was developed, aluminum (while lightweight and useful) was very expensive and difficult to produce, as it required reduction using reactive metals (not unlike titanium production today). After the electrochemical Hall-Héroult process was developed, aluminum became cheap and mass-produced. The idea is that if an analogous electrochemical process could be developed, then titanium could also be cheaply mass-produced.

One way of reducing the cost and energy associated with titanium production is to develop a process that can use low-grade ores. Current methods for making titanium invariably rely on high-purity feedstocks. Low-grade ores (i.e. ilmenite), are unable to be used directly in titanium production and are currently only useful if they are made into either a high-grade titaniferous slag, or a synthetic rutile [27, 28].

While the price of titanium ores (shown in Figure 2.1) is highly volatile, the trend is clear—low-grade titanium ores are many times cheaper than their high-grade counterparts. Therefore, if a new process can use lower-grade titanium ores directly, this could go a long way towards making titanium production cheaper, and potentially less energy intensive.

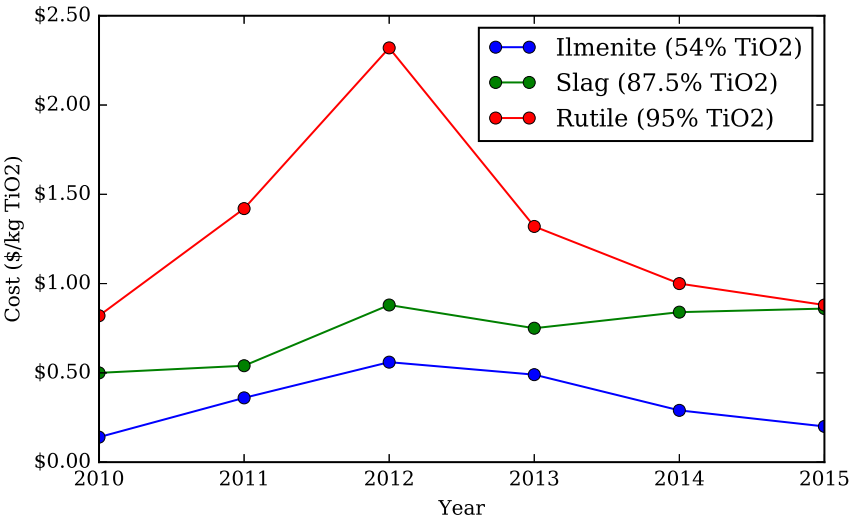

Figure 2.1: Spot prices of different titanium feedstocks from 2010-2015 [29].

Chapter 3

Expected Reactions During Titanium Oxycarbide Production and Electrolysis

Titanium oxycarbide is a complete solid solution of titanium(II) oxide (TiO) and titanium carbide (TiC) [30]. As with any such solution, a range of compositions varying from TiO to TiC can form (TiO_xC_{1-x}). For the MER process, the target composition is an equal mixture of TiO and TiC, yielding a chemical formula of Ti_2OC (or $TiO_{0.5}C_{0.5}$). This is to allow for full dissolution of the anode in the electrochemical cell (no excess TiO or TiC).

In the program FactSage (using a database generated from a paper by Cao et al. [30]), we can use the "Phase Diagram" module to generate a phase diagram for the Ti-O-C system at P = 1 bar and T = 1873 K (1600 °C). All pure compounds, as well as the titanium oxycarbide custom database were selected. This phase diagram, along with the more important phases is shown in Figure 3.1.

Using the FactSage "Equilib" module, we can model the oxycarbide formation reaction (Reaction (1.3)). Using the data from this (the results summarized in Figure 3.2), we can see

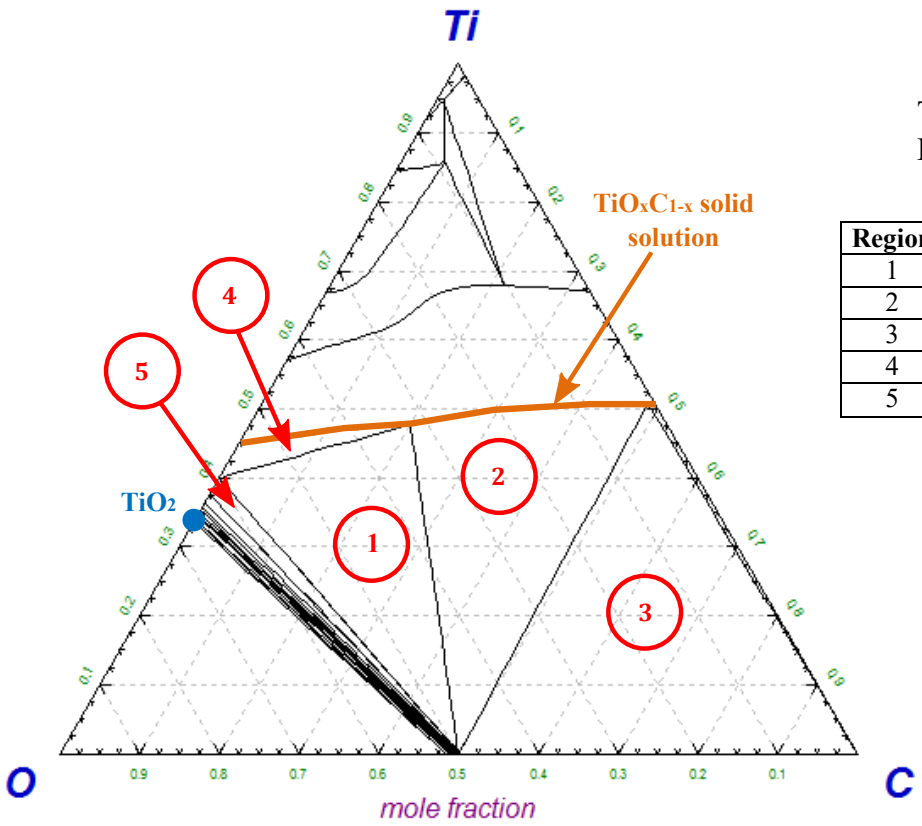

Region	Equilib. Phases
1	$TiO_xC_{1-x} + Ti_2O_3 + CO$
2	$TiO_xC_{1-x} + CO$
3	$TiO_xC_{1-x} + C + CO$
4	$TiO_xC_{1-x} + Ti_2O_3$
5	$Ti_3O_5 + Ti_2O_3 + CO$

Figure 3.1: Phase diagram of the Ti-O-C system at 1600 °C (Calculated with FactSage using database from Cao et al. [30])

that the oxycarbide formation reaction is not a simple one-step reaction, as shown previously. Instead, it should instead be modeled as Reaction (3.1). Strictly speaking, Reaction (3.1) should also include Magneli phases (the higher oxides that exist between TiO_2 and Ti_3O_5), but the reaction from TiO_2 to Ti_3O_5 is so fast that Magneli phases have not been observed in these experiments, even in incomplete oxycarbide formation reactions.

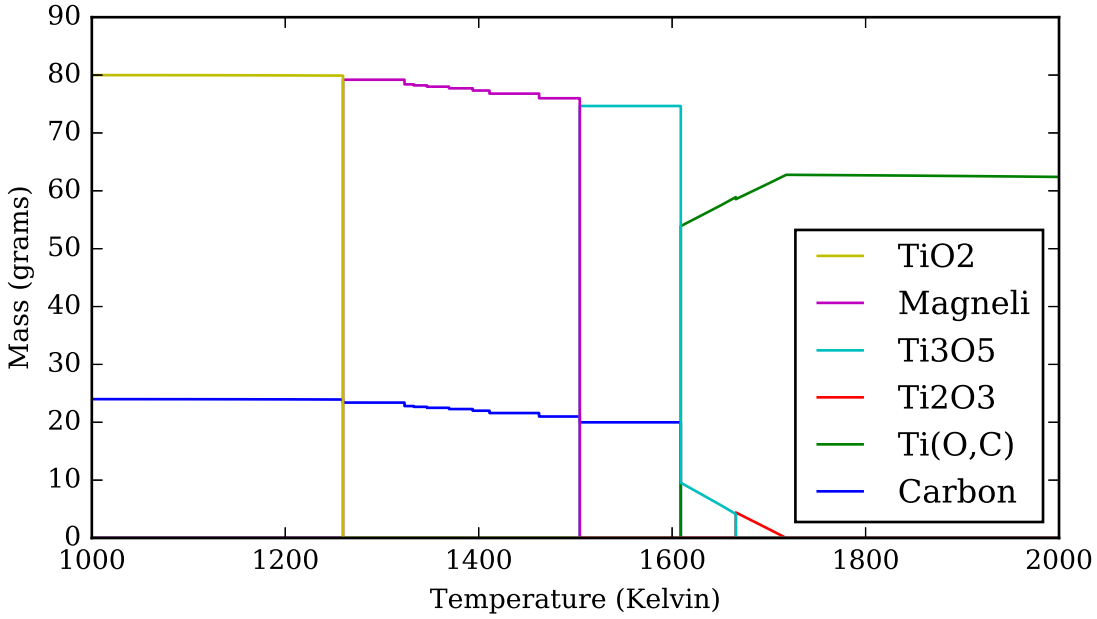

Figure 3.2: Mass plot of TiO_2 and its products over the course of carbothermal reduction (Calculated with FactSage using database from Cao et al. [30]). Calculated by equilibrating 1 moles of TiO_2 with 2 moles of carbon at different temperatures and 1 atm pressure.

$$2\,TiO_2 + 4\,C \longrightarrow \frac{2}{3}\,Ti_3O_5 + 3\,C + CO \longrightarrow Ti_2O_3 + 2\,C + 2\,CO \longrightarrow Ti_2OC + 3\,CO \quad (3.1)$$

From this calculation, the last step before full conversion to titanium oxycarbide is titanium(III) oxide, or Ti_2O_3. Ti_2O_3 was a common impurity in oxycarbide samples prepared in this work, usually due to kinetic effects (discussed in Section 7.8).

Most naturally-occurring titanium ores contain iron. The most common of these lower-grade titanium ores is ilmenite ($FeTiO_3$) [28]. If this material is subjected to carbothermal reduction conditions, we would expect the iron to reduce first. In fact, this is the basis

of one of the more common titanium ore "upgrading" processes, the Becher process [31]. Oxycarbide production from ilmenite is therefore expected to proceed as in Reaction (3.2). However, this material cannot be used directly in a molten salt reactor, as explained in Section 3.2.

$$2\,\mathrm{FeTiO_3} + 6\,\mathrm{C} \longrightarrow 2\,\mathrm{TiO_2} + 4\,\mathrm{C} + 2\,\mathrm{Fe} + 2\,\mathrm{CO} \longrightarrow \mathrm{Ti_2OC} + 2\,\mathrm{Fe} + 5\,\mathrm{CO} \tag{3.2}$$

3.1 Shrinking Core Kinetics

Production of titanium oxycarbide involves reaction between two solids. As with other examples of solid-solid carbothermic reduction, it is expected that CO and CO_2 will be gaseous intermediate species between the solids; see Reactions (3.3) to (3.5). Reduction hence requires diffusion of CO to the reaction front, and diffusion of CO_2 away from the reaction front to the reductant (carbon) to be regenerated as CO.

$$\mathrm{C} + \mathrm{CO_2} \longrightarrow 2\,\mathrm{CO} \tag{3.3}$$

$$2\,\mathrm{TiO_2} + \mathrm{CO} \longrightarrow \mathrm{Ti_2O_3} + \mathrm{CO_2} \tag{3.4}$$

$$\mathrm{Ti_2O_3} + 4\,\mathrm{CO} \longrightarrow \mathrm{Ti_2OC} + 3\,\mathrm{CO_2} \tag{3.5}$$

When reducing large particles ($\geq 50\mu$m), diffusion of the gaseous species through the porous reaction product can be rate-controlling. A reaction mediated by gaseous diffusion of a reducing gas through a porous product layer (pore diffusion) is characterized by the "shrinking-core model" [32].

Given the high reaction temperature required by the oxycarbide production process (as

shown in Figure 3.2), the CO_2 produced in Reactions (3.4) and (3.5) will react with carbon to form CO. The corresponding equilibrium gas compositions are shown in Figure 3.3. The newly reduced CO can either participate in the reaction again or leave the system as there is a net production of gas (2 moles of CO produced per 1 mole of CO_2), so some CO must leave the system.

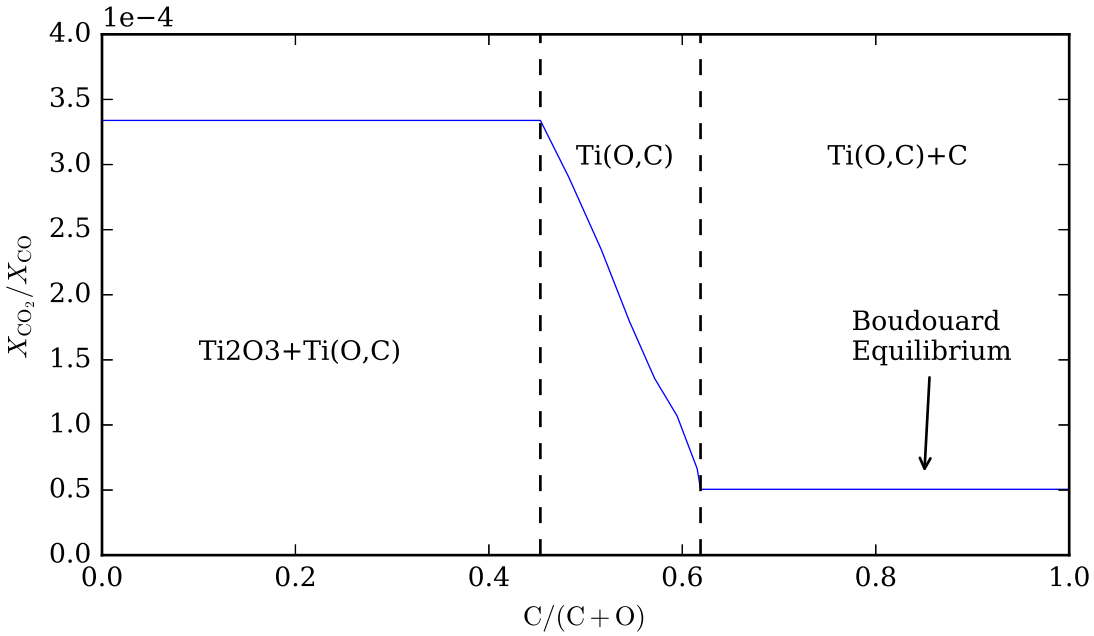

Figure 3.3: Effect of reaction extent on equilibrium CO_2 molar ratio in titanium oxycarbide at T = 1600 °C, P = 1 atm (Calculated with FactSage using database from Cao et al. [30]). The x-axis is the molar ratio C to (C + O) in the solid; zero corresponds to Ti_2O_3 and 1 to TiC

3.2 Electrochemical Potentials

Equilibrium potentials of titanium oxycarbide and expected impurities were calculated using the change in Gibbs free energy for the reaction and the Nernst equation (Equation 3.1). This approach has limitations, as the activity of each dissolved species is unknown, so an activity of 1 was assumed in all cases, unless specified. All potentials are relative to a chlorine reference, as the electrolyte is a mixed chloride salt. These reactions are summarized in

Table 3.1. This can then be adjusted to the actual experimental reference (Ag wire in 4 mol% AgCl). Due to a lack of thermodynamic data on vanadium oxycarbide, the anodic dissolution potential for vanadium oxycarbide was determined experimentally (see Section 10.3.1).

$$E = \frac{\Delta G}{zF} \tag{3.1}$$

The equilibrium potentials can be used to evaluate the limited literature data on titanium electrochemistry in alkali metal chloride salts [18, 35]. A cyclic voltammogram for a NaCl-KCl electrolyte containing in Figure 3.4 (reproduced from Kjos et al. [18]). Equilibrium potentials are marked with orange dotted lines (after adjusting the reference to the pure Ag/AgCl reference of -0.79 V_{Cl_2}), for Na dissolution/plating, Ti^{2+} dissolution/Ti plating, and the Ti^{3+} to Ti^{2+} redox reaction. These reactions appear to be clearly visible.

For the production of high purity titanium it is necessary to remove impurities of all electrochemically active compounds with more positive reduction potentials than titanium (but more negative than titanium oxycarbide), such as iron, silicon, and manganese from titanium oxycarbide before titanium production. If these elements remained in the anode material, these would dissolve at the oxycarbide anode and deposit on the cathode at more positive potentials than titanium. The expected anode behavior of oxycarbide and impurity elements (as various phases) is summarized in Table 3.2, for two potentials: one above and below the titanium oxycarbide dissolution potential. The significance of these potentials for the electrolytic purification of titanium oxycarbide, discussed in Section 9.3.

Compounds that are not electrochemically active, such as inert oxides (i.e. Al_2O_3, MgO, etc.) will remain in the anode basket, forming what is called an "anode sludge". If this anode sludge is allowed to accumulate and mixes in with the rest of the electrolyte, it is possible that it may also contaminate the cathode deposit.

Table 3.1: Half-cell potentials for possible reactions. T = 800 °C, $a = 1$ unless specified, reference states: pure liquid chlorides, metals in condensed form (liquid or solid), gases at 1 atm pressure. Free energy data from NIST [33] and FactSage [34]

Reaction	E (Cl_2), volts	E (ref.), volts	Notes
$Cl_2 + 2\,e^- \longrightarrow 2\,Cl^-$	0	+1.06	
$FeCl_3 + e^- \longrightarrow FeCl_2 + Cl^-$	-0.06	+1.00	
$2\,TiCl_2 + CO + 4\,e^- \longrightarrow Ti_2OC + 4\,Cl^-$	-0.63	+0.43	Anode
$FeCl_3 + 3\,e^- \longrightarrow Fe + 3\,Cl^-$	-0.76	+0.30	
$AgCl + e^- \longrightarrow Ag + Cl^-$	-0.79	+0.27	
$2\,VCl_2 + CO + 4\,e^- \longrightarrow V_2OC + 4\,Cl^-$	-0.81	+0.25	[1]
$AgCl + e^- \longrightarrow Ag + Cl^-$ ($a_{AgCl} = 0.04$)	-1.06	0	Reference
$SiCl_4 + C + 4\,e^- \longrightarrow SiC + 4\,Cl^-$	-1.06	0	
$FeCl_2 + 2\,e^- \longrightarrow Fe + 2\,Cl^-$	-1.11	-0.05	
$5\,FeCl_2 + 3\,Si + 10\,e^- \longrightarrow Fe_5Si_3 + 10\,Cl^-$	-1.16	-0.10	
$SiCl_4 + 4\,e^- \longrightarrow Si + 4\,Cl^-$	-1.23	-0.17	
$VCl_2 + 2\,e^- \longrightarrow V + 2\,Cl^-$	-1.52	-0.46	
$TiCl_3 + e^- \longrightarrow TiCl_2 + Cl^-$	-1.52	-0.46	
$TiCl_3 + 3\,e^- \longrightarrow Ti + 3\,Cl^-$	-1.70	-0.64	
$MnCl_2 + 2\,e^- \longrightarrow Mn + 2\,Cl^-$	-1.79	-0.73	
$TiCl_2 + 2\,e^- \longrightarrow Ti + 2\,Cl^-$	-1.79	-0.73	Cathode
$AlCl_3 + 3\,e^- \longrightarrow Al + 3\,Cl^-$	-1.83	-0.77	
$CaCl_2 + 2\,e^- \longrightarrow Ca + 2\,Cl^-$	-3.27	-2.21	
$NaCl + e^- \longrightarrow Na + Cl^-$	-3.39	-2.33	
$KCl + e^- \longrightarrow Na + Cl^-$	-3.53	-2.47	

[1] Determined by experiment, not calculation

Table 3.2: Behavior of various impurities at +0.3 V_{ref} and +0.6 V_{ref}, T = 800 °C.

Element	Phase	Behavior at +0.3 V_{ref}	Behavior at +0.6 V_{ref}
Titanium	Ti_2OC	Inert	Dissolves
Iron	α-Fe	Dissolves	Dissolves
	Fe_5Si_3	Dissolves	Dissolves
Silicon	Si (in α-Fe)	Dissolves	Dissolves
	Fe_5Si_3	Dissolves	Dissolves
	SiC	Dissolves	Dissolves
	$ZrSiO_4$	Inert	Inert
Chromium	Cr (in α-Fe)	Dissolves	Dissolves
Manganese	Mn (in α-Fe)	Dissolves	Dissolves
Vanadium	V_2OC	Dissolves	Dissolves
Aluminum	Al_2O_3	Inert	Inert
Magnesium	MgO	Inert	Inert
Zirconium	ZrO_2	Inert	Inert
	$ZrSiO_4$	Inert	Inert

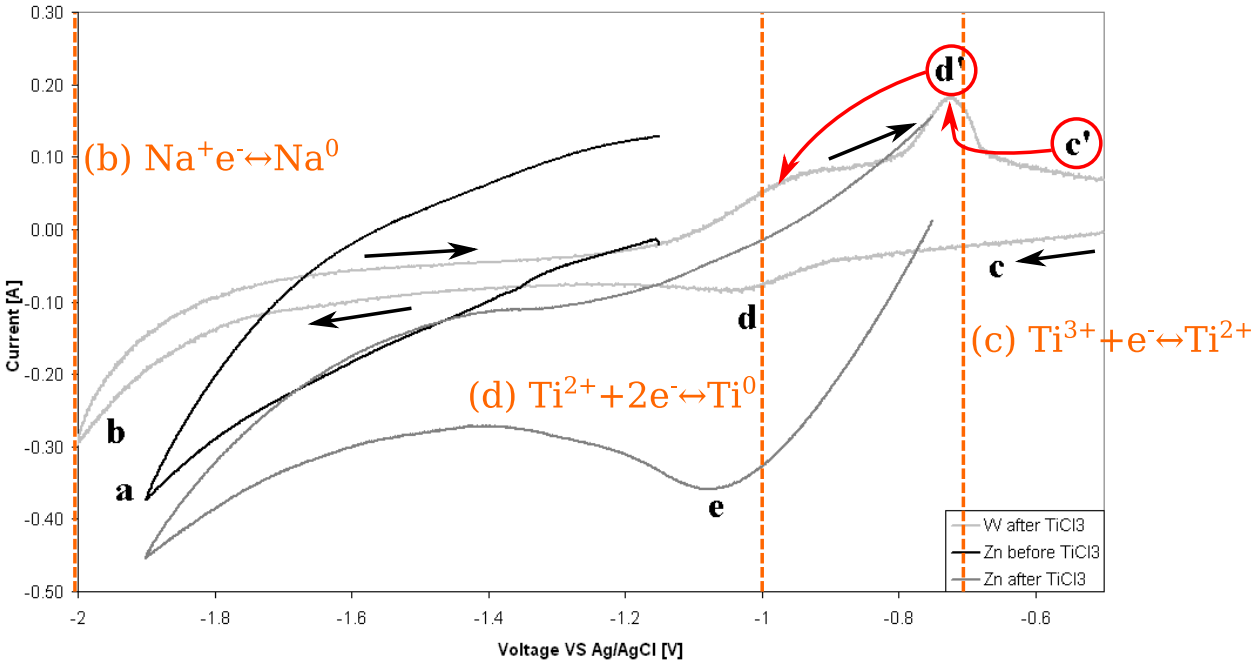

Figure 3.4: Cyclic voltammogram curve of titanium(III) chloride (X = ions in solution in an NaCl-KCl electrolyte at 800 °C (reproduced from Kjos et al. [18]). Light gray curve is using tungsten cathode as working electrode. Calculated equilibrium potentials are shown in orange, and proposed corrections to the reactions identified by Kjos et al. are shown in red.

Chapter 4

Objective and Hypothesis

The primary objective of this research is to successfully make titanium oxycarbide which can be used to make ASTM Grade 2 titanium[1] [36] with a low-grade titanium ore using the MER process. Two main hypotheses were formulated:

1. Titanium oxycarbide of sufficient purity to meet the ASTM Grade 2 standard can be produced from some low-grade titanium ores by removing all "reducible" impurities before titanium electroplating.

2. The kinetics of carbothermal titanium oxycarbide reduction is limited by pore diffusion.

[1]Max impurities: 0.08% C, 0.25% O, 0.03% N, 0.015% H, 0.3% Fe, all others—0.1% each and 0.4% total. All values in weight%.

Chapter 5

Experimental Setup and Procedures

This chapter discusses the different experimental setups and standard procedures used throughout the project.

5.1 Carbothermal reduction furnace setup

The furnace used for carbothermal reduction was a Lindberg vertical tube furnace with an alumina working tube (3" diameter, 48" length) and $MoSi_2$ heating elements (maximum operating temperature of 1700 °C). The ends of the working tube were sealed with water cooled stainless steel end caps with Viton gaskets. There was an inlet on the bottom endcap for gas input, and an outlet on the top endcap for exhaust gas.

Argon (99.9995% purity) was connected to the inlet of the furnace, with an Omega FMA A2200 Mass Flow Controller (70 °F, 29.92 inHg reference) controlling the flow of gas. The exhaust gas flowed through a mineral oil bubbler (to trap any particulates or other contaminants that exited the furnace). The exhaust gas could be directed to the lab exhaust, or optionally to an infrared spectrometer (Cubic Gasboard-3100P Portable Infrared Syngas Analyzer by Wuhan Cubic Optoelectronics Co.) for off-gas analysis (measuring CO, CO_2,

CH_4, H_2, and O_2). The infrared spectrometer could save data on a laptop for later analysis. The setup is illustrated in Figure 5.1.

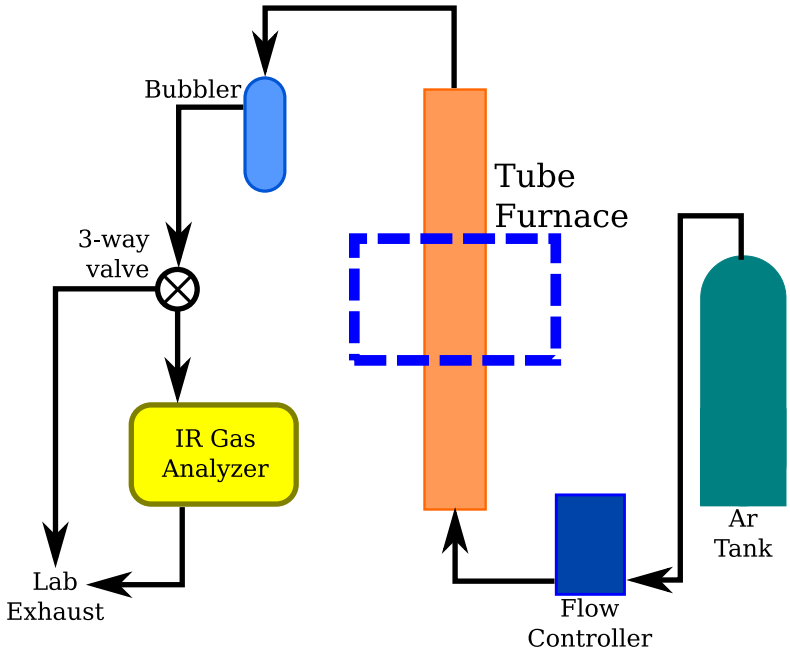

Figure 5.1: Basic schematic of the electrode setup in the reactor. Not to scale.

5.2 Titanium oxycarbide sample preparation

Titanium oxycarbide was primarily synthesized using carbon black (Fisher Chemical) as a reductant. The use of carbon black was primarily due to its low cost, small particle size, high surface area, and its ability to mix well with and coat powders. Reduction samples were prepared by mixing 1 gram of titanium ore with a 10 molar % excess of carbon over the stoichiometric ratio—as determined by a mass balance of the reducible components of the ore. The purpose of the excess carbon was twofold—to ensure the TiO:TiC ratio was at least 1:1 throughout the resulting particles, and to remove residual oxygen in the furnace during the heating phase. This mixture was placed into a small alumina crucible (Coorstek, 99.8% purity, 3/4" diameter and height). This crucible was then placed into the vertical tube furnace and sealed.

To perform reduction, argon gas was first flowed through the furnace at a rate of 65 mL/min. The furnace controller was set to heat the sample to the reaction temperature (1600 °C) at a rate of 5 °C/min, where it was held for 2 hours before cooling back to room temperature at a rate of 5 °C/min. To perform kinetic analyses, the exhaust gas were directed to the IR spectrometer, and flow rate and gas concentrations (CO, CO_2, and O_2) from the IR analyzer were recorded during the entire process.

5.2.1 Ore grinding and sizing

Many of the experiments performed over the course of this project necessitated the use of titanium ores of reduced particle size (relative to the original) or specific particle size ranges. This was performed by grinding the ore material in a SPEX SamplePrep ShatterBox 8530 "ring and puck"-style tungsten carbide grinder. For this, 50 grams of titanium ore would be put into the grinder and ground for an interval between 30 seconds and 3 minutes—the exact interval depended on many factors including the original particle size distribution of the ore and whether a specific size (less time) or fines (more time) were required for the experiment. After the grinding interval was complete, the resulting ore would be removed from the grinder.

If a specific particle size range was needed, the ore powder would sieved to select specific particle size ranges. The correct mesh sieves would be selected and combined to form a stack (in decreasing order of mesh size). The powder would then be added to the top of the stack and the stack would then be mechanically agitated for 30 minutes. To aid in the sieving process water would often be added to promote a fine dispersion of particles. Upon the conclusion of sieving, particles of the correct size could be recovered from the corresponding sieve layer.

5.3 Electrochemical Reactor Design

For the purposes of this project, an electrochemical reactor was designed, built, and tested. A basic schematic of the reactor is shown in Figure 5.2.

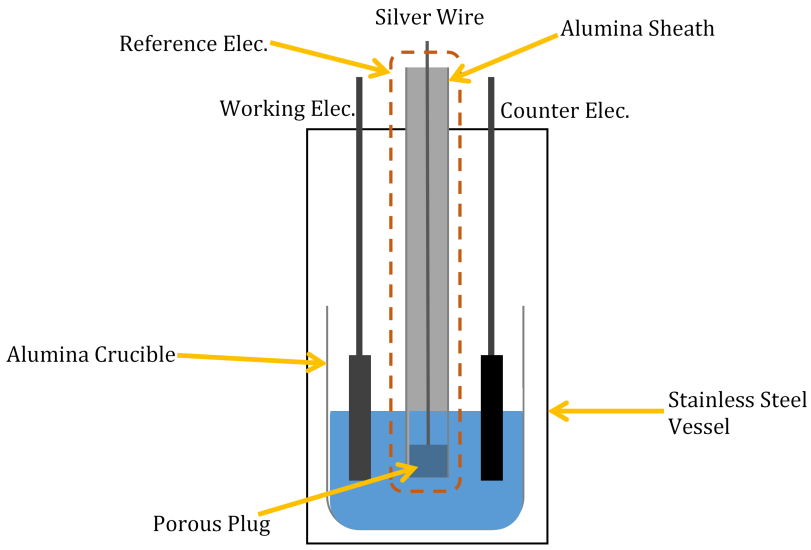

Figure 5.2: Basic schematic of the electrode setup in the reactor. Not to scale.

The reactor was placed in a resistance-heated vertical tube furnace. All reactor components were made of 316/316L stainless steel unless otherwise specified. The main reactor tube was an NPT size 3 (3.5" OD) unthreaded pipe (schedule 10), with a 3.5" disk and flange attachment welded to the bottom and top, respectively. The reactor was held in place in the furnace by a flange that was bolted to a frame above the furnace. The reactor cap was placed over the flange and the entire flange assembly was bolted together, holding the reactor tube, flange, and reactor cap firmly bolted to the furnace's frame. A 1/8" thick Viton gasket provided a gas-tight seal between the reactor tube and the reactor cap.

The reactor cap contained 6 ports. Two 7/8" Swagelok fittings were the main anode and cathode ports for the reactor. Three 1/4" Swagelok fittings were for the gas inlet, reference electrode, and the thermocouple tube. The thermocouple tube could also be replaced by a pressure gauge, or used for electrolyte sampling, if necessary. A 3/8" Swagelok fitting was

used as a gas outlet to prevent salt condensation from clogging the gas exhaust tube.

The main electrodes were 1/4" diameter stainless steel rods inserted into high-temperature silicone stoppers. The stoppers were the correct size to fit the 7/8" Swagelok fittings on the electrode ports, while also being an electrically insulating barrier between the rods and the reactor cap. The stainless steel rods were attached to 1/2" graphite rods by Kanthal (iron-aluminum-chromium) wire. Two types of electrode can be attached at the end of the rods (by platinum-rhodium thermocouple wire): metal strips (304 stainless steel, 1016 steel, or Grade 2 titanium). Alternatively, the graphite rods could dipped into the electrolyte and used as graphite electrodes.

The anode basket was similar in shape to a graphite crucible. The bottom is dense; electrolyte access to pellets within the basket is from the top of the basket (the immersion depth is greater than the lower cylindrical part, and smaller than the holes near the top from which the basket is suspended. A drawing of the anode basket is included in Figure 5.3.

The reactor was also connected to a vacuum pump, for the purposes of removing water from salts. The gas outlet passed through a series of bubblers to capture salt (using a water bubbler) and scrub any potential release of chlorine gas (using a solution of NaOH in water).

The potentiostat used in the reactor setup was a Gamry Reference 3000 potentiostat/galvanostat and was controlled by a laptop using the Gamry Framework software package.

5.3.1 Design of the reference electrode

In electrochemical systems, a reference electrode is needed to provide an absolute reference point for reactions taking place. In many systems, this is often a silver/silver chloride (Ag/AgCl) reference electrode. The main reasons for this are that silver is relatively noble and has only one oxidation state (+1), and therefore, the only possible reaction is as follows:

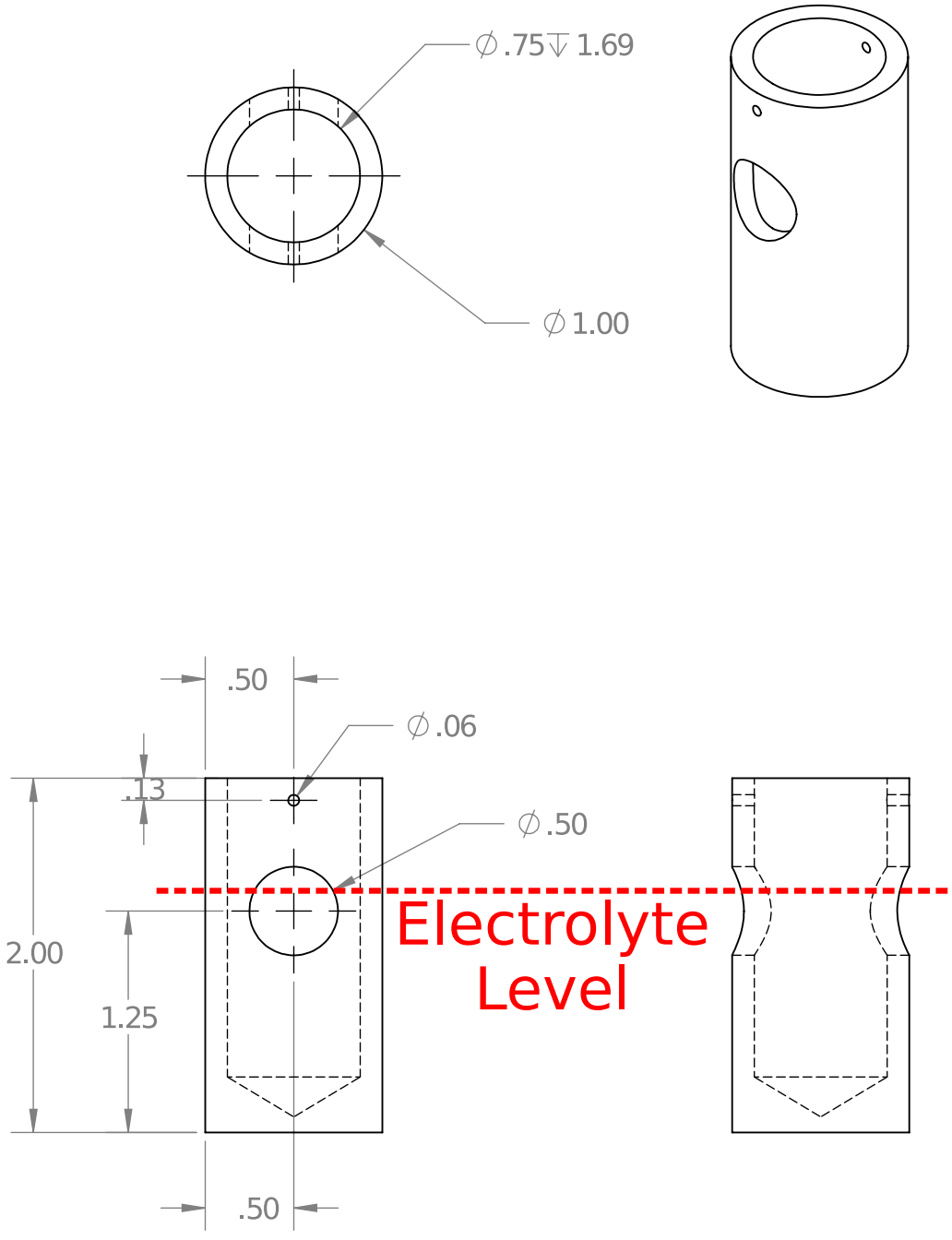

Figure 5.3: Drawing of graphite anode basket used in experiments. Red line denotes targeted electrolyte level.

$$Ag^+ + e^- \longleftrightarrow Ag \tag{5.1}$$

As this is the only possible reaction involving silver, this makes silver an ideal candidate for being a reference. In aqueous salt systems where these electrodes are often used, the silver chloride forms as a solid film on top of the silver.

However, in our molten salt system, the temperature is above the melting point of silver chloride. Therefore, unlike the aqueous salt system, we cannot have a solid film of silver chloride on silver. However, as silver chloride is soluble in the chloride salts we use as electrolytes, we can still utilize this as a reference.

The literature shows a few examples of molten silver chloride solutions being used as a reference electrode [37, 38]. We can then use the Nernst equation to find the potentials of this reaction, taking into account the activity of dissolved silver chloride. As a first-order approximation, the molar concentration of the salt is taken to be equal to its thermodynamic activity, with a constant activity coefficient (reasonable for dilute solutions). Figure 5.4 is a plot of potential as a function of silver chloride activity. Measured equilibrium potentials [39] for AgCl in equimolar NaCl-KCl confirms that AgCl shows near-ideal behavior, with $\gamma_{AgCl} = 0.85$ at $X_{AgCl} = 0.04$. This deviation from ideality changes the Ag/AgCl equilibrium potential by -15 mV (from ideality).

The silver-silver chloride electrode was constructed with silver wire (1 mm diameter), a 1/4" outside diameter alumina tube, alumina insulation material (ZIRCAR alumina felt type RS-3000), and hardener (ZRCI AL-HARD Rigidizer—alumina powder in an aqueous suspension, with phosphoric acid as binder). A small piece of the alumina insulation was dipped in the hardener and put into one end of the alumina tube. Drying this produced an alumina tube with a porous plug on one end.

Previous observations in this work showed that the molten sodium chloride–potassium chlo-

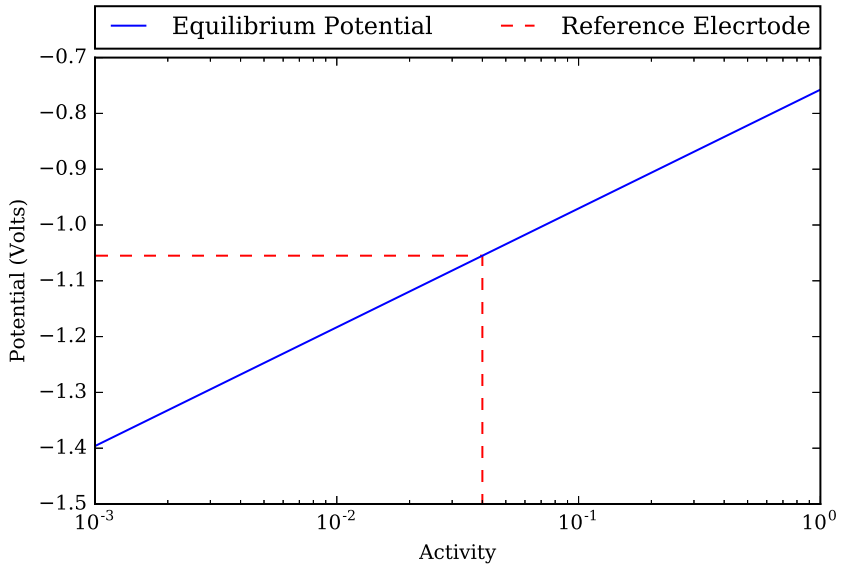

Figure 5.4: Plot of Ag/AgCl potential as a function of AgCl activity (T = 800 °C). 4% concentration (used in all experiments) is shown as dotted line.

ride electrolytes wet alumina very well. Upon inserting this plugged tube into the electrolyte, the salt easily percolated through the porous plug, and filled to the overall fluid level of the electrolyte in the larger crucible. The silver wire was inserted into into the tube for contact with the electrolyte pool. This is illustrated in Figure 5.2.

Silver chloride was produced in situ by anodic dissolution of the silver wire. Based on the known volume of the small reference electrolyte pool, and the desired silver chloride concentration, the number of moles of silver chloride required was calculated and converted to the required anodic charge, based on Faraday's law and assuming 100% current efficiency. The applied current was 50 mA for 240-300 seconds (depending on the inside diameter of the alumina tube) to produce an AgCl concentration of 4 molar percent.

5.4 Preparation and Setup for Electrochemistry Experiments

To prepare an electrolyte for electrochemical testing, 120 grams of sodium chloride and 150 grams of potassium chloride would be weighed and put into an alumina crucible (Almath, 2.5" inside diameter, 4" height), along with 50 milligrams of dopant salt—either $FeCl_2 \cdot 4\ H_2O$ (Fisher Chemical) or CuCl (Alfa-Aesar)—depending on the system being tested ($FeCl_2 \cdot 4\ H_2O$ for iron-based systems and CuCl for others). This crucible was then placed into an oven at 200 °C where it was stored overnight.

To begin the experiment, the crucible was placed into the stainless steel reactor and sealed. The gas inlet and outlet valves was closed and the vacuum pump was used to take the reactor to low vacuum (0.05 to 0.1 atm). The furnace controller was set to heat the sample to 400 °C at a rate of 15 °C/min, where it was held for 1 hour to dry the sample. After the drying phase, the vacuum pump was turned off and the reactor was backfilled with argon (flowrate of 100 mL/min; argon would be kept flowing after the furnace reached atmospheric pressure). The furnace would then continue to heat the sample to the working temperature (usually 800 °C) at a rate of 15 °C/min.

30 minutes after reaching the working temperature (to give the salt a chance to fully melt and mix), the anode, cathode, and reference electrode would be inserted into the melt, and the reference electrode would be generated. The system would then be put into a potentiostatic regime (with the anode as the working electrode), and the anode would be dissolved for 1 hour. This served two purposes: to remove any residual water dissolved in the molten salt, and to put the correct ion species into solution (especially if the doped species was different than the system being studied). After this pre-electrolysis phase, the system would be ready for the next phase of the experiment.

At the conclusion of the experiment, the anode and cathode would be carefully removed,

and the reference electrode raised to above the electrolyte level. The system would be cooled to room temperature at a rate of 15 °C/min. To recover anode powder material from the anode basket or cathode deposit from the bottom of the crucible, the basket/crucible would be immersed upside-down in water and stored in an oven at 80 °C. After the salt had been dissolved, the powder would be filtered in a cellulose thimble. The thimble containing the filtrate would then be placed in a Soxhlet extractor and washed continuously with distilled water for at least 18 hours. The washed filtrate would then be removed from thimble by spraying with de-ionized water into a funnel lined with filter paper. The filtrate would then be allowed to dry in air. When the filtrate was fully dried, it would be scraped into a glass sample vial for later analysis.

5.4.1 Electrochemical Impedance Spectrometry (EIS)

After pre-electrolysis, electrochemical impedance spectrometry (EIS) could be used to measure the impedance at the working electrode. The potentiostat would then be set to perform potentiostatic EIS centered around the rest potential (0 V_{OC}). The frequency range tested was from 100 kHz to 100 Hz, with an amplitude of 10 mV_{rms}. The potentiostat was also set to wait 1 minute before taking the open-circuit potential measurement to allow the system to stabilize at the rest potential. Upon the conclusion of the test, the Gamry software would then tabulate and save the data on the laptop for later analysis.

This EIS data could then be analyzed to determine the capacitance of the working electrode. This can be done using the reported imaginary impedance (Z_{imag}). The low-frequency impedance data is associated with the capacitance of the electrode surface, and the high frequency data is usually associated with the inductance of the leads. To find the capacitance, we can convert our imaginary impedance to electrical reactance (X, where $X = Z_{\text{imag}}$). If we plot reactance as a function of natural frequency (ω, where $\omega = 2\pi f$), we should see a linear trend. This trend is described by Equation 5.1, which shows that the slope of this

trendline is $-C$, where C is capacitance in Farads.

$$\frac{1}{X} = -\omega C \tag{5.1}$$

5.4.2 Polarization experiments

After pre-electrolysis, polarization curves could be obtained by using the potentiostat in a potentiodynamic mode. The potentiostat would be set to sweep the potential at a rate of 2 mV/sec from -0.1 V_{OC} to a value higher than the equilibrium dissolution potential of the material being tested. The potentiostat was also set to wait 1 minute before taking the open-circuit potential measurement to allow the system to stabilize at the rest potential before beginning the potentiodynamic scan. Upon the conclusion of the test, the Gamry software would then tabulate and save the data on the laptop for later analysis.

To obtain an IR-corrected potentiodynamic curve the resistance of the working electrode would be needed. EIS data performed on the working electrode would be examined to find the resistance. This resistance would then be used in conjunction with Ohm's law to obtain IR-corrected data by Equation 5.2.

$$E_{\text{corr}} = E_{\text{meas}} - I_{\text{meas}}R \tag{5.2}$$

5.5 Characterization Methods

5.5.1 X-Ray Diffraction (XRD)

X-ray diffraction was performed on all raw materials and nearly all experimental samples in this project. The purpose of XRD was for crystalline phase identification. As nearly all of the samples tested were powders, standard methods for powder x-ray diffraction techniques

were used. The powder was placed into a powder sample holder and made level to the sample holder surface—if the powder particles were larger than the thickness of the sample holder (1 mm), the samples were ground using the back of a spatula. The instrument used was a PANalytical X'Pert Pro x-ray diffractometer, scanning from $20° \leq 2\theta \leq 90°$ using Cu $K\alpha$ radiation. To quantify the amount of each phase present, the S-Quant feature of the QualX software package [40] was used to obtain an estimate.

XRD can be used to determine the TiO:TiC ratio in a titanium oxycarbide solid solution. This is done by determining the lattice parameter (a) of the FCC unit cell of titanium oxycarbide, and comparing it to literature data on the lattice parameter of titanium oxycarbide solid solutions [41].

XRD can only be used in cases where the phase in question is crystalline, which is why residual carbon content cannot be estimated by XRD (carbon black is mostly amorphous). The phase also needs to be present in sufficient amounts to be identifiable over the background noise of the pattern; this is especially true with low-symmetry phases, which have very few strong reflections.

5.5.2 Scanning Electron Microscopy (SEM)

SEM was performed on a wide variety of different materials, from ore to processed samples. SEM was performed with either an FEI Explorer, FEI XL30, FEI Quanta 200, or FEI Quanta 600 scanning electron microscope—all which can image in secondary and backscatter mode, and have energy-dispersive spectrometers (EDS) detectors equipped. An accelerating voltage of 15 kV was used for most instances, but accelerating voltages of 10 kV or less were sometimes used when higher resolution or a lower EDS excitation volume was required.

Most of the samples analyzed by SEM were polished sections of powder samples. To prepare these samples, a small amount of powder was scooped into an SEM sample mold, and Struers

EpoFix low-viscosity epoxy mounting resin poured into the mold. The samples were then degassed in a vacuum desiccator for 1 hour to remove any air bubbles from the mounted sample. The resin was allowed to cure overnight. The next day, the mounted samples were removed from the molds and polished by hand on a polishing wheel with 600, 800, and 1200 grit silicon carbide sandpapers. The samples were then polished on a cloth wheel sprayed with 1 μm alumina suspension. The polished samples were then washed with dish soap, water, and a clean polishing cloth to remove any remaining alumina suspension. The samples were then sprayed with methanol to wash away any remaining water and dried with a hair dryer. The sample was then coated with 2-3 nm of platinum using a plasma coater, and copper tape was used to make a conductive path between the top and bottom surface of the sample.

To analyze the surface of a powder sample, the sample had to be prepared differently. A piece of double-sided carbon tape was affixed to an SEM sample stub, and then pressed into the powder. Loose powders were removed by tapping the edge of the sample stub against the lab bench. As most of the powders prepared in this manner were non-conductive, they were also coated with 2-3 nm of platinum using a plasma coater.

Imaging of the mounted SEM samples were mostly carried out using the backscatter detector for the purposes of Z-contrast—which show higher atomic number (Z) areas as brighter. Stub-mounted powder samples were mostly imaged with secondary imaging, which has greater topological contrast. EDS was sometimes used to quantify the elemental composition at a given point, or for EDS mapping.

5.5.3 X-Ray Fluorescence (XRF) Spectrometry

In the cases where a bulk elemental composition was needed, x-ray fluorescence spectrometry was used. XRF was performed with a PANalytical MiniPal 4 x-ray fluorescence spectrometer. The MiniPal 4 uses an energy-dispersive spectrometer (EDS) detector to detect x-rays. The

instrument is also capable of being flooded with helium gas to allow for the quantification of light elements.

For analysis of non-light (heavier than argon) elements of similar atomic number (such as the quantification of titanium and iron), the spectrometer can be run in "standardless" mode with a reasonable degree of accuracy. For a full quantification of elements in a material (such as an ore), the instrument needs to be calibrated with standards. A set of standards were developed for the quantification of elements commonly found in titanium ores. However, even with calibration, the analysis of light element contents has a certain level of uncertainty. Also, quantifying small amounts of elements close together on the periodic table (such as vanadium, chromium, and manganese) is often leads to additional uncertainty, as the x-ray spectra of these elements can overlap, making deconvolution of the spectra difficult. This is why the quantification of certain elements by XRF is listed as being uncertain in some parts of this document.

5.5.4 Optical Microscopy

Optical microscopy was rarely used over the course of this project. It was only used in cases where the sample was too fragile to be cleaned or put under vacuum—such as for examining the electrodeposit on a cathode. The microscope used was a Leica MZ12 stereomicroscope with an eyepiece camera. Due to the fragility of the samples being examined, there was no sample preparation.

Examination of the samples were carried out only at the specific magnifications. After imaging of the samples were done, a ruler with small graduations was imaged at the magnifications used for the purposes of obtaining a proper scale. Scale bars were added to images later using the ImageJ software package [42].

5.5.5 Particle Size Analysis

To determine the size and surface area of different particles, a representative SEM image of the particle population would be loaded into the ImageJ software package. After setting the scale and setting the correct threshold, the "Analyze Particles" feature is used to obtain the area (A) and perimeter (P) of all particles. Depending on the morphology of the particles being analyzed, these quantities are used differently.

For spherical, roughly spherical, or angular particles, the particles are assumed to be spherical. The radius of each of the particles is derived from the area (using $A = \pi r^2$) and used to determine the surface area ($A_s = 4\pi r^2$) and volume ($V = \frac{4}{3}\pi r^3$). From the volume and density of each particle, we can derive mass for each particle. Then the total surface area and mass are totaled for the entire population, and used to obtain a specific surface area (in cm^2/g).

For particles with a flaky morphology, a uniform-thickness prism is assumed. In addition to the perimeter and area for the population, a characteristic length (l) is needed—for images where the population is seen edge-on the characteristic length is assumed to be the average length of the particle, for images where the flat cross-section is seen the characteristic length is the thickness of the flake. Using this information, the surface area is determined by $A_s = 2A + Pl$ and the volume by $V = Al$. The specific surface area is then derived from the surface area and volume information in a similar manner to the spherical particles.

This method of surface area measurement was not meant to be precise, but serve as a reasonable approximation. For example, the SEM images used to quantify the area and perimeter would miss sub-micron features such as nanoporosity, which would influence the surface area. Brunauer-Emmett-Teller (BET) surface area measurements could provide more accurate measurements of surface area, but this technique was not used as the measurements obtained from the analysis of SEM images were deemed sufficient.

Chapter 6

Raw Materials

A wide variety of raw materials were used for the experiments outlined in this document. This chapter will focus on the relevant titanium concentrates. A summary of the compositions of the titanium concentrates is given in Table 6.1 (determined by XRF). The ability of the ores to be converted to titanium oxycarbide, or be upgraded to synthetic rutile (where applicable) will also be discussed.

6.1 Titanium dioxide TiO_2 Pigment

Initial experiments on making titanium oxycarbide used titanium dioxide (TiO_2) pigment (Alfa, 99.8%, 2 μm). The experiments showed that it is an ideal working material, as it is very easy to make high-purity titanium oxycarbide from pigment, making it a good material for control experiments, as no significant levels of impurities are present. This TiO_2 pigment, mixed with other oxides, was the used to calibrate the XRF machine for characterization of the other titanium concentrates.

The X-ray diffraction pattern in Figure 6.1 shows that this pigment is actually a mixture

Table 6.1: Compositions of all natural and processed ores used in wt%

	Rutile (Australia)	Leucoxene (Australia)	Pseudo-rutile (Florida)	Ilmenite (S. Africa)	Slag (S. Africa)	Ilmenite (Madagascar)	Slag (RTCS) (Canada)	UGS (Canada)	Panzhihua Ilmenite (China)
TiO_2	95.6	91.5	77.5	40.8	81.8	60	61.5	94.5	46.8
Ti_2O_3	-	-	-	-	*	-	28.0	-	-
Fe_2O_3	2.15	2.18	17.51	*	-	23	-	1.4	6.10
FeO	-	-	*	53.7	11.0	11	7.5	-	34.10
Fe	-	-	-	-	*	-	0.4	-	-
Al_2O_3	0.17	0.56	0.27	0.54	0.58	0.95	1.7	0.5	1.00
CaO	0.03	0.04	0.18	0.13	0.35	0.02	0.11	0.12	0.84
Cr_2O_3	0.20	0.14	0.40	0.39	0.28	0.05	0.08	0.07	-
MgO	0.05	0.05	0.04	0.03	0.09	0.50	1.3	0.7	5.66
MnO	0.01	0.01	0.93	1.27	1.93	0.40	0.50	0.04	0.66
Nb_2O_5	0.33	0.86	0.12	0.09	0.12	0.25	0.28	100 ppm	-
SiO_2	1.29	2.23	1.64	2.13	3.75	0.35	1.0	1.8	3.23
V_2O_5	-	-	1.37	0.89	-	0.20	0.31	0.4	0.06
ZrO_2	0.26	2.43	0.11	0.04	0.13	0.10	0.15	-	-
Th+U	45 ppm	143 ppm	46 ppm	63 ppm	40 ppm	160 ppm	190 ppm	3 ppm	-

- not specified/measured

* observed but not measured

of rutile and anatase. As far as high temperature processing is concerned, having anatase present has not affected the product, as the anatase likely transforms to rutile when taken to high temperature. As stated before, the particle size is reported to be 2 μm, allowing reactions with pigment TiO_2 be very fast and even practical at lower temperatures (as kinetic limitations are far less noticeable).

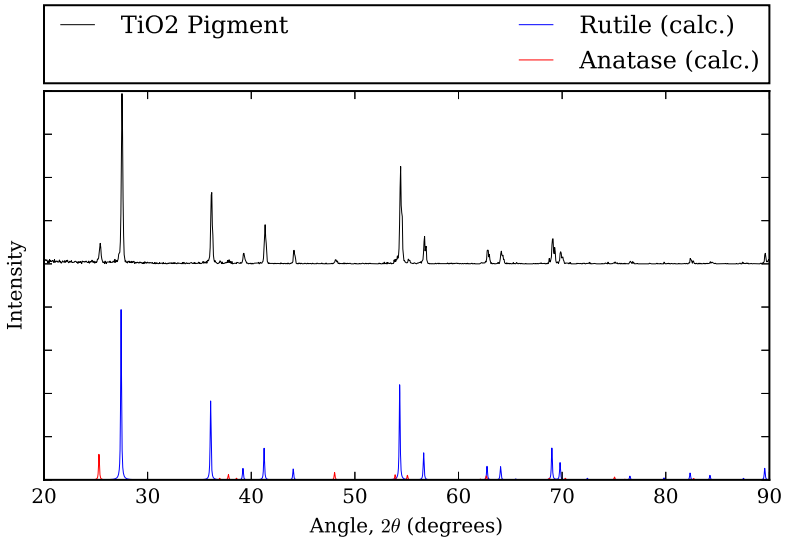

Figure 6.1: XRD Pattern of Pigment TiO_2.

6.2 Natural Rutile Mineral Sand (Australia)

Of the titanium minerals, natural rutile is generally the purest form, containing over 95% TiO_2. Samples of Australian natural rutile and leucoxene mineral sands were tested (discussed in a Section 6.3). The composition of this mineral sand is shown in detail in Table 6.1.

X-ray diffraction of this material shows that it is almost a perfect match for rutile (see Figure 6.2). SEM (Figure 6.3 shows the material consists of mineral sand particles with an overall average diameter of approximately 100 μm. The material is fully dense. Backscattered SEM also shows the presence of bright particles—EDS shows these to be zircon crystals ($ZrSiO_4$).

The presence of zircon ($ZrSiO_4$) suggests that while the bulk elemental compositions given in Table 6.1 are correct, it does not give us information on what compounds are present (because XRF tells us nothing about the actual compounds present, only bulk composition). Thus some of the SiO_2 content is not present as silica, but in the zircon. SEM also showed the presence of a few monazite particles ($(Ce,La)PO_4$), but these particles were too rare to significantly influence the composition of the ore.

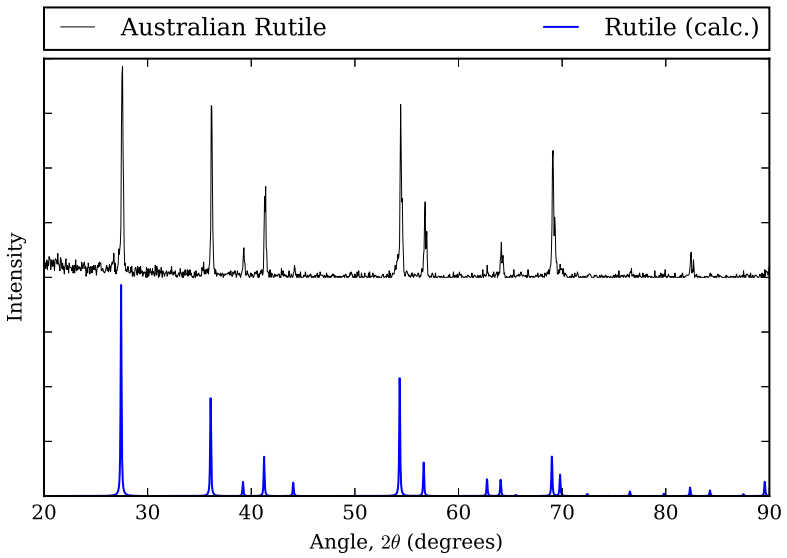

Figure 6.2: XRD Pattern of Australian rutile mineral sand compared to pure compounds.

6.3 Leucoxene Mineral Sand (Australia)

A "leucoxene" mineral sand is the designation given to a broad range of titanium minerals—generally iron-containing ores in which the TiO_2 content is between that of pseudorutile[1] (60 weight % TiO_2) and natural rutile (95 weight % TiO_2). These materials can have very different microstructures, ranging from large particles with extensive porosity (leached, but not densified), to almost natural rutile-like morphologies.

[1]Ideal composition $Fe_2O_3{\cdot}3(TiO_2)$ [43]

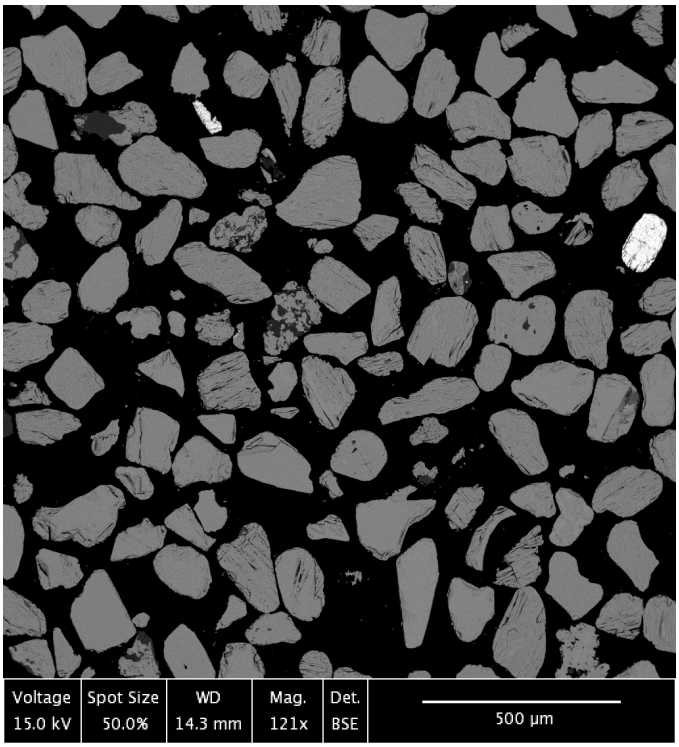

Figure 6.3: Backscattered SEM image of Australian rutile mineral sand (polished section). Bright particles are zircons.

The Australian leucoxene mineral sand was from the same source as the natural rutile. Its elemental composition is very similar to that of the natural rutile, shown in Table 6.1. The x-ray diffraction (Figure 6.4) shows the material is rutile, is almost identical to the natural rutile in Section 6.2. SEM of the material showed an almost identical morphology to the natural rutile, with a greater number of zircon and silica particles present. In fact, the only reason this material is considered to be a leucoxene appears to be its high zircon and silica content. The titania particles themselves are considered to be natural rutile.

6.4 Pseudorutile Mineral Sand (Florida)

This sample was labeled as "Florida Ilmenite". However, x-ray diffraction studies showed that while there was some trace levels of ilmenite present in the ore, there was a significant amount of rutile, however with additional peaks, as seen in Figure 6.5. This seems to indicate

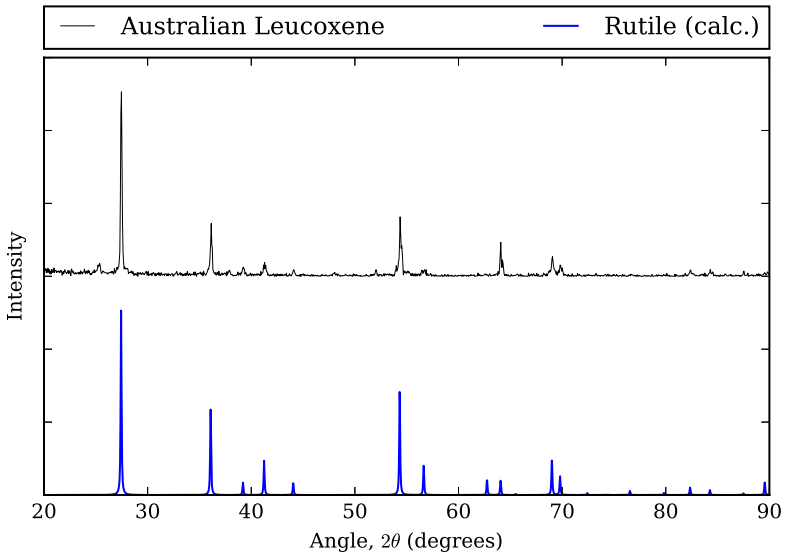

Figure 6.4: XRD Pattern of Australian leucoxene mineral sand compared to pure compounds.

that the ore is a mixture of rutile, pseudorutile ($Fe_2Ti_3O_9$)[43], and ilmenite. It should also be noted that the main peak of pseudorutile is 102, which occurs at the same angle as the 211 peak of rutile, which is rutile's second most intense peak. So while identifying the presence of rutile and pseudorutile is possible, determining the exact content of rutile and pseudorutile is not trivial. This is mitigated to an extent by XRF (see Table 6.1), which shows that the titanium content is too high relative to iron for the material to be an ilmenite or pseudorutile, and allows an estimate as to the rutile content—rutile comprises approximately 50 weight percent of this material. Taking all these into account, it can be concluded that this material is a pseudorutile mineral sand, and will be identified as such in this document.

Pseudorutile itself is a naturally occurring phase which is a result of the natural weathering of ilmenite [44, 43]. The iron oxidizes, and some of it is leached away, yielding the atomic formula of $Fe_2Ti_3O_9$ or $Fe_2O_3{\cdot}3(TiO_2)$. It should be noted that unlike ilmenite, which ideally has all iron in the Fe^{2+} oxidation state, pseudorutile has iron in the Fe^{3+} oxidation state.

SEM of this sample (Figure 6.6) shows that the ore itself is a mixture of regions of various iron compositions, sometimes within the same particle. This can be distinguished based on

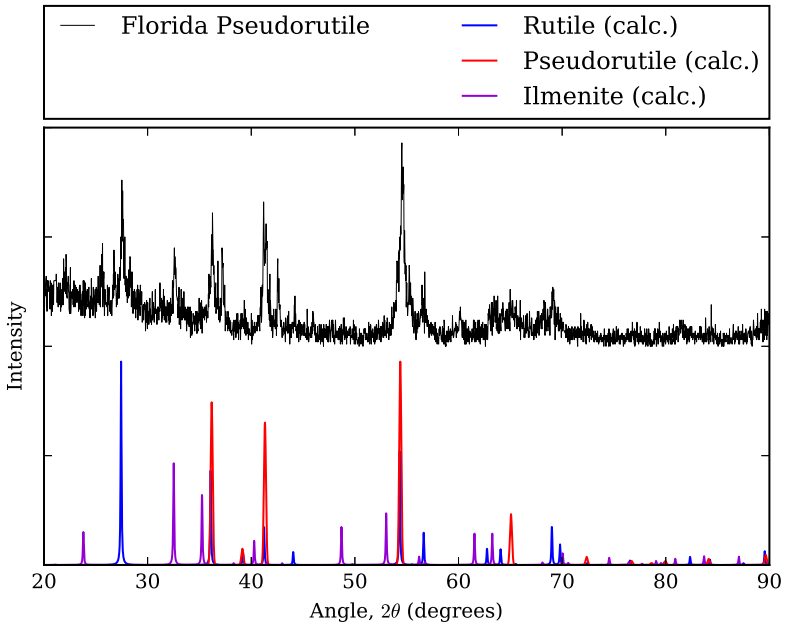

Figure 6.5: XRD Pattern of Florida pseudorutile compared to pure compounds.

the brightness in the backscattered electron images (iron-rich regions are brighter). Some of the lower-contrast areas correspond with increased porosity and low iron content, which is a good example of weathering. EDS shows that the bright particles that show up in the backscatter image are high in zirconium, but contain no silicon, indicating that they are some form of zirconia (ZrO_2), rather than zircon as seen in the rutile and leucoxene mineral sands. EDS analyses show varying concentrations of other impurities such as aluminum, which varies from only trace amounts in some particles, to over 1 wt% in others.

6.5 Ilmenite Mineral Sand (South Africa)

The South African ilmenite mineral sand is a very-iron rich ilmenite mineral sand, to the point that the FeO content is greater than 50%, as seen in Table 6.1. The XRD pattern in Figure 6.7 shows that this mineral sand consists mostly of ilmenite, with trace amounts of pseudorutile—which is unexpected, considering the high iron content—and quartz. SEM (Figure 6.8) shows that the material is generally an ilmenite, with a few particles having a

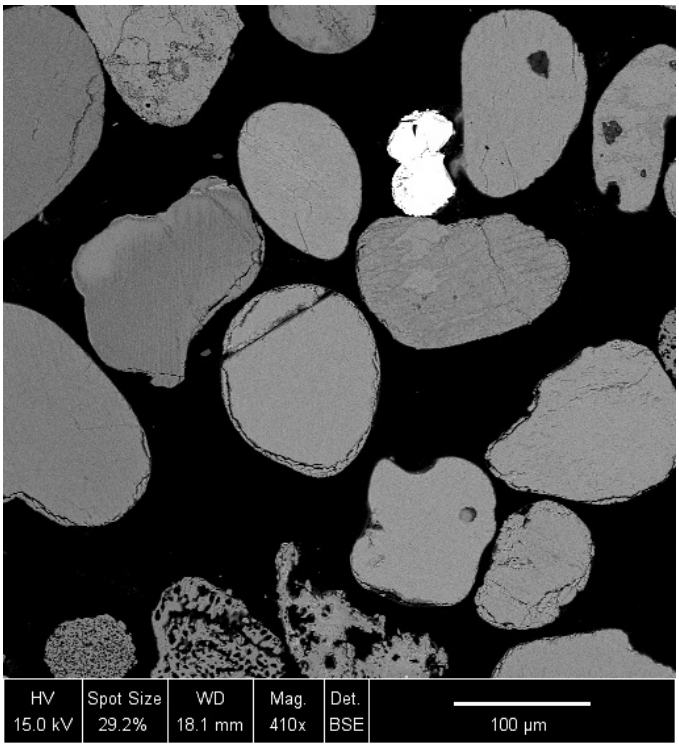

Figure 6.6: Backscattered SEM image of Florida Pseudorutile mineral sand. Bright particle is zirconia.

little less iron. There is also some silica present as inclusions in some particles (the dark spots in Figure 6.8), which matches both the quartz observed in the XRD pattern, and the elevated levels of silicon present in XRF analysis. XRF also shows the material as mildly radioactive, with a combined 63 ppm of uranium and thorium. However, unlike other ores described thus far, the zirconium content is too low for the radioactive elements to be contained in any zircon-type particles. This radioactivity is likely contained within the ore itself.

6.6 Titaniferous Slag (South Africa)

Titaniferous slags are different than all the kinds of ores discussed here due to their synthetic nature. They are produced by reducing ilmenite with coke at high temperatures of around 1600 °C in an electric arc furnace [2]. The result is pig iron which is tapped off, and a partially reduced slag, rich in titanium(III) oxide, iron(II) oxide, and other reduced oxides.

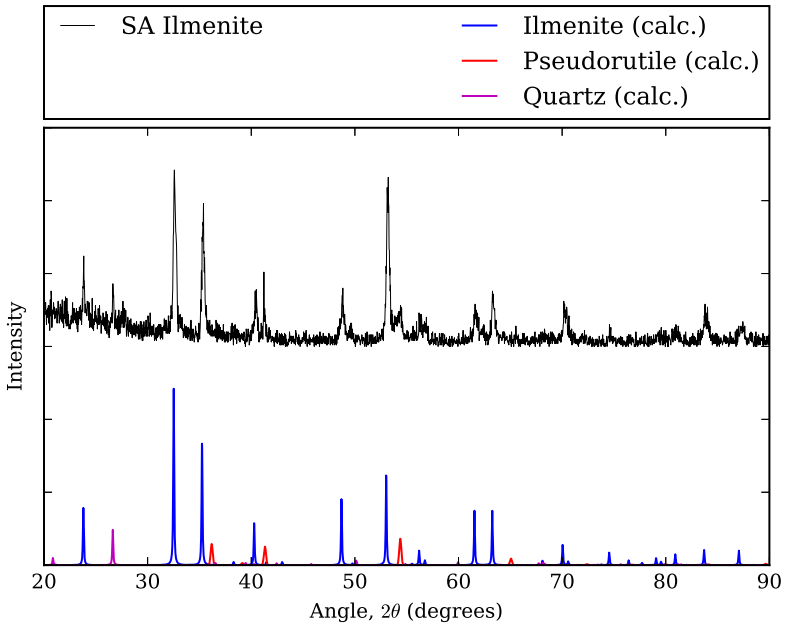

Figure 6.7: XRD Pattern of South African Ilmenite compared to pure compounds.

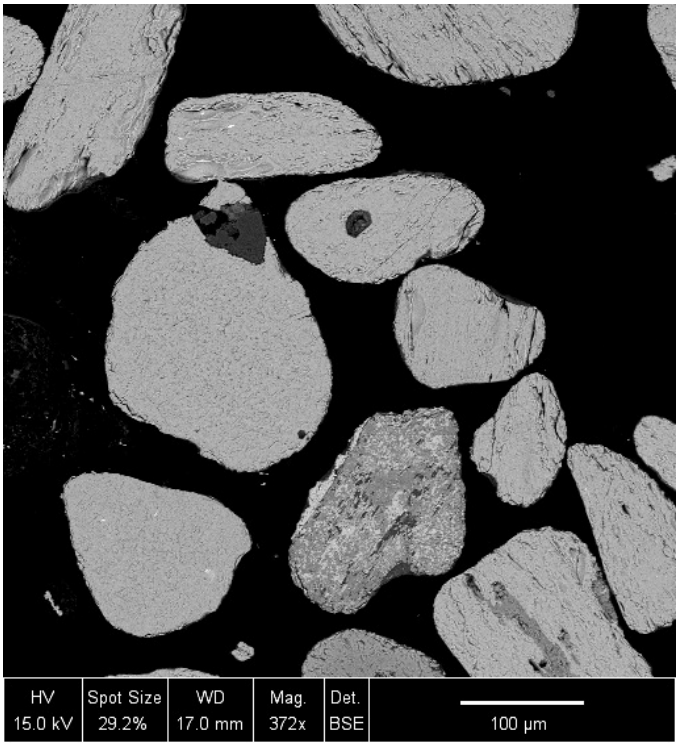

Figure 6.8: Backscattered SEM image of the South African Ilmenite mineral sand

Its x-ray diffraction pattern, shown in Figure 6.9 shows that it is most similar to Ti_3O_5, but not exactly. Titaniferous slags are typically classified as M_3O_5 compounds, where M is typically a mixture of Ti, Fe, and Mn [45]. This is why Ti_3O_5 is not a perfect match for the XRD pattern. Some quartz is also observed in the XRD pattern. SEM of this ore (Figure 6.10) shows almost uniform contrast in backscatter imaging, indicating that the titanium-bearing particles in the slag have uniform composition. There are also dark areas in some of the particles, and EDS shows these particles to be silicon-rich which matches the XRD observations of quartz. There are also bright spots in some particles. These appear to be metallic iron particles that were trapped in the slag during production.

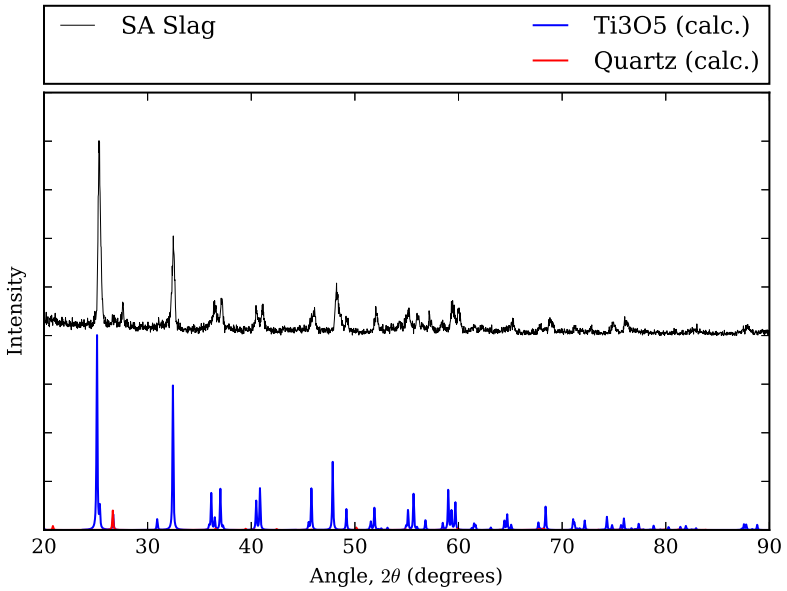

Figure 6.9: XRD Pattern of South African Slag compared to pure compounds.

6.7 Ilmenite Mineral Sand (Madagascar)

The ilmenite mineral sand referred to as QMM Ilmenite (QMM = QIT Madagascar Minerals) is a weathered ilmenite mineral sand. As seen in Table 6.1, the concentrations of both Fe_2O_3 and FeO are reported and Fe_2O_3 is present in larger quantities. The ore is also relatively

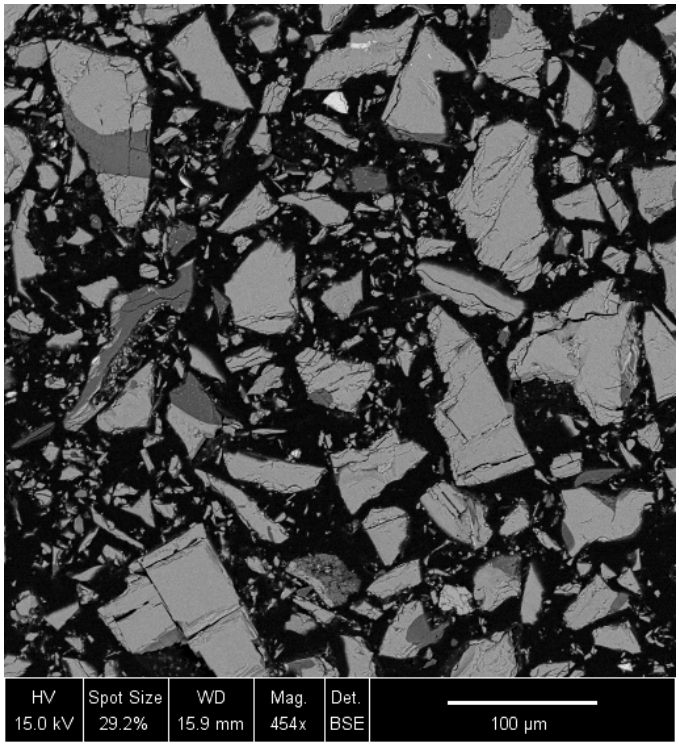

Figure 6.10: Backscattered SEM image of the South African titaniferous slag. Bright particles are metallic iron, dark areas are silica, otherwise M_3O_5.

rich in thorium and uranium (160 ppm). Given the lack of zirconium, it is likely that the radioactivity of this ore is contained within the ore particles, as with the South African ilmenite in Section 6.5.

The x-ray diffraction pattern of this material (Figure 6.11) was very weak. Only the main peaks of ilmenite, pseudorutile, and rutile can be identified over the background. This is again probably due to the fact that this ore is heavily weathered. Backscattered SEM imaging seems to support this (Figure 6.12), as the particles themselves seem to contain both iron rich and poor (or at least less iron rich) regions, in addition to rutile particles.

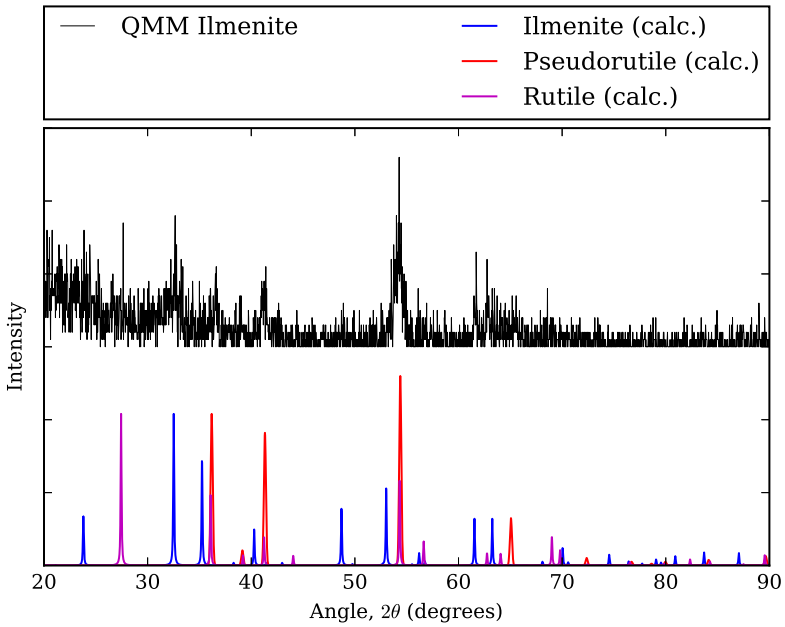

Figure 6.11: XRD Pattern of QMM Ilmenite compared to pure compounds.

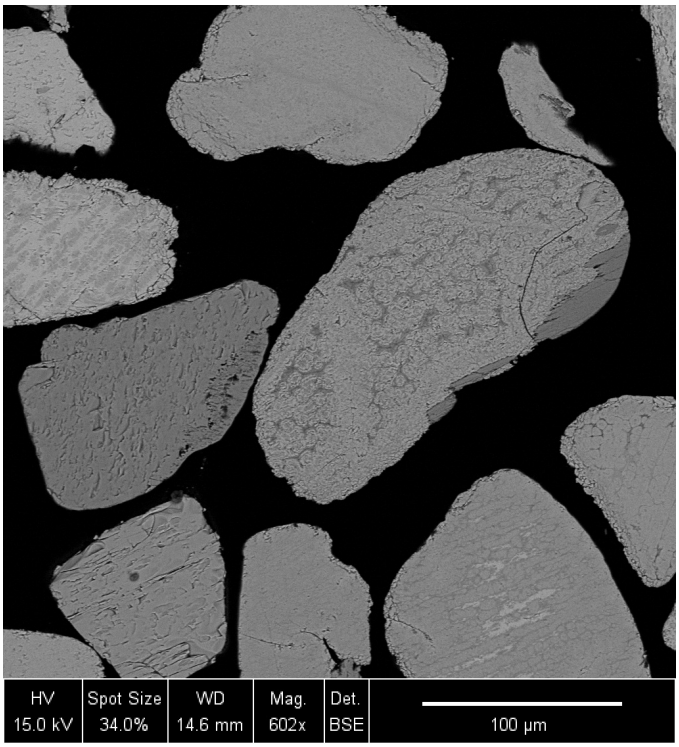

Figure 6.12: Backscattered SEM image of the QMM Ilmenite mineral sand. Brighter areas have higher iron content.

6.8 Titaniferous Slag - RTCS (Canada)

The titaniferous slag samples (received from Rio Tinto) were labeled as RTCS (Rio Tinto Chloride Slag) or QMM Slag. As suggested by the name, this slag has an impurity content low enough (see Table 6.1) to be used directly in chlorination processes for making titanium tetrachloride ($TiCl_4$). Overall, it is similar to the South African slag sample (Section 6.6). Its x-ray diffraction pattern is shown in Figure 6.13, showing a typical M_3O_5 diffraction pattern. Backscatter SEM imaging (Figure 6.14) also shows very homogeneous contrast within the titanium-bearing particles, with silica-containing showing up as dark bands. Some metallic iron can also be observed.

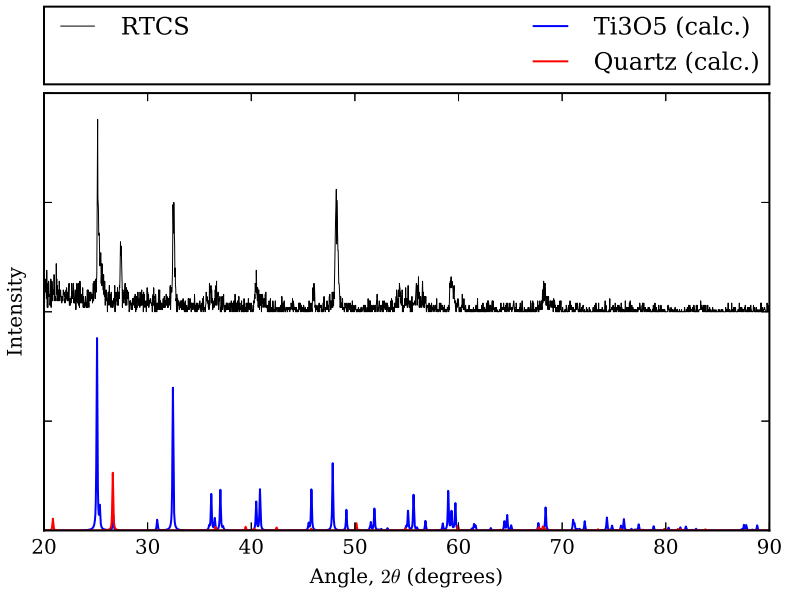

Figure 6.13: XRD Pattern of RTCS Slag compared to pure compounds.

6.9 UGS (Canada)

The UGS (Upgraded Slag) results from a process which utilizes a high pressure acid leach on thermally treated titaniferous slag to upgrade slag into what is essentially a silica-rich

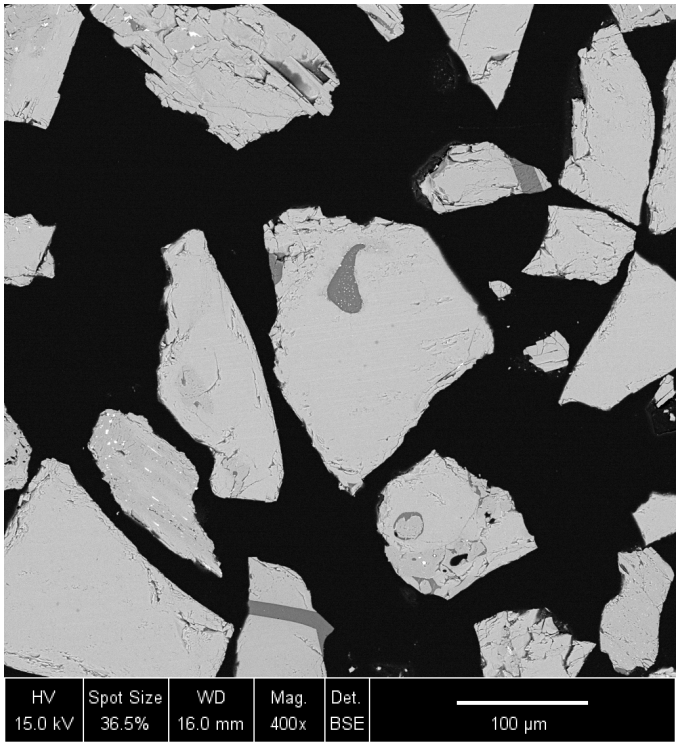

Figure 6.14: Backscattered SEM image of the RTCS slag. Bright areas are M_3O_5, dark areas are silica.

natural rutile [46]. From Table 6.1, we can see its TiO_2 content is 94.5 weight %, just shy of the common 95% threshold for synthetic rutile.

X-ray diffraction on this material (Figure 6.15) shows that it is a perfect match for rutile, despite the presence of 1.8 weight % silica. In other silica-rich samples, quartz peaks were often visible. Backscattered SEM imaging (Figure 6.16) shows the sample looks like a slag (angular particles), except porous. This also includes dark bands (which are identified as silicon-rich). It is currently unknown as to why such a high silica content is not showing up in the XRD diagram; the silicates may be amorphous. EDS shows that the occasional non-porous particle is iron-rich. This likely is the source of the 1.4 % iron shown in Table 6.1. The particle size varies from 1 mm to around 50 µm, with an average around 300 µm. This broadly agrees with the size range for chlorination feed, which is approximately 75-850 µm [46].

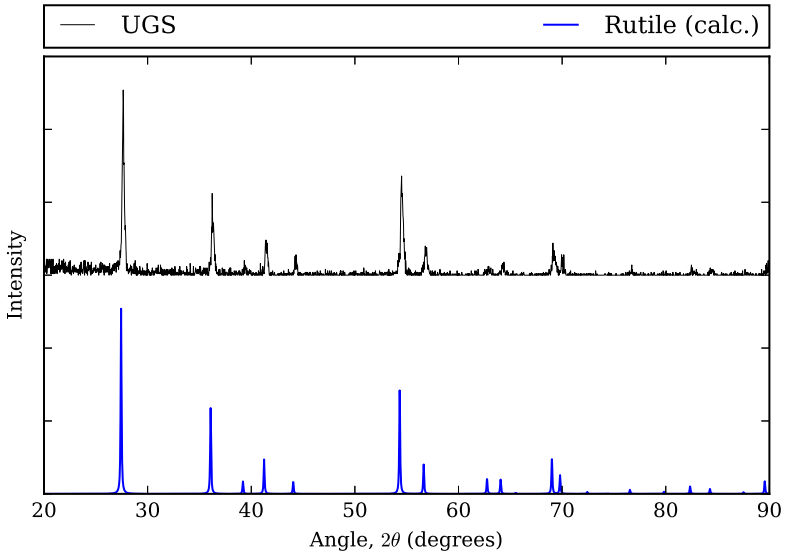

Figure 6.15: XRD Pattern of RTCS Slag compared to pure compounds.

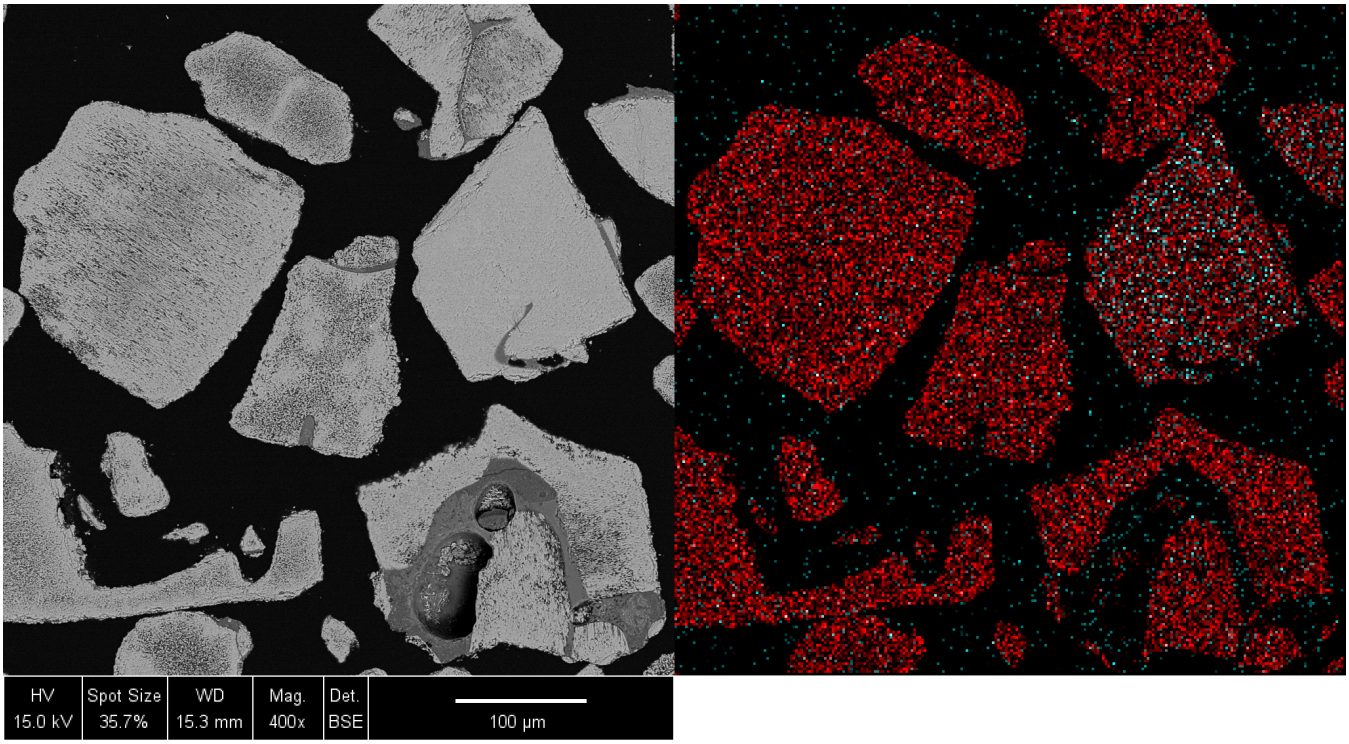

Red = Titanium, Cyan = Iron

Figure 6.16: Backscattered SEM image and EDS of UGS. Bright areas in SEM image are TiO_2 and dark areas are silica. Non-porous particles tend to contain iron.

6.10 Panzhihua Ilmenite (China)

Ilmenite mineral sand obtained from the Panzhihua region of China is a mostly unweathered deposit, meaning it is high in FeO, and is unique in the fact that it contains an abnormally high concentration of MgO. This MgO is likely in the form of the mineral geikielite, which has the chemical formula $MgTiO_3$. Geikielite and ilmenite tend to form a solid solution [47]. However, this is not evident in the X-ray diffraction pattern (Figure 6.17)—which shows that the sample is almost entirely pure ilmenite—though this is likely due to the fact that the geikielite fraction is too small to cause a noticeable peak shift in the XRD pattern.

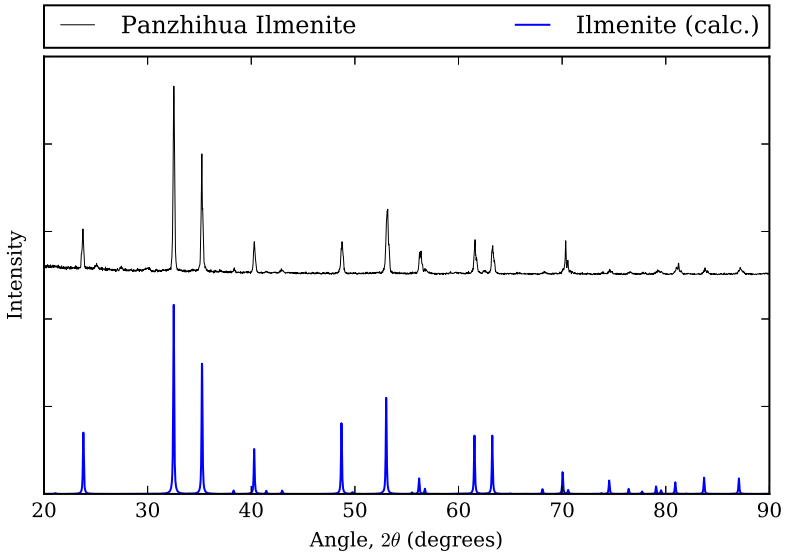

Figure 6.17: XRD Pattern of Panzhihua Ilmenite compared to pure compounds.

Chapter 7

Oxycarbide Production

This chapter, discusses carbothermal reduction of titanium oxycarbide from the various materials described in Chapter 6. Multiple factors have a significant effect on the production of titanium oxycarbide, including particle size, particle porosity, impurity content, and reductant.

Not all the ores described in Chapter 6 were converted to titanium oxycarbide. The ores used were mostly converted by the conventional method of carbothermal reduction with a source of solid carbon, but some work was also performed on methane-hydrogen gas mixtures as a reducing agent for some ores—carried out by Dr. Jie Dang, a visiting researcher.

7.1 Pigment Oxycarbides

As stated before, making titanium oxycarbide from pigment is relatively easy. While the carbothermal reduction step to make titanium oxycarbide is normally performed at 1600 °C with most titanium ores, for pigment, a temperature of 1400 °C was sufficient. This is due to the small particle size of the pigment particles, and because there are no other impurities that need to be removed.

Using normal carbothermal reduction techniques at 1400 °C, the product was generally close to pure oxycarbide, with a very small amount of unreacted Ti_2O_3 usually present, as shown in Figure 7.1. The likely cause of unreacted TiO_2 is poor mixing of the carbon into the pigment. If methane reduction is used, the reaction can be carried out around 1200 °C. However, a small amount of metallic iron needs to be present in the sample in order to catalyze the decomposition ("cracking") of methane. With methane reduction, the result is usually pure oxycarbide, once the iron catalyst is removed (usually by magnetic separation).

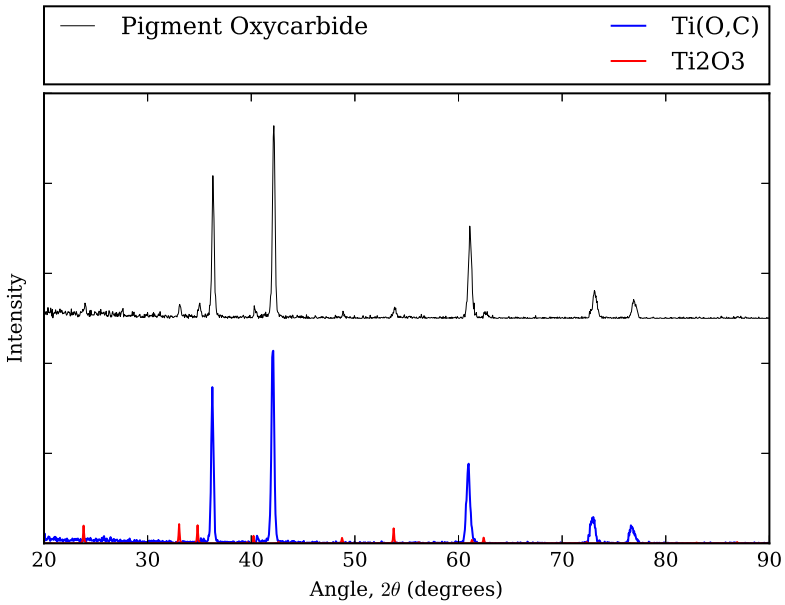

Figure 7.1: XRD Pattern of pigment titanium oxycarbide (reduced at 1400 °C) compared to pure compounds.

SEM of the oxycarbide shows a decrease in particle size relative to the starting material. This is expected, as the removal of oxygen during reduction increases porosity. Figure 7.2 illustrates the smaller particle size of titanium oxycarbide shown alongside coarser particles of Ti_2O_3. The increased porosity would significantly increase the surface area of the oxycarbide, potentially allowing for faster dissolution when used as a consumable anode material.

However, porosity can potentially be a problem if evolved carbon monoxide (during electrolysis) fills these pores. Trapped CO would increase the likelihood of anode flotation, where the overall anode pellet density is less than the electrolyte density.

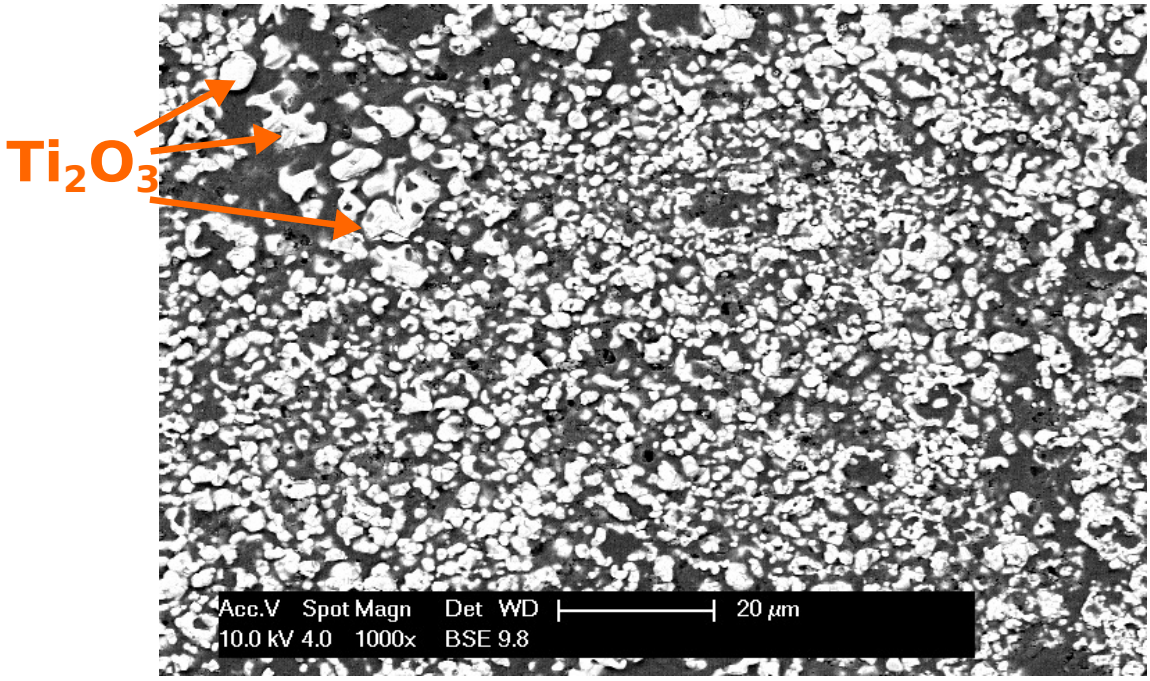

Figure 7.2: Backscattered SEM image of titanium oxycarbide produced from pigment (reduced at 1400 °C). Finer particles are oxycarbide.

7.2 Titanium Oxycarbide from Leucoxene and Natural Rutile

Attempts to make titanium oxycarbide directly from leucoxene (and natural rutile) under typical reaction conditions (1600 °C for 2 hours) always yielded incomplete reduction. This is readily seen by x-ray diffraction (Figure 7.3). Analysis of the XRD pattern shows that the material is a mixture of Ti_2O_3 and titanium oxycarbide (the broad peak centered on 2θ = 26° is from unreacted carbon black). SEM of this sample (Figure 7.4) showed a distinct

The content of this section has also been described in my paper: "Production of Titanium Oxycarbide from Titania-Rich Mineral Sands" [48].

core and shell in partially reduced particles, indicating that the kinetics of this reaction is limited by pore diffusion. If pore diffusion is rate limiting, a reduction in particle size would increase reaction rate. The natural rutile (leucoxene) particles had an average particle size of 100 μm.

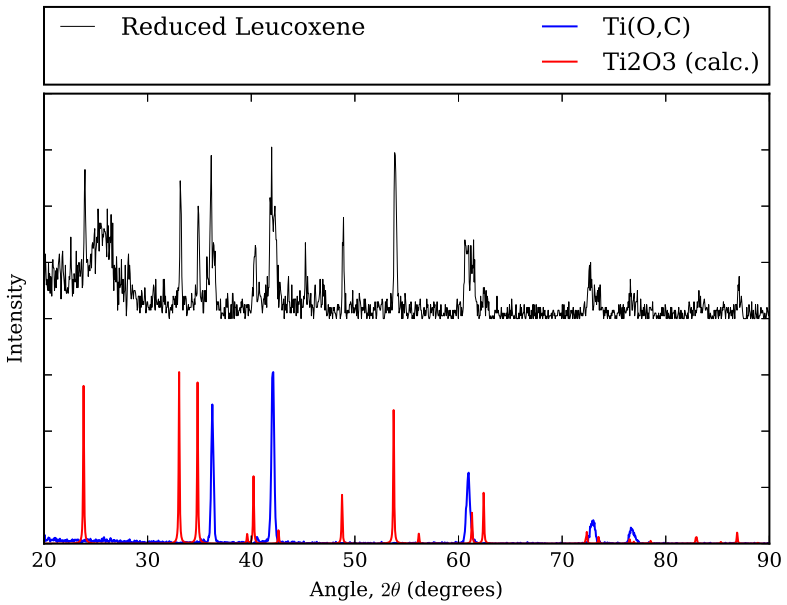

Figure 7.3: XRD Pattern of reduced leucoxene mineral sand (incomplete oxycarbide reaction) compared to pure compounds.

Grinding the particles down to approximately 50 μm (using particles between 38 and 63 μm), allowed full reduction to occur in the normal 2 hour holding time, as seen in the x-ray diffraction pattern in Figure 7.5. Most of the sample is titanium oxycarbide, with a small fraction of it remaining as Ti_2O_3, which is likely the unreacted cores of the largest particles. A longer reaction time, or using even finer particles (less than 50 μm) should produce almost pure titanium oxycarbide for these reduction conditions.

Iron in the reduced material can in principle be removed by magnetic separation, as the iron has been reduced to metallic form. However, due to the relatively high silica content (at least compared to the iron oxide content) in the feed material the typical metallic product was

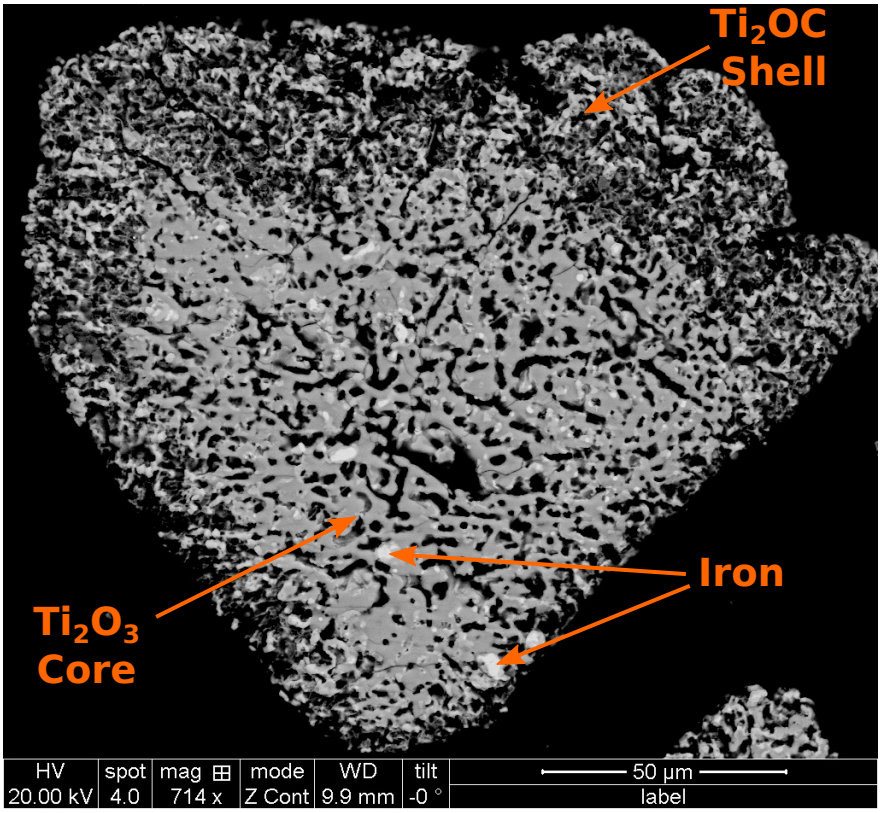

Figure 7.4: Backscattered SEM image of partially-reduced leucoxene particle showing shrinking-core behavior.

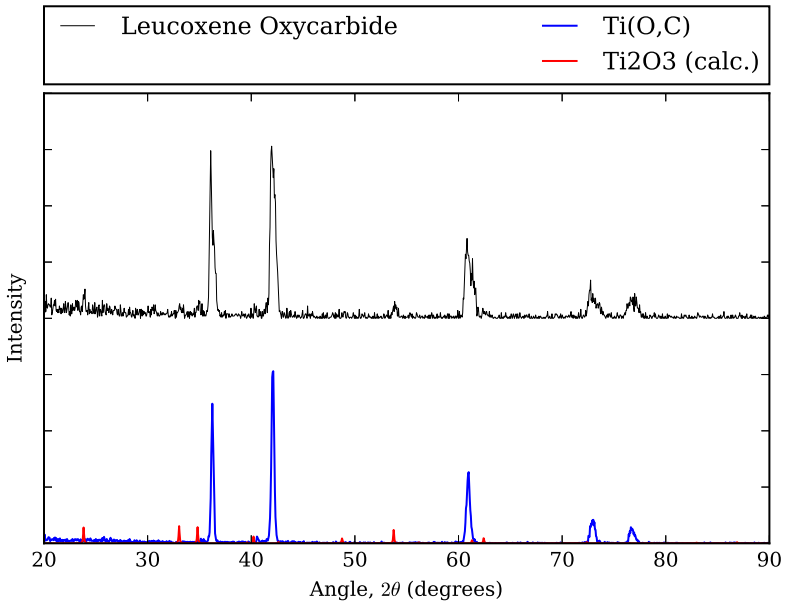

Figure 7.5: XRD Pattern of leucoxene oxycarbide compared to pure compounds.

an iron-silicon alloy. X-ray diffraction (Figure 7.6) shows that the magnetically separated component consists of titanium oxycarbide, the iron-silicon intermetallic compound Fe_5Si_3 (η-phase in the Fe-Si system), and silicon carbide (SiC).

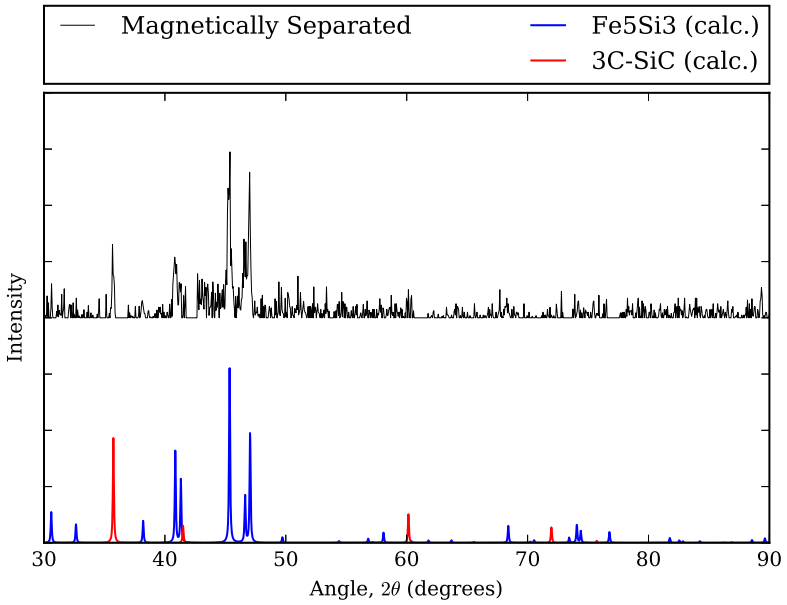

Figure 7.6: XRD Pattern of material magnetically separated from leucoxene oxycarbide compared to pure compounds (titanium oxycarbide peaks removed).

The intermetallic compound Fe_5Si_3 is a high temperature phase in the iron-silicon system. However, as seen in the iron-silicon phase diagram in Figure 7.7, it is not the equilibrium stable phase at 1600 °C, nor at room temperature. A combination of Fe_5Si_3 and SiC can form from a Fe-Si-C melt (formed during reduction at 1600 °C) upon subsequent cooling. As Figure 7.8 shows, Fe_5Si_3 and SiC form a stable mixture at 850 °C [49]. However, this is fortuitous as Fe_5Si_3 is ferromagnetic up to 373—385 K [50], allowing the Fe_5Si_3 to be removed, together with any attached SiC, using only magnetic separation.

Magnetic separation would tend to decrease yield: if a particle of Fe_5Si_3 is attached to or otherwise embedded in a titanium oxycarbide particle, then the whole oxycarbide particle will be removed, potentially decreasing yield. However, yields of approximately 90% have

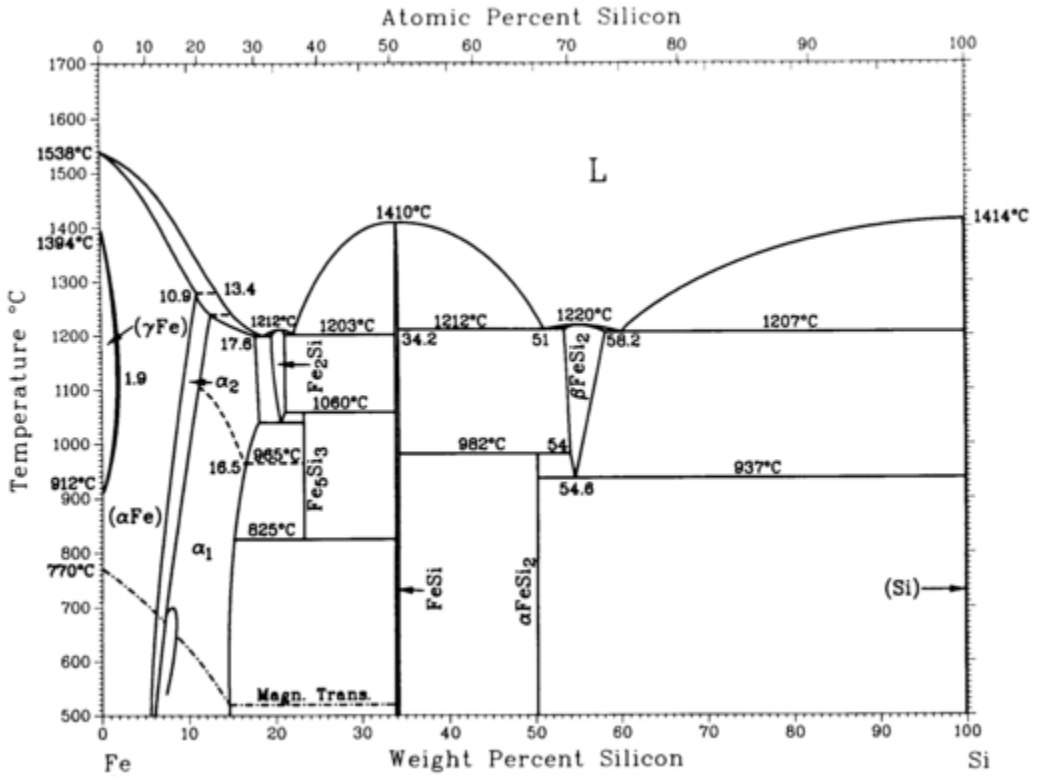

Figure 7.7: The Fe-Si Phase Diagram [51]

been achieved using this technique of magnetic separation with leucoxene-based oxycarbides.

7.3 Pseudorutile Oxycarbide

The same techniques described in Section 7.2 were applied to the production of titanium oxycarbide from pseudorutile mineral sand. However, these experiments were performed without grinding, as the existing porosity of the material would help with gas diffusion, and due to increased porosity, larger particles can be reduced for the same reaction time. It was also expected that the denser iron-rich particles would also become porous as the iron is reduced to metallic form and removed.

The results of initial testing showed extensive titanium oxycarbide production, but also the

The content of this section has also been described in my paper: "Production of Titanium Oxycarbide from Iron-Rich Titanium Ores" [52].

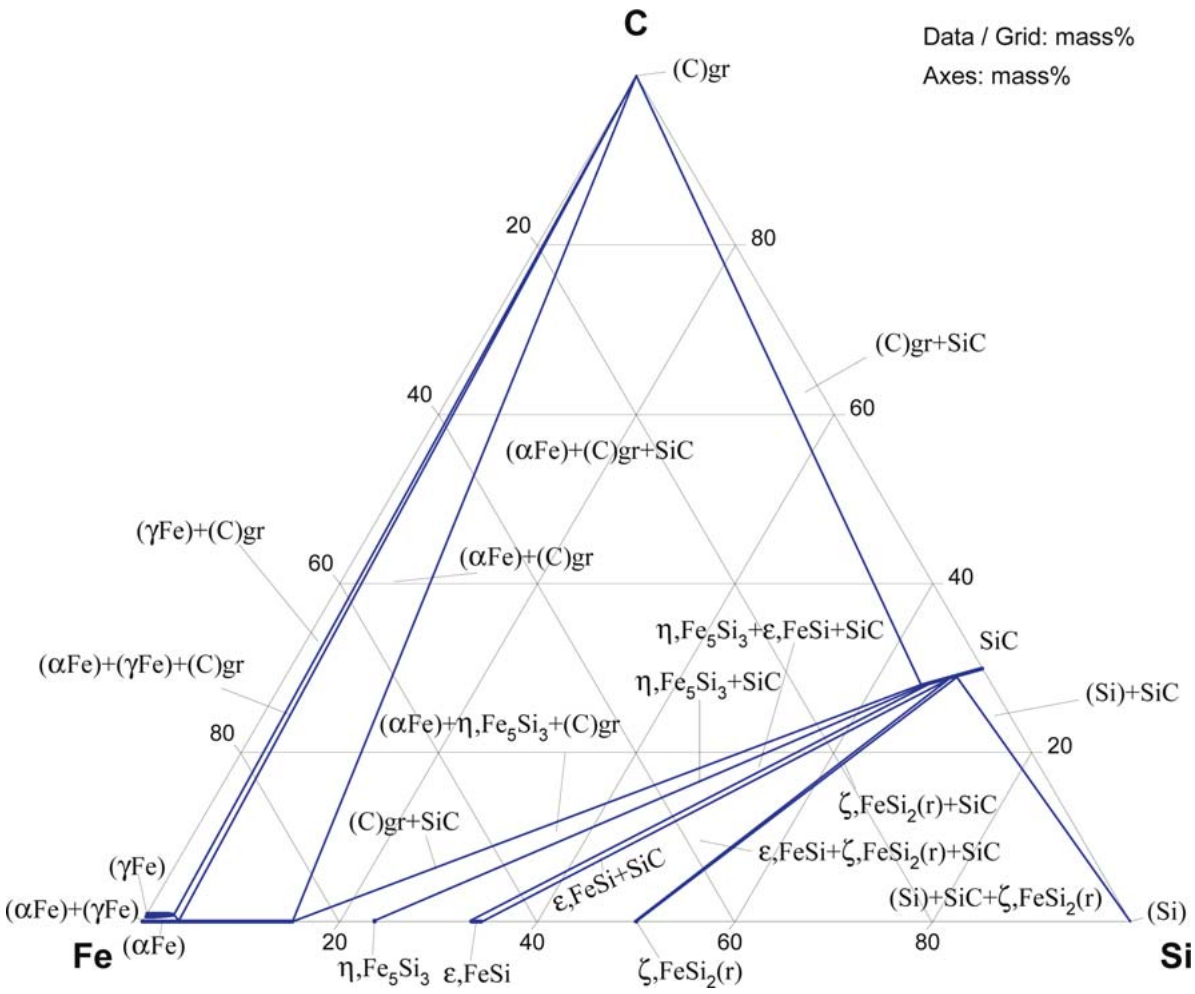

Figure 7.8: Isothermal section of C-Fe-Si Phase Diagram (800 °C) [49]

presence of titanium(III) oxide and metallic iron, as seen in the XRD pattern in Figure 7.9. SEM images of the powder showed full reduction in some particles which were over the previous 50 µm size limit, showing that existing porosity may help with the reduction of larger titania particles as expected. However, there were other particles of similar or smaller size which appeared to show core-shell behavior, with titanium oxycarbide surrounding a core of titanium(III) oxide. Closer examination of the core-shell interface (Figure 7.10) showed the presence of a phase which appeared dark under backscatter imaging. EDS of this boundary showed it to be very high in alumina, suggesting that alumina had precipitated at the grain boundary.

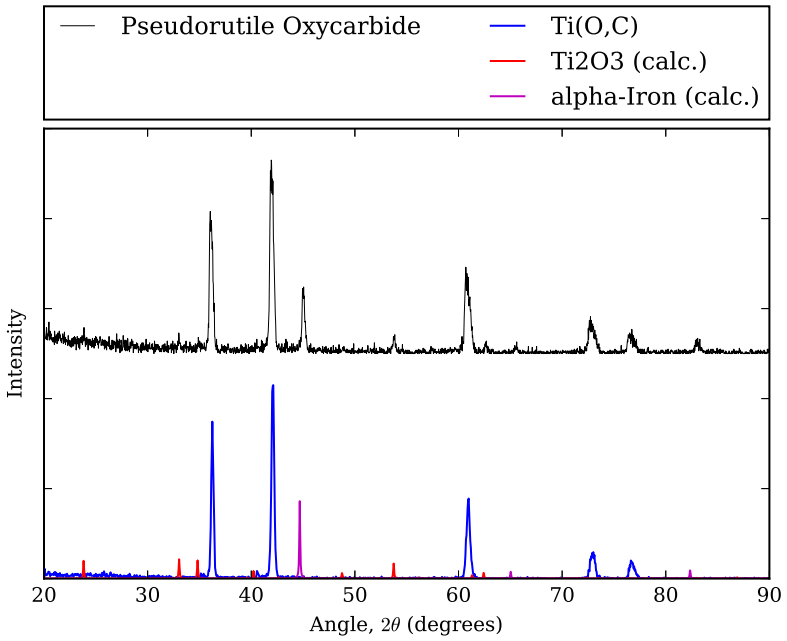

Figure 7.9: XRD Pattern of reduced pseudorutile mineral sand.

The current hypothesis is that the particles which exhibited this alumina precipitation phenomenon were the particles which were high in aluminum impurities to begin with. Based on all the oxycarbides examined in this work, titanium oxycarbide has no solubility for aluminum. As a result, during reduction, the aluminum oxide will remain in titanium(III) oxide. The phase diagram in Figure 7.11, shows around 20 mol% solubility of alumina in

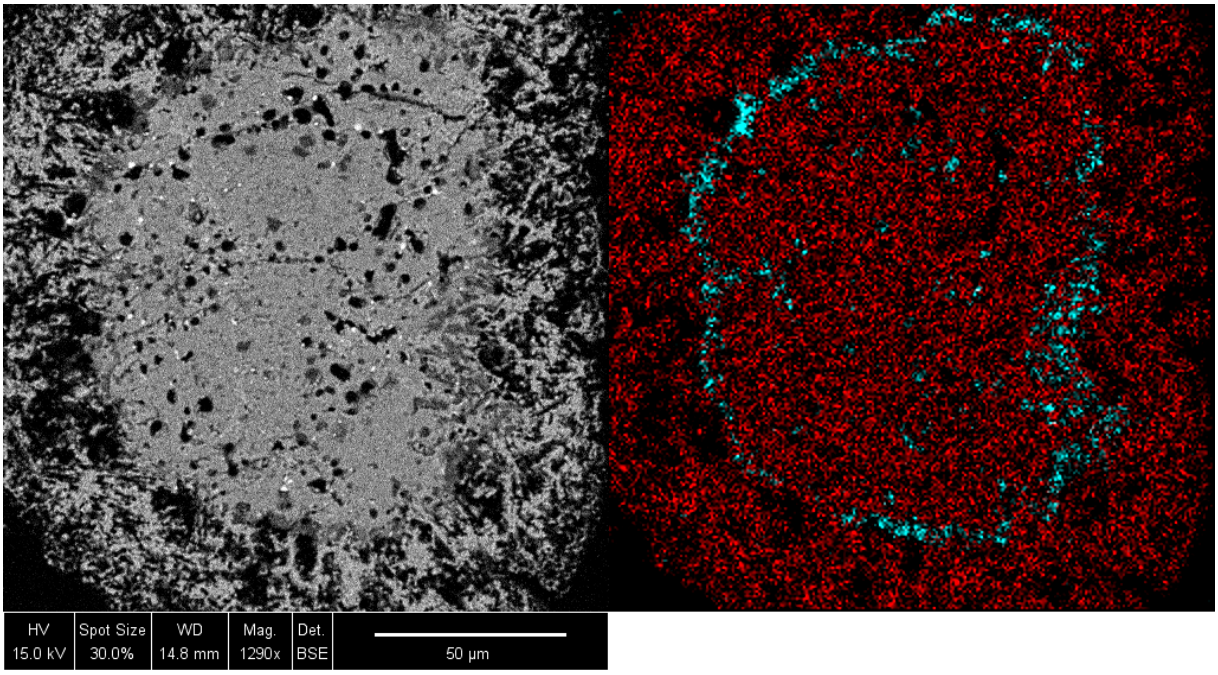

Red = Titanium, Cyan = Aluminum

Figure 7.10: Backscattered SEM image and EDS of a Florida pseudorutile oxycarbide particle showing alumina "rim".

titanium(III) oxide. During the reaction of titanium(III) oxide to titanium oxycarbide, any aluminum oxide present will remain at the reaction front, as it is soluble in the titanium(III) oxide and not the titanium oxycarbide. Over time, the alumina concentration will increase until it reaches saturation, where it will precipitate at the reaction front (the point of highest concentration). It is expected that precipitation of alumina would slow further reduction, and decrease overall oxycarbide yield.

Unlike in the oxycarbide produced from leucoxene mineral sands, the iron from the pseudorutile oxycarbide does not separate from the oxycarbide. This may be partially due to particle size. The leucoxene oxycarbide materials had a particle size of approximately 50 µm, but the pseudorutile particle size is on the order of 150 µm.

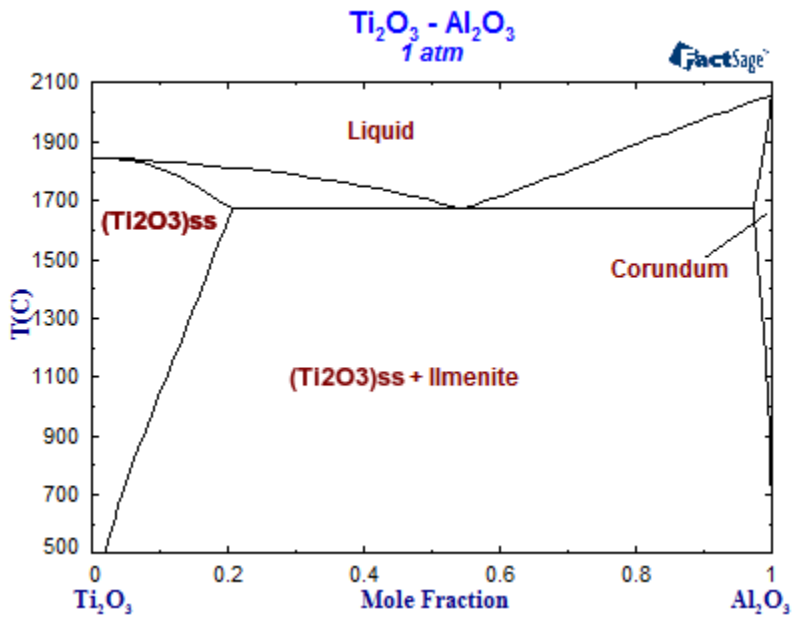

Figure 7.11: The Al_2O_3-Ti_2O_3 Phase Diagram (calculated from FactSage)

7.4 UGS Oxycarbide

The methods developed in Section 7.2 for leucoxene oxycarbide were applied to the UGS material. Without grinding or other kind of size reduction, this material is not expected to fully reduce, as it has an average particle size of 300 μm, with some particles being as large as 800 μm or more. For this reason, the material was ground for 3 minutes in a tungsten carbide "ring and puck"-style grinder to produce a fine powder.

When these standard reaction conditions were applied to the UGS material, an almost fully reduced product was obtained, as expected. An x-ray diffraction pattern of this material (Figure 7.12) shows the presence of titanium oxycarbide, with trace amounts of Ti_2O_3, Fe_5Si_3, and cubic SiC, the same compounds as the leucoxene oxycarbide described in Section 7.2. However, unlike the leucoxene, there is significantly more silica and less iron in the UGS; this might be expected to produce a higher silicon phase of iron, or more SiC. Neither of these is present. Indeed, the ratio of Fe_5Si_3 to SiC looks similar to the leucoxene oxycarbide in Figure 7.6. This is confirmed by magnetically separating the oxycarbide and analyzing

the magnetic fraction, shown in Figure 7.13 which shows pure-phase Fe_5Si_3, with no SiC.

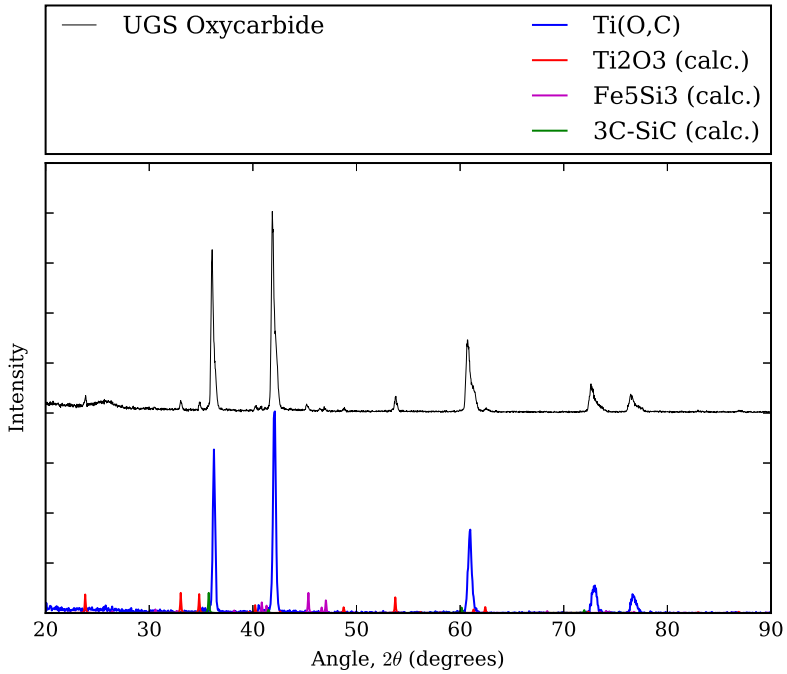

Figure 7.12: XRD Pattern of reduced UGS compared to pure compounds.

The lack of excess silicon-containing phases might be explained by a single phenomenon. Table 6.1 shows that the UGS material had a significantly higher MgO content than the natural rutile, leucoxene, and pseudorutile. During reduction Al_2O_3, MgO, and SiO_2 may have reacted to form a liquid. As seen in the phase diagram in Figure 7.14, the combination of MgO, SiO_2, and Al_2O_3 in the UGS material would produce a low-melting point mixture (liquidus temperature around 1400 °C).

Due to the low levels of overall iron present in these samples, these samples could also be subjected to magnetic separation to remove the Fe_5Si_3 particles in a similar fashion to the natural rutile and leucoxene oxycarbides described in Section 7.2. By this method, almost all of the iron and silicon was removed. The final composition of this magnetically separated material is shown in Table 7.1. This composition shows that the ratio of elements in this material almost meets what would be required to achieve ASTM Grade 2 specifications. However, the vanadium content is too high at 0.37 weight percent (ASTM Grade 2 specifies

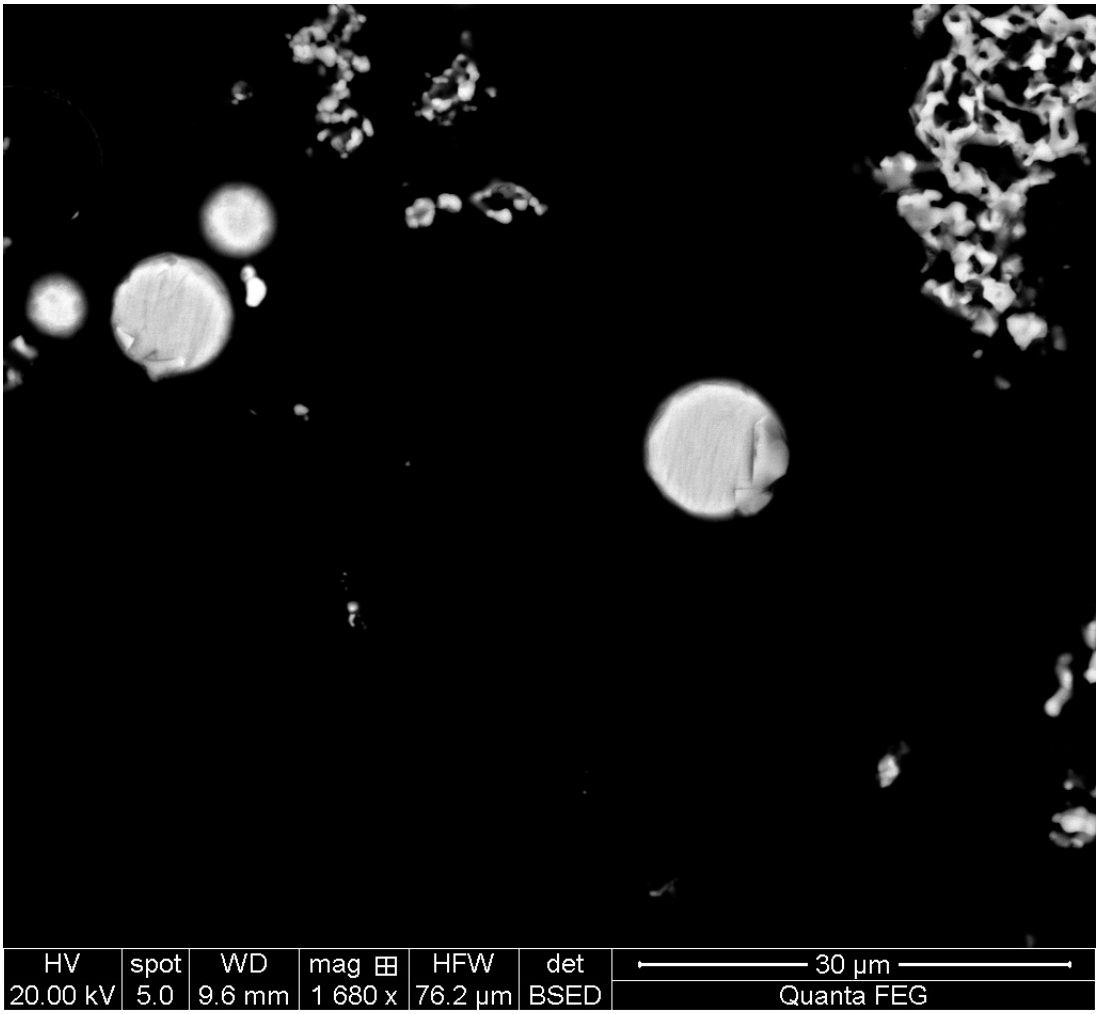

Figure 7.13: Backscattered SEM image of magnetically separated material from UGS oxycarbide showing single phase Fe_5Si_3 particles (round particles).

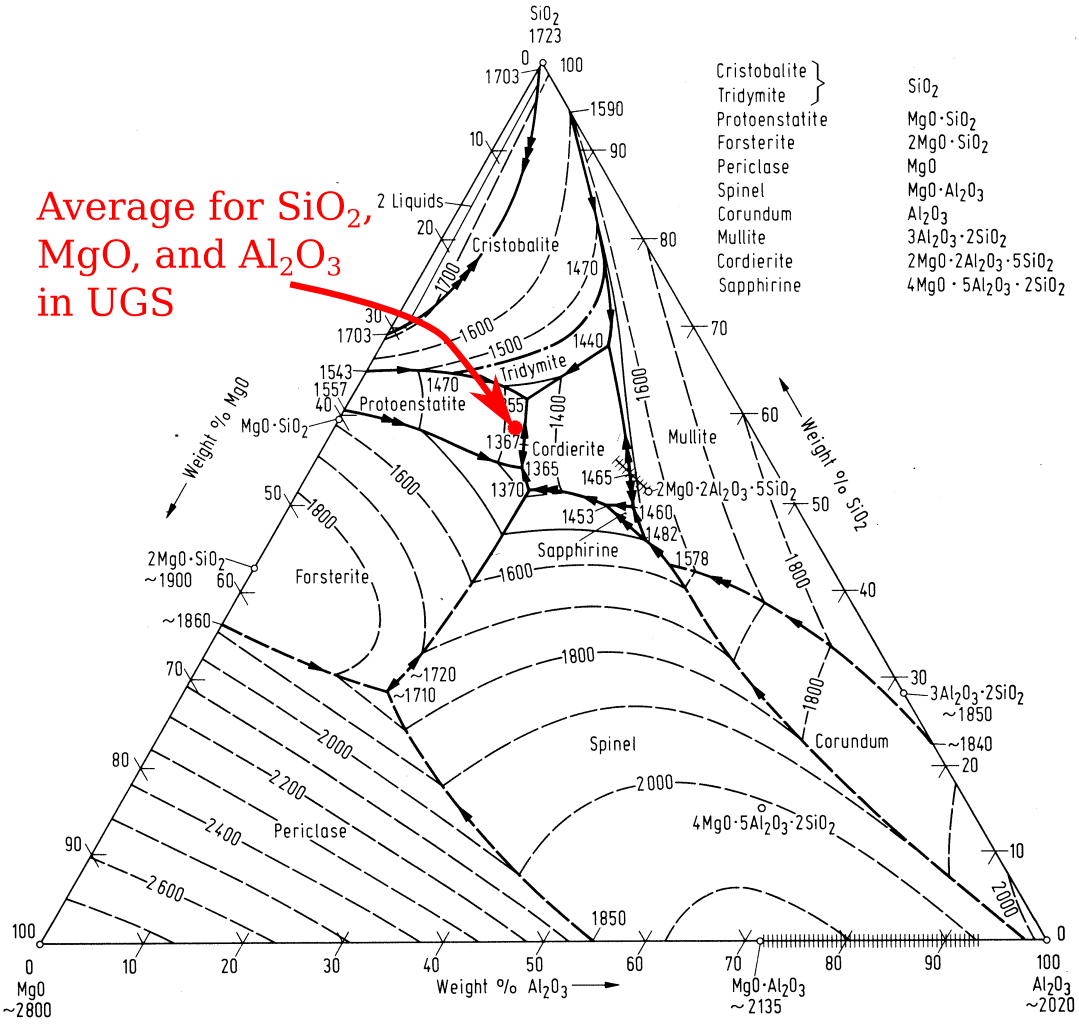

Figure 7.14: The Al_2O_3-MgO-SiO_2 Phase Diagram (Liquidus projection) [53]

all nonferrous metallic impurities must be below 0.1 weight percent). Given the high vanadium content of this ore, this material could be used as the basis of other titanium alloys which contain vanadium, such as ASTM Grade 5 (Ti-6Al-4V).

7.5 Ilmenite Oxycarbides

Experiments were also performed on both the South African and Panzhihua ilmenite mineral sands to convert them into titanium oxycarbide. First, both materials were ground for 3 minutes and mixed with the stoichiometric amount of carbon (plus 10%).

The resulting materials were analyzed by XRD. The South African ilmenite (Figure 7.15) behaved entirely as expected, resulting in almost complete conversion to titanium oxycarbide and iron. On the other hand, the Panzhihua ilmenite displayed some odd—but not unexpected behavior—as shown in Figure 7.16. The Panzhihua ilmenite was almost fully converted to titanium oxycarbide and iron, with some impurity peaks corresponding to Ti_2O_3.

As previously discussed in Section 6.10, the relatively high MgO content of the Panzhihua ore is likely a solid solution of ilmenite and geikielite. During the reduction, the iron in the ilmenite would be reduced, enriching the ilmenite in MgO (which cannot be reduced by carbon easily). Increased MgO concentration in the ilmenite-geikielite solution is expected to retard reduction. Persistence of geikielite in the reduced material cannot be discerned in the XRD pattern in Figure 7.16 due to the fact that ilmenite and geikielite peaks overlap

Table 7.1: Composition of the UGS oxycarbide after magnetic separation compared to original ore. Only reducible impurities shown. Normalized to 100%; all quantities in mass percent.

Material	Ti	Fe	Cr	Mn	Si	V
Original UGS	96.39	1.67	0.08	0.05	1.43	0.38
UGS Oxycarbide (non mag.)	99.4	0.21	—	—	0	0.37

with Ti_2O_3.

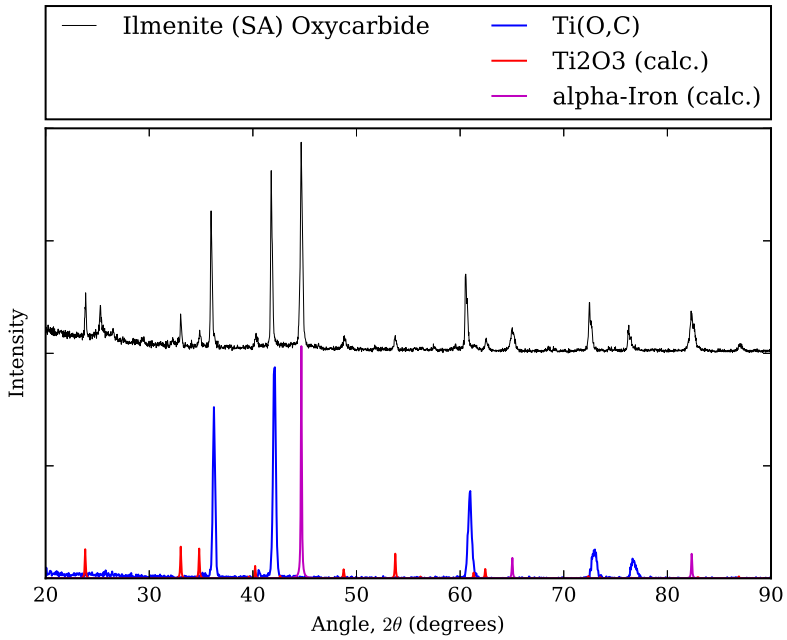

Figure 7.15: XRD Pattern of titanium oxycarbide made from South African Ilmenite compared to pure compounds.

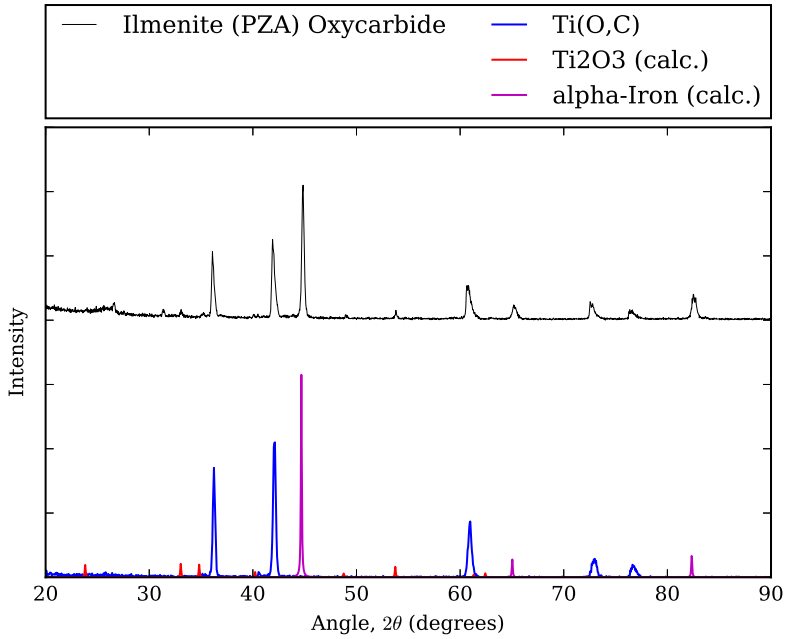

Figure 7.16: XRD Pattern of titanium oxycarbide made from Panzhihua (PZA) Ilmenite compared to pure compounds.

7.6 Methane Reduction of Ilmenite and Titaniferous Slag (South Africa)

Jie Dang—a visiting researcher in our laboratory in 2012-2013—performed experiments using methane gas mixtures (typically 8% CH_4-55% H_2-bal. Ar) to reduce of South African ilmenite mineral sands for 1.5 hours at 1200 °C. The result was the iron was fully reduced to metallic form, and the titanium ore itself was reduced to Ti_3O_5, as seen from the XRD pattern in Figure 7.17.

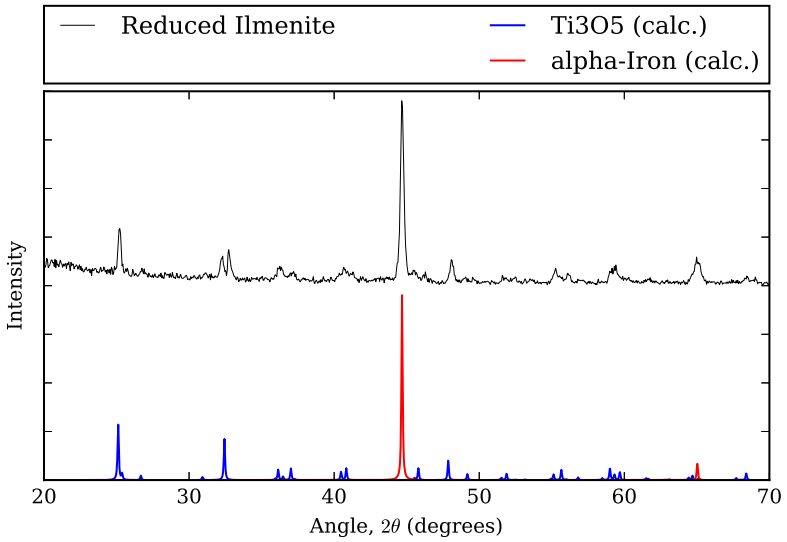

Figure 7.17: XRD Pattern of methane-reduced South African ilmenite (1200 °C for 1.5 hours).

SEM of this sample (Figure 7.18) confirms the iron has been reduced to the metallic form. The actual form of the iron (lamellar) is as observed in the reduction of other ilmenites [54]. This structure is not expected to persist for oxycarbide forming reactions using solid carbon, which use much higher temperatures. At 1600 °C, the iron will be molten, and the iron may agglomerate and spheroidize, or the iron may simply leak out.

Similar experiments were run using South African titaniferous slag, using methane reduction for 5 hours at 1200 °C. The result was the iron was fully reduced to metallic form and the

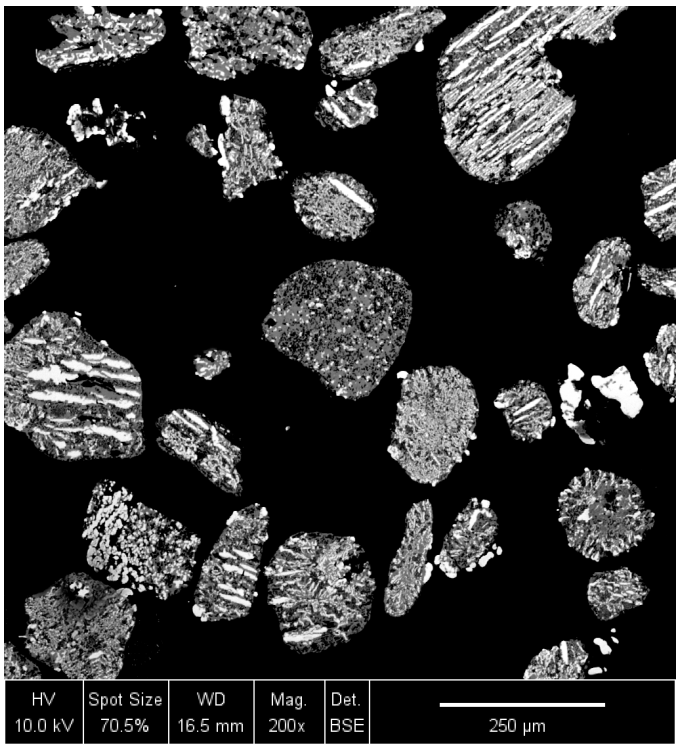

Figure 7.18: Backscattered SEM image of methane-reduced South African ilmenite (1200 °C for 1.5 hours). Bright areas are metallic iron.

titanium ore itself was reduced to Ti_2O_3, as seen from the XRD pattern in Figure 7.17. Quartz was also present in the XRD pattern.

SEM of this sample (Figure 7.20) shows a similar "rim" effect to that of pseudorutile oxycarbide (Figure 7.10). However in this case, the rim that has inhibited the oxycarbide reaction consists of silica. It is unclear as to whether this behavior would also affect solid carbon reduction at the higher temperature of 1600 °C. At this temperature, the iron would be molten, and better able to dissolve silicon.

It may be possible to remove the excess silica in a different manner. The slag is rich in three "inert" oxides - Al_2O_3 (0.58 wt%), CaO (0.35 wt%), and SiO_2 (3.75 wt%). As with UGS oxycarbides (Section 7.4), these oxides can mix to form a liquid slag, and thus remove silica from the system. Based on the phase diagram in Figure 7.21, with the right amount of Al_2O_3 and CaO additions, a low-temperature oxide slag can be made, which might drain out

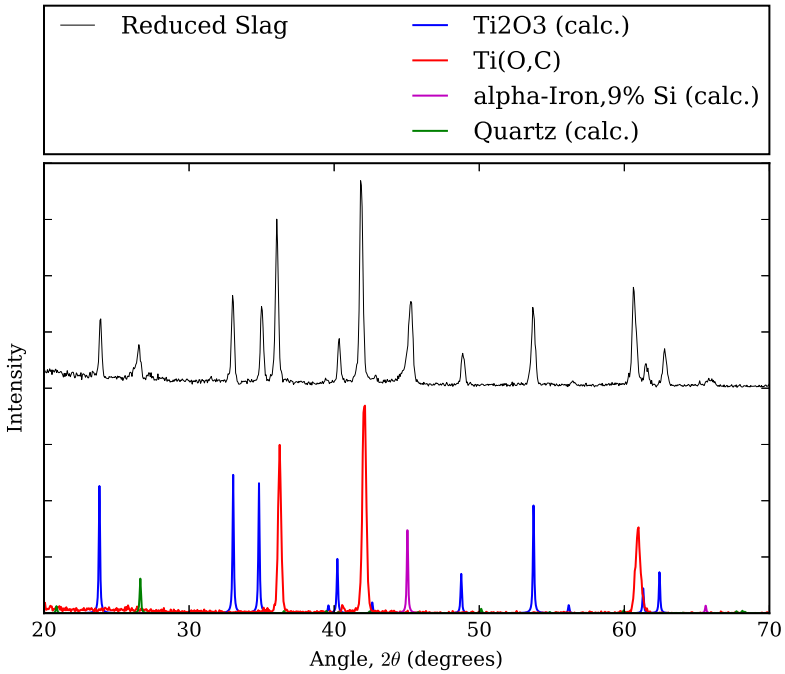

Figure 7.19: XRD Pattern of methane-reduced South African slag (1200 °C for 1.5 hours).

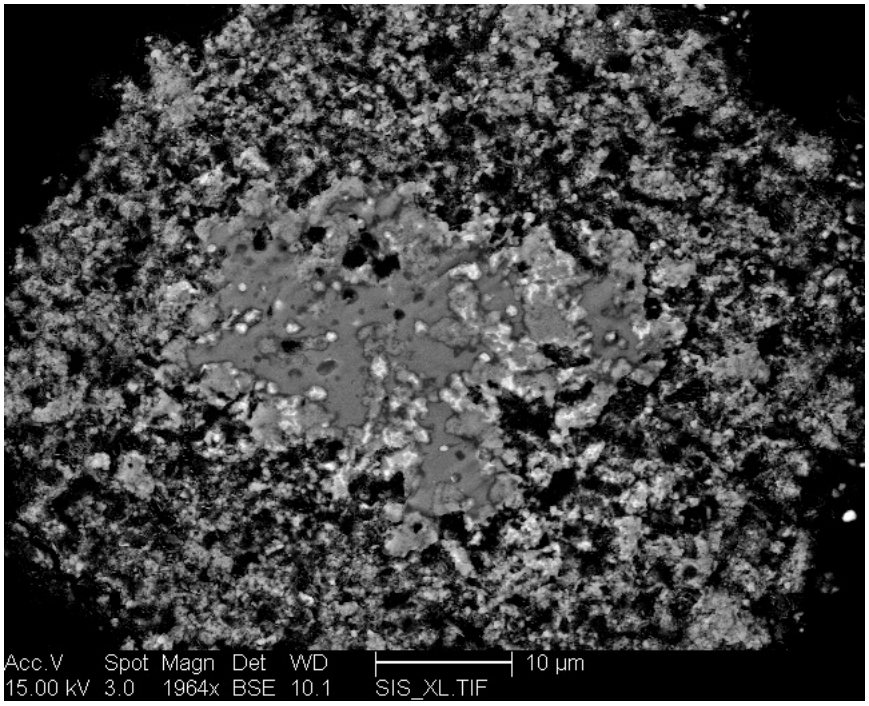

Figure 7.20: Backscattered SEM image of methane-reduced South African slag (1200 °C for 1.5 hours), showing porous titanium oxycarbide shell and dense Ti_2O_3 core. Dark phase around core is SiO_2.

of the material, leaving the oxycarbide reaction front clean. This sort of oxide liquidation would likely behave best in titanium slags, which have a uniform composition in all particles, meaning the treatment would behave the same throughout the sample. In theory the same principle can be applied to the RTCS slag, except as that material is rich in MgO and not CaO, the Al_2O_3-MgO-SiO_2 phase diagram in Figure 7.14 should be used instead.

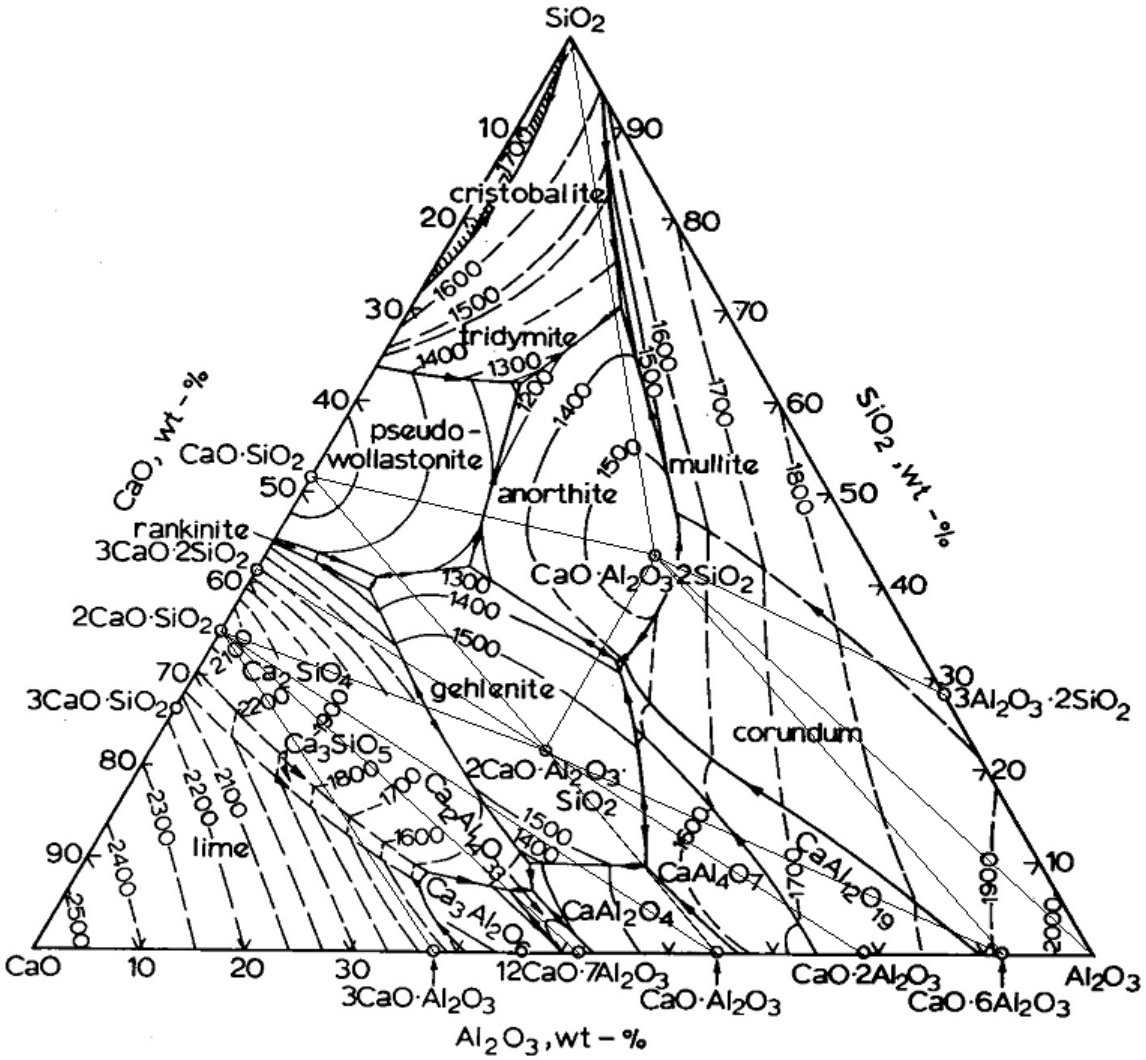

Figure 7.21: The Al_2O_3-CaO-SiO_2 Phase Diagram (Liquidus projection) [55]

7.7 Vanadium Oxycarbide

Vanadium oxycarbide was also synthesized to determine its anode potential and polarization behavior. While vanadium oxycarbide is known to be a solid solution [56] of vanadium(II) oxide and vanadium carbide, the solution thermodynamics of the vanadium-carbon-oxygen are not well characterized. However, a regular solution model was developed from the anodic dissolution potential (determined in Section 10.3.1) of the material synthesized in these experiments. Using this solution model, a phase diagram (Figure 7.22) and plot of $\frac{X_{CO}}{X_{CO_2}}$ (Figure 7.23) was obtained.

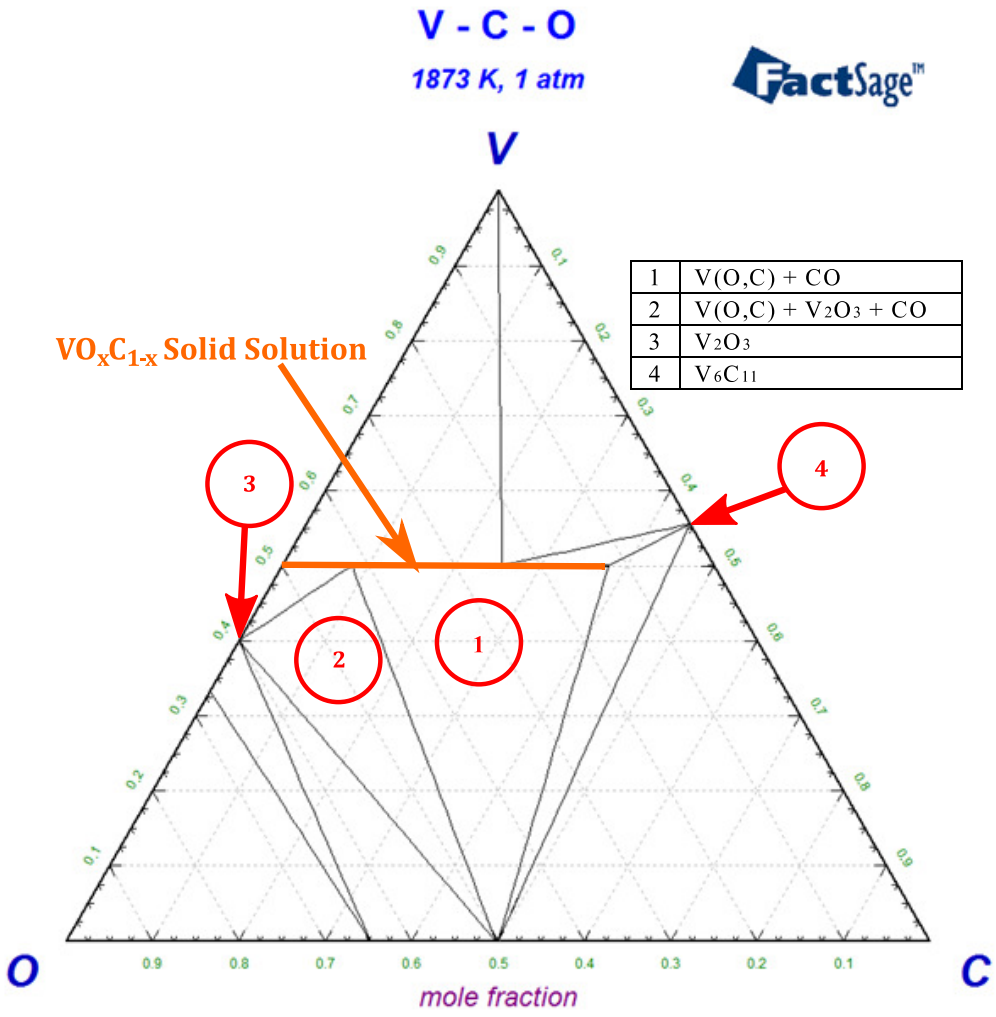

Figure 7.22: Phase diagram of the V-O-C system at 1600 °C (Calculated with FactSage).

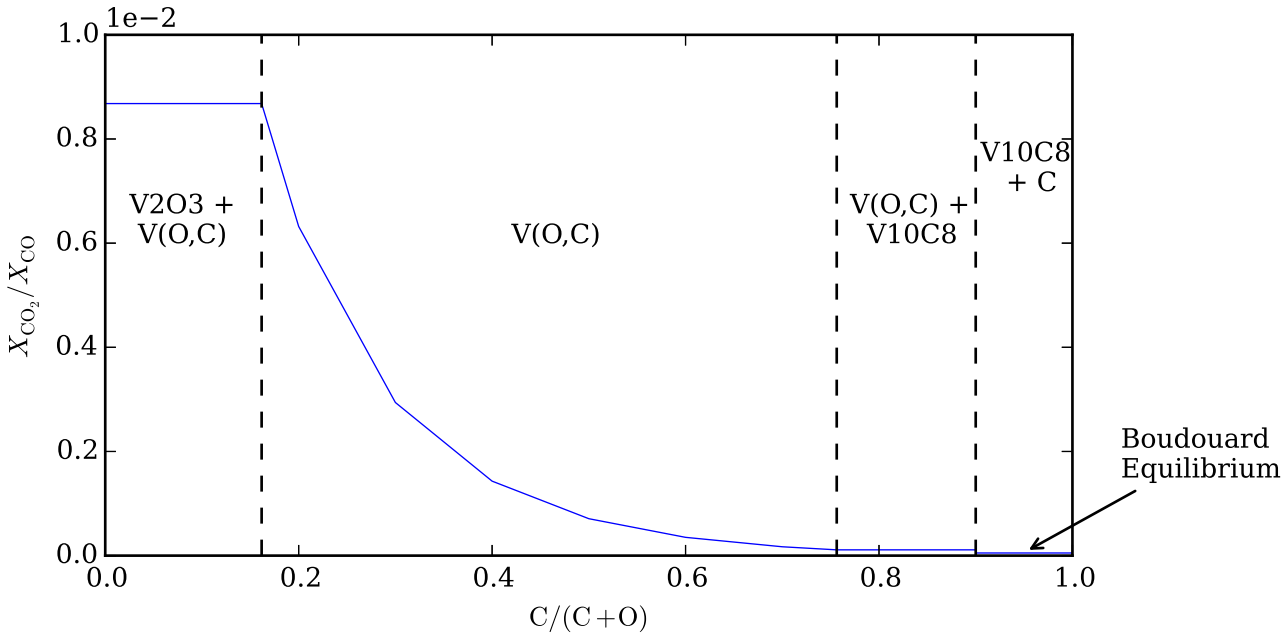

Figure 7.23: Effect of reaction extent on equilibrium CO_2 molar ratio in vanadium oxycarbide at T = 1600 °C, P = 1 atm (Calculated with FactSage using database developed in this work). The x-axis is the molar ratio C to (C + O) in the solid; zero corresponds to V_2O_3 and 1 to VC

The main challenge for the synthesis of vanadium oxycarbide was obtaining a useful precursor. The most common vanadium oxide—vanadium(V) oxide (V_2O_5)—is the only stable oxide under room temperature conditions (lower vanadium oxides tent to oxidize to vanadium(V) oxide over time). However, vanadium(V) oxide melts at 690 °C, making it not ideal for reduction, as a liquid would have a low surface area for reduction, as compared to a finely-powdered solid. Vanadium(III) oxide (V_2O_3) is the next most stable oxide, and remains solid until 1940 °C, making it the better choice for carbothermal reduction at 1600 °C. Vanadium(III) oxide from vanadium(V) oxide was synthesized before performing the vanadium oxycarbide reaction.

As vanadium(V) oxide melts at 690 °C, solid-state reduction is limited to temperatures less than this (600 °C was used in this case). Carbon is not a good reducing agent at these temperatures. Instead hydrogen gas was selected as the reducing agent. The reduction of

vanadium(V) oxide with hydrogen is described by Reaction 7.1.

$$V_2O_5 + 2\,H_2 \longrightarrow V_2O_3 + 2\,H_2O \qquad (K = 3 \times 10^6 \text{ at } 600\,^\circ\text{C}) \qquad (7.1)$$

Synthesis of vanadium(III) oxide began by grinding vanadium(V) oxide powder by hand using a mortar and pestle until fine. 2.5 grams of vanadium(V) oxide was then put into a graphite crucible and put into a quartz glass reactor. This reactor was sealed and placed into a vertical tube furnace. Argon gas was flowed into the reactor vessel while the temperature was taken to 600 °C (pausing when necessary to ensure that the temperature did not overshoot the target temperature). When the temperature reached 600 °C and had stabilized, hydrogen gas was added to produce a 90% Ar-10% H_2 mixture. A dew point analyzer was used to determine when the reaction had reached completion (20-60 minutes depending on the amount of vanadium(V) oxide used). At this point the hydrogen flow was stopped and the reactor cooled down to room temperature under flowing argon.

The resulting vanadium(III) oxide was removed from the reactor and weighed, and then put into a vial for storage. Determining whether the reaction had completed could be done in three different ways—mass loss, color, and XRD. Mass loss can be used by using a mass balance based on Reaction 7.1 to determine the theoretical product mass from a given amount of reactant. Color could be used as vanadium oxides have very distinct colors—vanadium(V) oxide is yellow, vanadium(IV) oxide is blue/violet, and vanadium(III) oxide is black. XRD is the surest method, which shows that the resulting powder is almost entirely vanadium(III) oxide, as in Figure 7.24.

For the reaction for vanadium oxycarbide synthesis itself—described in Reaction 7.2—a 10% over stoichiometric amount of carbon black was mixed with vanadium(III) oxide and reacted under standard titanium oxycarbide furnace conditions (2 hours at 1600 °C, with a ramping

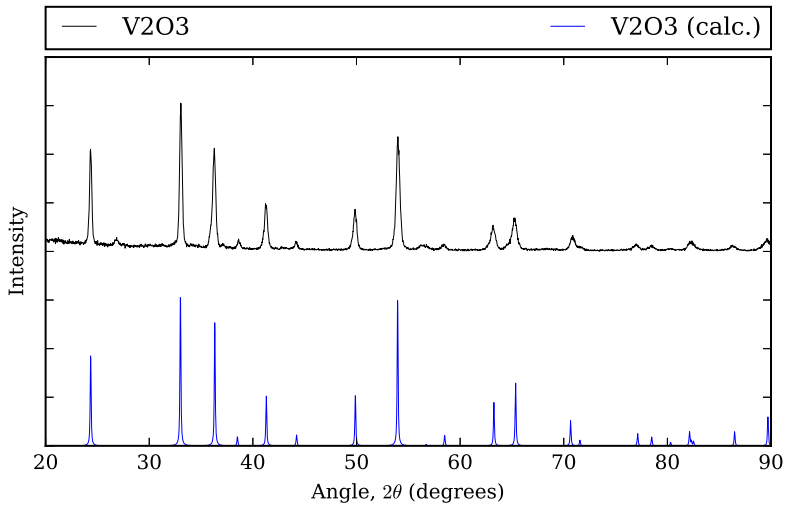

Figure 7.24: XRD Pattern of synthesized vanadium(III) oxide (hydrogen reduced at 600 °C) compared to pure compounds.

rate of 5 °C per minute), mirroring the pigment titanium oxycarbide reaction.

$$V_2O_3 + 3\,C \longrightarrow V_2OC + 2\,CO \tag{7.2}$$

X-ray diffraction of the resulting material (Figure 7.25) shows that the product has peaks between that of vanadium(II) oxide and vanadium carbide, indicating it is a solid solution of the two (and therefore is vanadium oxycarbide). One large peak around 41°appears to be a V_2O_3 peak with an anomalously high intensity—the reason for this is unknown.

7.8 Carbothermal Reduction Kinetics

The initial assumption in designing oxycarbide reduction experiments was that the kinetics of titanium oxycarbide reduction was pore diffusion limited with the rate controlled by diffusion of CO and CO_2 through the porous oxycarbide product layer. This would mean that reduction kinetics should follow the shrinking core model, which means that the a given temperature, reaction time will scale as the square of particle size, and the reductant has no

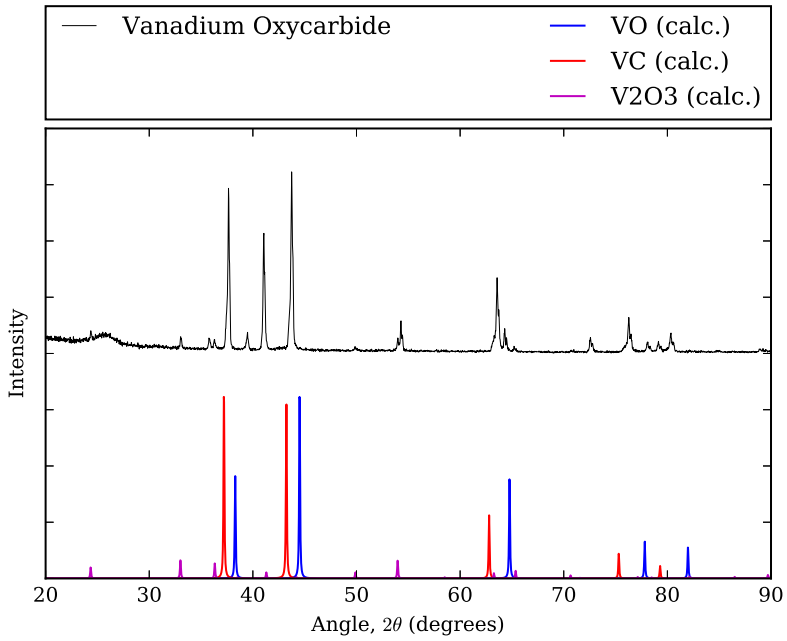

Figure 7.25: XRD Pattern of synthesized vanadium oxycarbide compared to pure compounds.

effect. As noted earlier, finer grinding of the titanium minerals before reduction did improve reduction, confirming at least partial control by pore diffusion. To test whether reductant affects reduction kinetics, we studied the reduction kinetics of titanium oxycarbide with varying particle size and carbon reductant.

The titanium mineral tested (leucoxene) was ground and separated into three different particle size ranges: smaller than 45 μm, between 45 and 75 μm, and larger than 75 μm—but only $<$ 45 μm and 45-75 μm were used in the kinetics experiments. The mean particle size of the $<$ 45 μm fraction was determined by SEM to be 3 μm and the mean size of the 45-75 μm particles was taken to be 60 μm. The three reductants we tested were carbon black, graphite flakes (approximately 1 mm in diameter), and coal tar roofing pitch (Koppers, obtained from Alcoa). A mass balance was used to determine the correct amount of carbon needed for leucoxene reduction. To determine how much carbon remains from the pitch after carbonizing, 10.1 grams of pitch was placed into a crucible and taken to 800 °C and pyrolyzed under an inert argon atmosphere for 2 hours. After cooling, the pyrolyzed

carbon was weighed (4.6 grams remained) and this was used to determine the amount of pitch needed for reduction. This amount of pitch was mixed with the ground leucoxene and heated in an oven to 180 °C and mixed until leucoxene was thorougly mixed and coated with pitch (the softening temperature of the pitch was determined to be between 120 and 140 °C, but 180 °C was used due to the low viscosity of this pitch at this temperature).

The reduction of the leucoxene to titanium oxycarbide was carried out under normal conditions (2 hours at 1600 °C, with a ramping rate of 5 °C per minute). The exhaust was measured using an infrared gas analyzer measuring the CO, CO_2, CH_4, H_2, and O_2 content of the exhaust gas. This data was saved on a computer for later analysis. All samples were weighed after reduction and subjected to x-ray diffraction.

The extent of reaction could be determined by three methods. The first, and likely most accurate, is by mass loss. The second method is by analysis of the x-ray diffraction pattern (this was done using the S-Quant feature of the QualX software package [40]). The final method is by off-gas analysis. As the main product of the reaction is carbon monoxide, the CO content was integrated to determine the total volume (and therefore moles) of CO generated, and this was used to calculate an extent of reaction. However, analysis showed that the mass loss calculated by the off-gas analysis was consistently underestimating the real mass loss by 40-50%. Assuming the error in the gas analyzer measurements is linear, we used the real mass loss data to calculate a correction factor for each experiment.

The basis of the calculation is shrinking core kinetics [32]. In this kinetic model, the product is more porous than the starting reactant. The reductant is a gas—in this case, carbon monoxide (CO)—which has to diffuse through the porous product layer to the reaction front within the particle, where it can then participate in the reaction described by Reaction 3.5 (TiO_2 reduction to Ti_2O_3 proceeds so quickly that it is neglected in this analysis), forming CO_2. This CO_2 then needs to diffuse out of the particle, where it can encounter a source of solid carbon, where by the Boudouard reaction (Reaction 3.3), it is converted into two CO

molecules. Thus, the CO off-gas can be used as a measure of the overall rate of reaction.

$$Ti_2O_3 + 4\,CO \longrightarrow Ti_2OC + 3\,CO_2 \qquad \text{(3.5 revisited)}$$

$$C + CO_2 \longrightarrow 2\,CO \qquad \text{(3.3 revisited)}$$

The equation that governs the rate of oxygen removal from the ore ($\frac{dn_O}{dt}$ or $\dot{n}_O$) is directly related to the rate of CO_2 generation ($\frac{dn_{CO_2}}{dt}$ or $\dot{n}_{CO_2} = \frac{3}{2}\dot{n}_O$). It is assumed that local equilibrium holds at the Ti_2O_3-Ti_2OC gas interface (3.5). The CO_2 generation rate then depends on the effective diffusion coefficient of the gas (D_{eff}, which is determined from the pore diffusivity D_{pore} and Knudsen diffusion coefficient D_K), concentration difference (ΔC), particle size (r_o), size of the unreacted core (r_i), molar density of Ti_2O_3 the reactant (ρ_n), and the number of moles of gas generated (Z) per mole of reactant. This equation is given in Equation 7.1 below. How each of these variables is calculated is discussed in Appendix B.

$$\dot{n}_{CO_2} = D_{\text{eff}}\Delta C\frac{4\pi r_o r_i}{r_o - r_i} = -4\pi r_i^2 \rho_n Z\frac{dr_i}{dt} \qquad (7.1)$$

Integration leads to Equation 7.2:

$$\frac{1}{6}r_o^2 + \frac{1}{3r_o}r_i^3 - \frac{1}{2}r_i^2 = \frac{D_{\text{eff}}\Delta C}{Z\rho_n}t \qquad (7.2)$$

Using Equation 7.1, an expected curve of normalized rate ($\frac{\dot{n}_O}{N_O^{Tot}}$) versus extent of reaction (f) was calculated. N_O^{Tot} is the number of moles of atomic oxygen (present as Ti_2O_3) in the unreacted core, and f is the extent of reaction; $f = 1 - \left(\frac{r^i}{r^o}\right)^3$. This is shown in Figure 7.26 along with the actual rates taken from the IR spectrometer. The concentration difference (ΔC) was taken from Figure 3.3.

It is immediately evident that the actual rates of reaction are orders of magnitude slower than

the theoretical rate. Of all the parameters in the equation the one expected to deviate most from the theoretical values under real experimental conditions is the value of concentration difference (ΔC). As explained in more detail in Appendix B, the theoretical value is derived from the difference between the equilibrium CO_2 concentration at the reaction front between Ti_2O_3 and Ti_2OC, and the Boudouard equilibrium concentration. However, the Boudouard equilibrium condition implies a "perfect" reductant. Also, under pore diffusion control there should be no effect of reductant (only particle size), but Figure 7.26 clearly shows that there is a significant effect of the reductant used. Pitch gives the highest reduction rate.

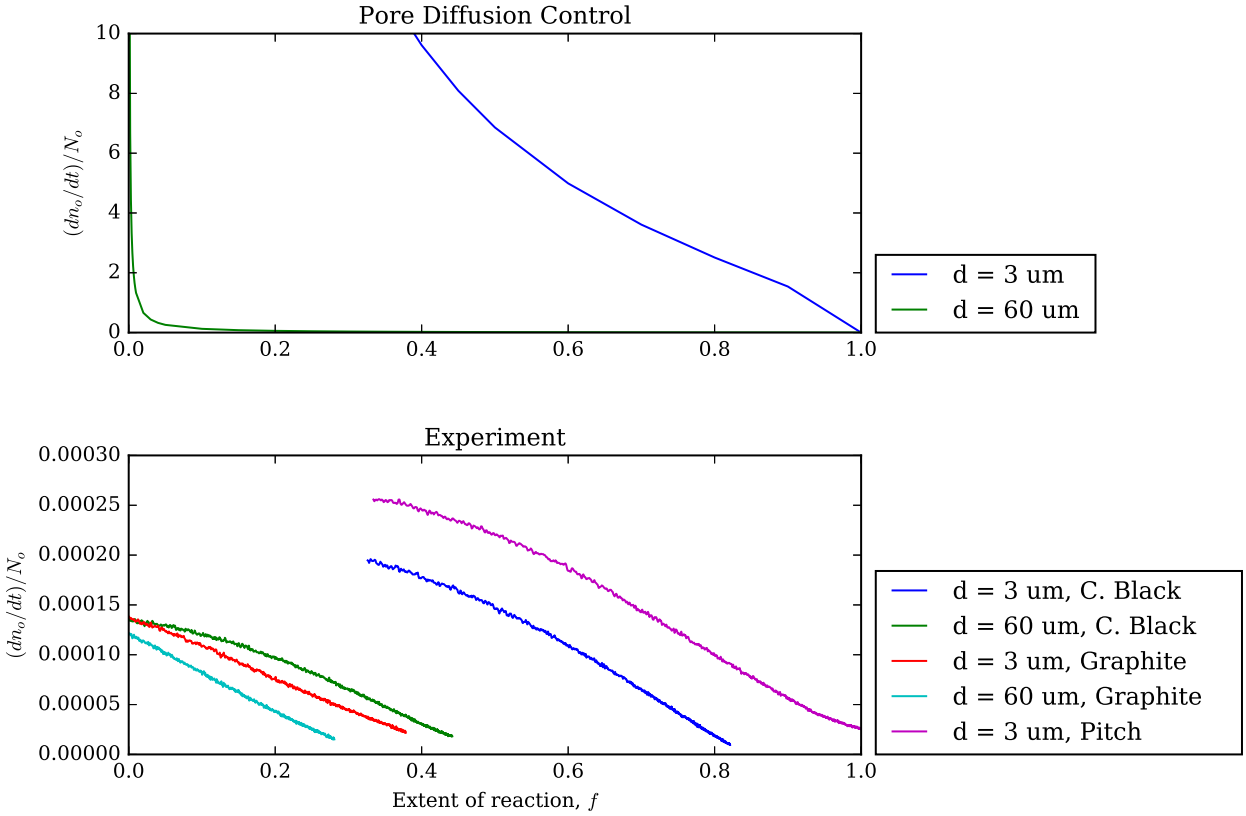

Figure 7.26: Plot of oxygen removal rate (s^{-1}) versus extent of reaction for pore diffusion control (top) and experimental measurements (bottom).

The fact that there is an effect of reductant and of particle size demonstrates that the reaction is governed by mixed control, not just pore diffusion control. Especially for larger reductant particles—such as the graphite reductant, which had flakes approximately 1 mm

in diameter—pore diffusion within the reductant would also have an effect on that reaction [57, 58].

The effect of the mixed control can be quantified with the ΔC variable. While the assumption of Boudouard equilibrium implies a constant value for ΔC, mixed control implies a varying ΔC that is smaller than the equilibrium value. Figure 7.27 and 7.28 show the calculated values of ΔC for each case.

While Figure 7.27 shows that the value of ΔC is not a constant, a very rough approximation of ΔC for a given set of conditions (particle size and reductant used) can be obtained from the average value of ΔC for that data set. The calculated values are shown in Table 7.2. This value can then be used to determine a hypothetical time for full reaction using Equation 7.2. This information is summarized in Table 7.3.

The information gathered in these experiments shows that the best reductant by far is pitch(as seen in Table 7.3). IR information was not obtained for a test with pitch and 45-75 μm particles but the XRD patterns—shown in Figure 7.29—and mass loss data shows that the larger particles were also fully reduced within approximately 2 hours. Pitch also had the added benefit of producing a sintered oxycarbide "pellet", though the reason for this is unknown. The main drawback with using pitch in our experiments was the large amount of sulfur deposition and sulfur containing gases generated in the furnace. However, these problems could be mitigated with basic cleaning and maintenance of the furnace chamber and exhaust tube, and could potentially be avoided if a lower sulfur pitch is used.

Table 7.2: Average value of ΔC (in mol/cm^3) for varying particle size and reductant combinations.

	3 μm particles	60 μm particles
Carbon Black	2.61×10^{-14}	3.10×10^{-16}
Graphite	4.97×10^{-15}	1.37×10^{-16}
Pitch	7.47×10^{-14}	—

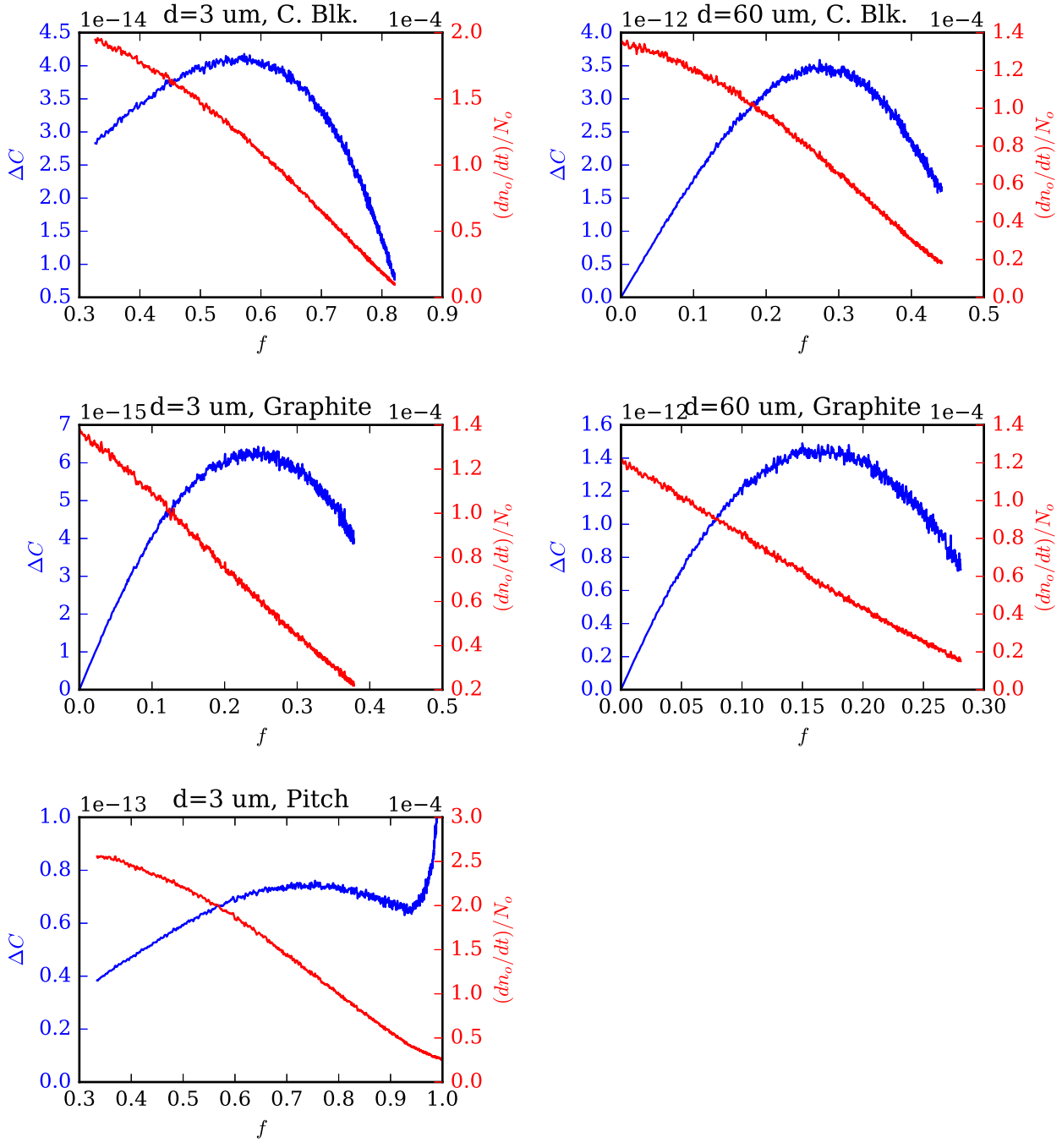

Figure 7.27: Plot of ΔC (in mol/cm^3) and oxygen removal rate (s^{-1}) for varying particle size and reductant combinations.

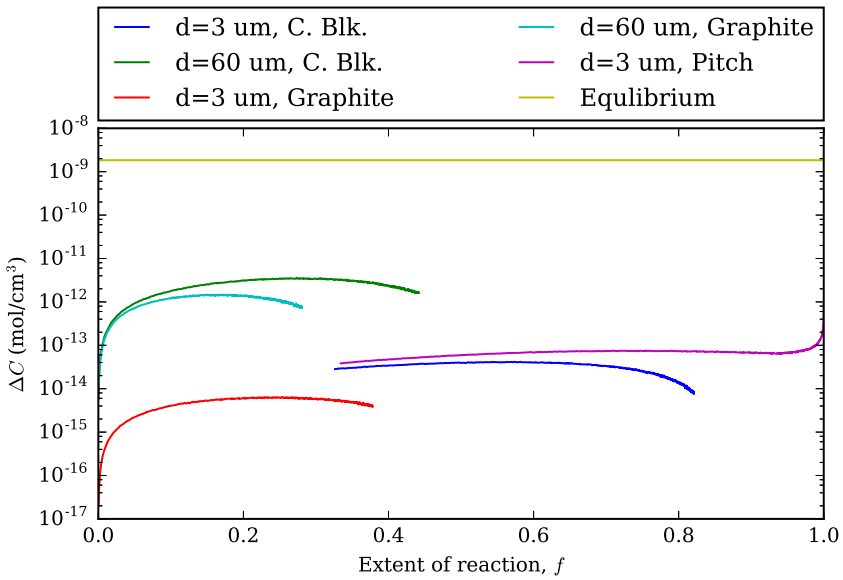

Figure 7.28: Plot of ΔC (log scale) all experimental cases and equilibrium.

Table 7.3: Estimated time (in hours) for full reaction at 1600 °C for different cases of particle size and reductant, using average values for ΔC.

	3 µm particles	60 µm particles
Carbon Black	5.5	23.2
Graphite	28.9	52.4
Pitch	1.9	—

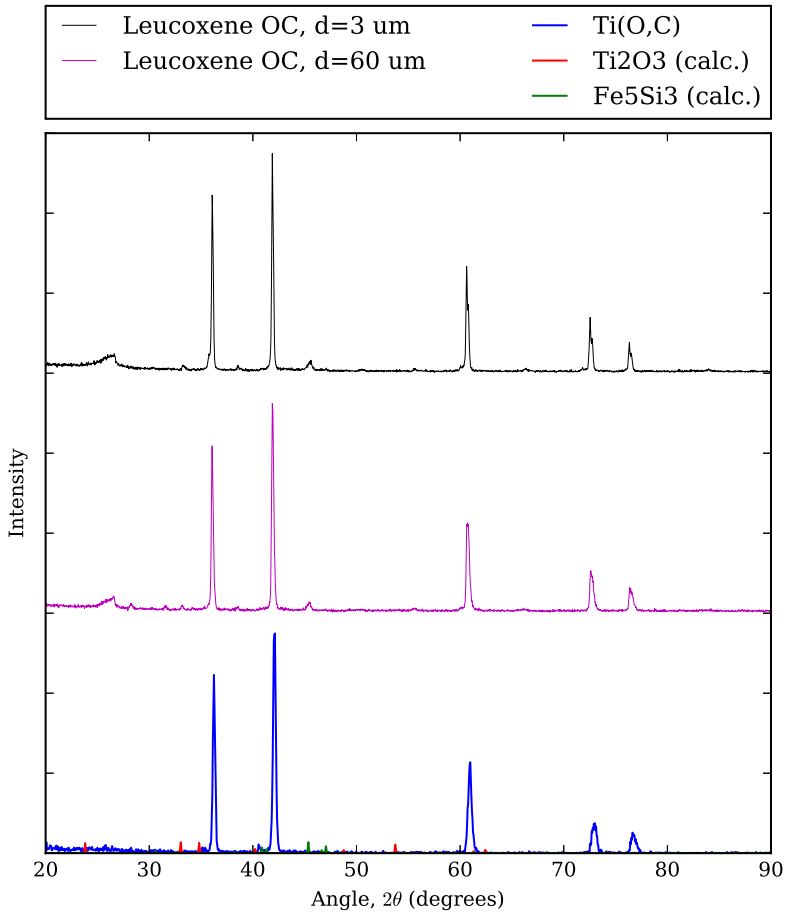

Figure 7.29: XRD Pattern of 3 µm and 60 µm leucoxene powders reduced by pitch to oxycarbide. Compared to pure compounds.

Chapter 8

Purification by Leaching

To be able to use titanium oxycarbide materials made from lower-grade materials for titanium production, most of the metallic impurities (especially iron) must be removed. There are two different paths to take to do this: one is to remove the iron from the ore before carbothermal reduction to make titanium oxycarbide (analogous to an "upgrading" process to turn the low grade ore into a higher grade material), or removal of metallic iron from a partially or fully reduced titanium ore. This work tested multiple methods to do this, and these are summarized in Table 8.1 as the amount of iron removed relative to titanium.

In this chapter, we will be discussing methods of removing iron from iron-containing titanium oxycarbide materials, as well as methods of "upgrading" iron-rich titanium ores to synthetic rutile by non-electochemical means.

8.1 Aqueous ("Becher-style") Iron Leaching

In order to upgrade ilmenite to a synthetic rutile, the Becher process [59, 31] is used. The Becher process uses a reduced titanium ore—where only the iron is reduced to metallic form, as in reaction (8.1)—which is then leached in an oxygenated 0.1M ammonium chloride

Table 8.1: Summary of different iron removal methods from ores and oxycarbides.

Method	Ores tested	Notes
Becher	Pseudorutile oxycarbide	Removes iron, but reoxidizes oxycarbide.
Molten salt leaching	Pseudorutile ore Ilmenite ore (SA) Titaniferous slag (SA)	Removes iron, but only in pseudorutile. Slow.
Electrochemical upgrading of ore	Pseudorutile ore	Removes iron, but only in oxidized ores. Slow.
Electrochemical iron removal from oxycarbide	Rutile oxycarbide Leucoxene oxycarbide Pseudorutile oxycarbide Ilmenite oxycarbides	Removes iron, but limited by Fe_5Si_3 formation

(NH_4Cl) solution. This solution reacts with the iron, dissolving it as in reaction (8.2). This iron-containing solution then reacts further with the oxygen and water to make insoluble iron oxides and hydroxides, as in reaction (8.3). This insoluble iron is then removed, leaving behind a porous synthetic rutile.

$$\mathrm{FeTiO_3 + C \longrightarrow TiO_2 + Fe + CO} \qquad (\mathrm{T = 1200\,^{\circ}C}) \tag{8.1}$$

$$\mathrm{Fe + \frac{1}{2}\,O_2 + 2\,H^+ \longrightarrow Fe^{2+} + H_2O} \tag{8.2}$$

$$\mathrm{Fe^{2+} + \frac{1}{4}\,O_2 + \frac{3}{2}\,H_2O \longrightarrow FeO(OH) + 2\,H^+} \tag{8.3}$$

Since this process is used for industrial scale removal of metallic iron from titanium ores, it would be a possible method in order to remove iron from titanium oxycarbide, such as an oxycarbide made from a pseudorutile mineral sand. The results of such an attempt from a pseudorutile oxycarbide (washed at 40 °C in a magnetically stirred beaker overnight) is

shown in Figure 8.1. This XRD pattern shows that while much of the iron content was leached, the leaching also increased the amount of Ti_2O_3 present.

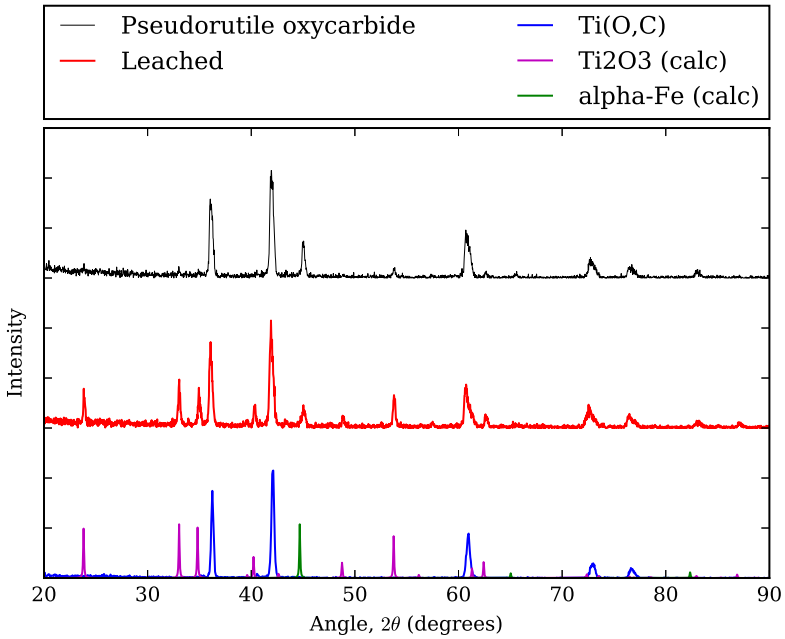

Figure 8.1: XRD Pattern of pseudorutile oxycarbide before and after Becher leaching.

The reason for this partial oxidation of the oxycarbide is probably the mildly oxidizing environment of the leach—which takes place in oxygenated water. The oxidation mechanism is not clearly known, but it appears that Ti_2O_3 must be present before leaching for Ti_2O_3 to increase during leaching. When visiting researcher Jie Dang created pure fully reduced titanium oxycarbide (from natural rutile using methane reduction) with no Ti_2O_3, Becher leaching had no effect on the oxycarbide itself.

However, it is expected that carbothermal reduction with solid carbon will always contain trace levels of Ti_2O_3. Therefore, Becher-style leaching is not advisable, as it decreases our titanium oxycarbide yield, and increases anode sludge, as Ti_2O_3 is inert in our electrochemical cell. Becher leaching was also found to be ineffective at removing silicon-containing iron, which is commonly produced by carbothermal reduction.

8.2 Molten Salt Leaching

Given to the difficulty in removing iron from titanium oxycarbide, it would make sense to remove the iron prior to titanium oxycarbide production. However, there would be no economic advantage to doing so by conventional means, as processes to make synthetic rutile exist (there is no obvious advantage to producing synthetic rutile it is already a well-established product). Therefore the focus of the rest of this chapter is on novel methods of iron removal from titanium ores, especially molten salt leaching methods, which can use a reactor similar to the one already used for the MER process.

In the 1970s Pollard and Stewart described a method for molten salt leaching of iron from ilmenites [61, 62, 63]. Their process involves putting an ilmenite mineral sand into sodium chloride with ground coke. Then the sample is heated to around 1000 °C under an atmosphere of nitrogen, carbon monoxide, and hydrogen chloride gas. Alternatively, instead of hydrogen chloride gas, the patent describes the use of a hydrogen chloride generator, namely adding hydrated ferrous chloride ($FeCl_2 \cdot 4H_2O$) to produce hydrogen chloride in-situ. After cooling back to room temperature, the sample is washed and subjected to magnetic separation. The non-magnetic fraction is essentially synthetic rutile.

Pollard and Stewart argued that the hydrogen chloride and carbon monoxide were responsible for the dissolution and reduction of the iron oxide from the titanium ore. However, when the experiment was repeated in this work (placing 1 gram of NaCl, 1 gram of titanium ore, and 0.3 grams of carbon in a crucible and holding at 900 °C for 4 hours) without carbon monoxide and no source of hydrogen chloride, the leaching still occurred, albeit only when pseudorutile mineral sand was used as a feedstock (there was no leaching observed in the ferrous titanium ores, namely actual ilmenites and titaniferous slags). It is proposed that the basis for iron removal by this method is due to the small—but nonzero—solubility of

The content of this section has also been described in my paper: "Upgrading of Iron-Rich Titanium Minerals Using a Molten Salt Process" [60].

iron(III) oxide in alkali chloride salts [64].

The ability for iron(III) oxide to dissolve in molten alkali chlorides was tested by putting a small amount of pseudorutile mineral sand (50 mg) in 100 grams of alkali chloride salt (NaCl, KCl, or NaCl-KCl eutectic) in an alumina crucible. The mixture was then put into a furnace for varying amounts of time (1-24 hours) under a nitrogen atmosphere. After cooling to room temperature, the salt was washed overnight with clean water in a Soxhlet extractor. After washing the pseudorutile was dried and mounted in resin for SEM. In the SEM, various backscatter images were taken of the partially-leached pseudorutile particles 8.2. The leached areas were estimated by image analysis using ImageJ [42], and from this data approximate dissolved concentrations can be determined, shown in Table 8.2.

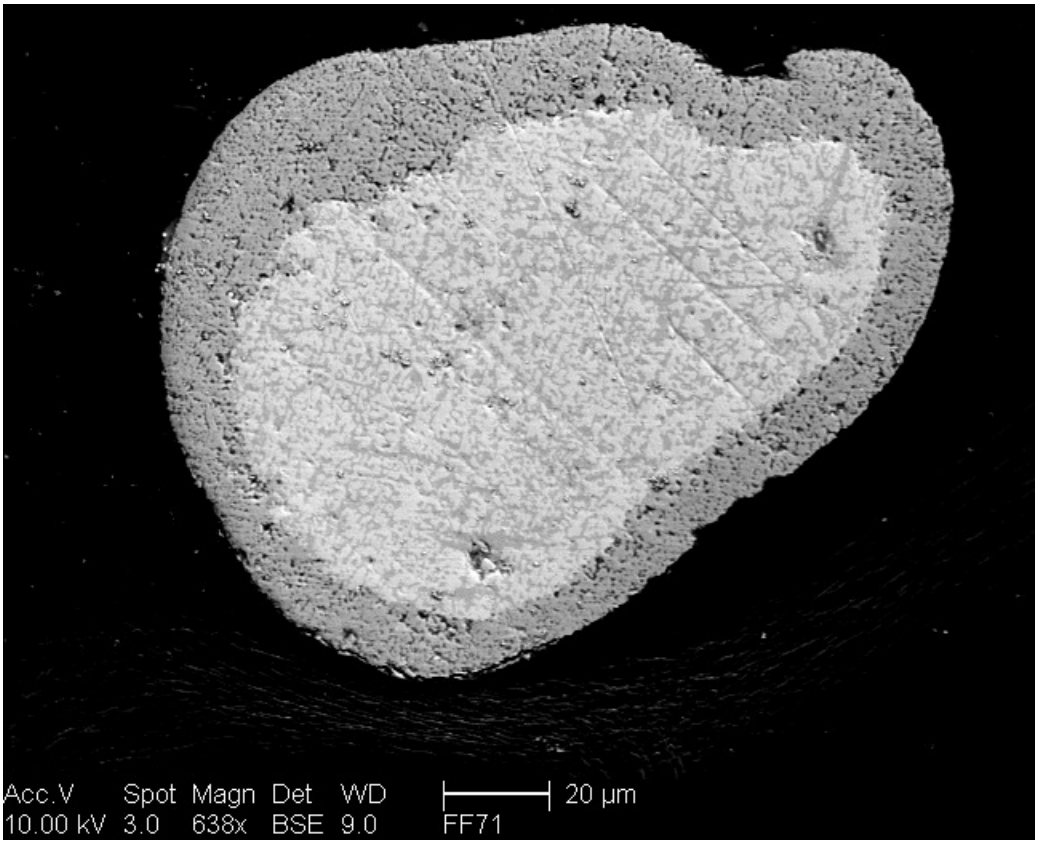

Figure 8.2: Backscattered SEM image of a pseudorutile particle after 4 hours of Fe_2O_3 dissolution in NaCl molten salt. Darker outer shell contains no iron.

The mechanism for this process is contingent upon the solubility of iron(III) oxide. When

Table 8.2: Concentration of iron(III) oxide in molten alkali chlorides at 900 °C after different leaching times.

Salt	Time (hours)	Concentration (ppm molar)
NaCl	1	17
NaCl	4	27
KCl	4	26
NaCl-KCl (eutectic)	24	43

the mineral sand is put in contact with molten alkali chloride salt, the iron(III) oxide will dissolve. It will remain in solution in the salt until presented with a reductant, in this case solid carbon (the patent called for ground coke—carbon black was used in this work). The dissolved iron is reduced to metallic iron by the reductant, away from the titanium oxide particle, allowing for easy magnetic separation as the leached titanium dioxide is physically separate from any formed metallic iron.

Attempts at using other molten salts with potentially higher solubilities for oxides, such as calcium chloride were not very successful. Using calcium chloride as the molten salt resulted in the all the leached areas of the material being converted into perovskite ($CaTiO_3$). The likely reason for this that calcium chloride is a deliquescent salt, and is very hygroscopic and thus would contain some CaO after heating and melting. In fact, XRD of the salt itself showed that it was a mixture of hydrated calcium chlorides—$CaCl_2{\cdot}2(H_2O)$ and $CaCl_2{\cdot}6(H_2O)$. During the process of heating up the salt, this decomposes into $CaCl_2$, CaO, and HCl. Free CaO can react with TiO_2 and produce perovskite. Thus in order to use calcium chloride, care would have to be taken to make sure it is fully anhydrous, which does not appear to be practically feasible.

Other attempts were made to perform the same leaching on oxidized ilmenite. Since ilmenite normally contains its iron in the form of iron(II) oxide, South African ilmenite mineral sand was first oxidized in a box furnace at 800 °C overnight in air before leaching. XRD (shown in Figure 8.3) shows that the material was converted by oxidation to a combination of rutile, pseudobrookite (Fe_2TiO_5 or $Fe_2O_3{\cdot}TiO_2$), and hematite (Fe_2O_3), which indicates all of the

iron has been oxidized to the form of iron(III) oxide.

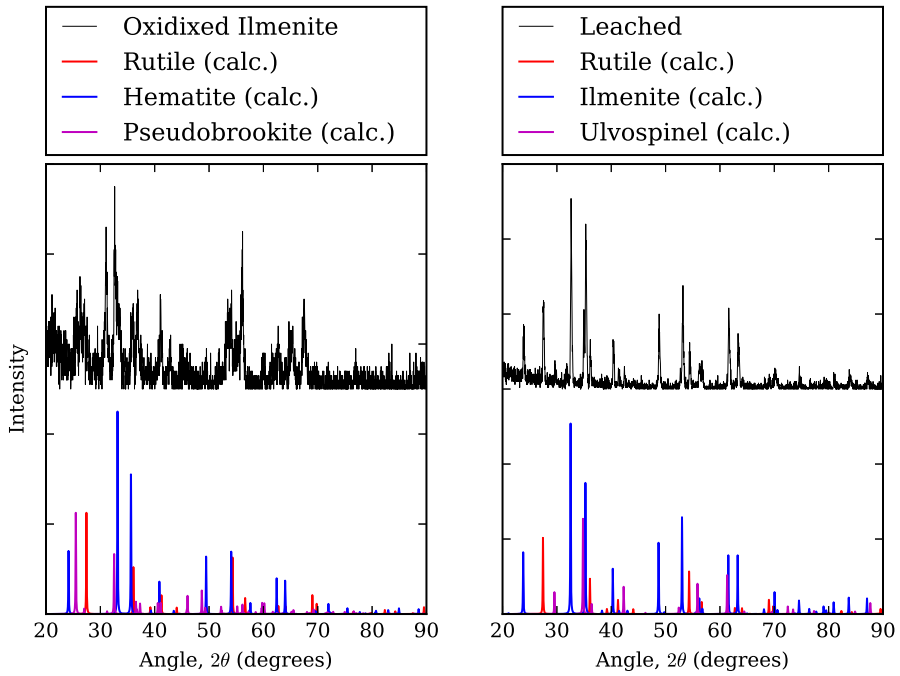

Figure 8.3: XRD Patterns of oxidized South African Ilmenite (left) and result after molten salt leach (right).

The oxidized ilmenite mineral sand was ground and subjected to the same treatment as pseudorutile. However, the result was very different than expected. Rather than just leaching the iron, the mineral sand itself was altered by the process. XRD shows the resulting material is a combination of rutile, ilmenite, and ulvöspinel (Fe_2TiO_4 or or $2(FeO)\cdot TiO_2$). While it appears that no iron(III) oxide remained, the oxidized mineral sand was apparently re-reduced to an iron(II) oxide in the presence of carbon.

Chapter 9

Electrochemical Purification

This chapter will discuss the possible electrochemical routes to purifying titanium concentrates or oxycarbides.

9.1 Electrochemical Leaching of Iron from Oxidized Pseudorutile

Since the mechanism discussed in Section 8.2 involves the dissolution of an iron species, an alternative to using carbon as reductant is electrochemical plating. Therefore, using an iron-containing working electrode and a graphite (for example) counter electrode, the trivalent iron can be plated from the salt, keeping the concentration in solution low without the need for a source of carbon in the melt itself.

It should be stated that DuPont had a patent [66] on a similar process (also seemingly derived from the works of Pollard and Stewart). However, this patent still relies on a reducing atmosphere containing carbon monoxide, whereas as mentioned in Section 8.2, the current

The content of this section has also been described in my paper: "Electrochemical Upgrading of Iron-rich Titanium Ores" [65].

work showed that a reducing atmosphere is not necessary. Also, the iron oxide in the titanium concentrates were specified as ferrous, or iron(II) oxide, whereas in this work it was found that the solubility of iron(II) oxide is significantly lower than that of iron(III) oxide.

In this work, the pseudorutile was first oxidized in order to fully convert the iron oxide to ferric oxide the purpose of oxidation was to remove the trace amounts of ilmenite present in the pseudorutile sand. One gram ore ore was placed in a small alumina crucible and oxidized in a box furnace in air at 1000 °C for 24 hours. The result was that the mineral sand was converted to rutile and fully-oxidized pseudobrookite (Fe_2TiO_5 or $Fe_2O_3{\cdot}TiO_2$) as seen by the XRD pattern in Figure 9.1.

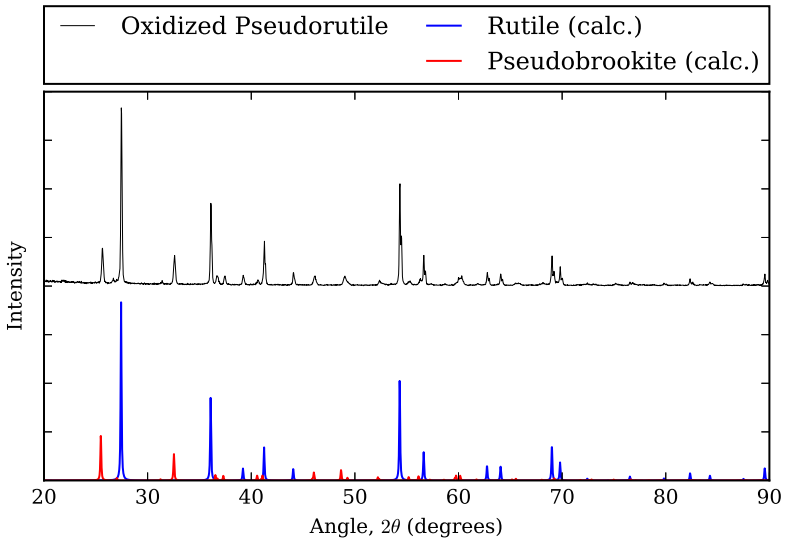

Figure 9.1: XRD Pattern of Florida pseudorutile oxidized at 1000 °C.

The oxidized pseudorutile mineral sand was placed in a graphite anode basket which also acted as the counter electrode (a basket was used to simplify the removal of the pseudorutile upon completion of the experiment). Stainless steel was used as the working electrode and a potential of -0.5 volts was applied in a potentiostatic regime for 8 hours. Under these conditions, iron would chemically dissolve in the electrode and be plated out at the cathode. The expected anodic reaction is production of CO or CO_2. The experiment was paused every 4 hours to recycle and regenerate the reference electrode to prevent potential drift.

XRF results showed that the iron content had been decreased from 17.5 wt% to 6.6 wt%, as shown in Table 9.1. X-ray diffraction also shows the ore as being simply a rutile, as seen in Figure 9.3. Its color is also yellowish as opposed to gray (Figure 9.2), indicating that it is now a leucoxene, not a psuedorutile. Given all of these observations, the process clearly is capable of making at least leucoxene from pseudorutile mineral sand.

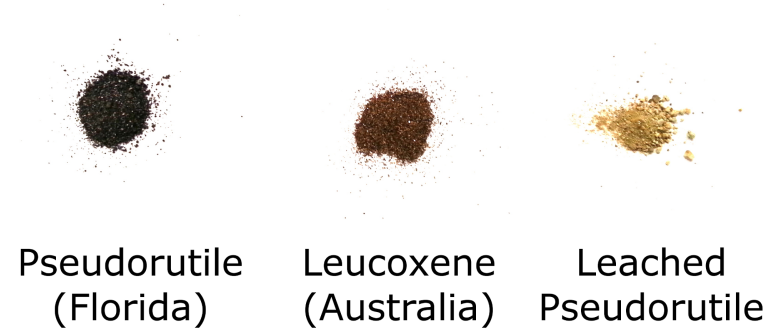

Figure 9.2: Leached pseudorutile compared to Pseudorutile and Leucoxene

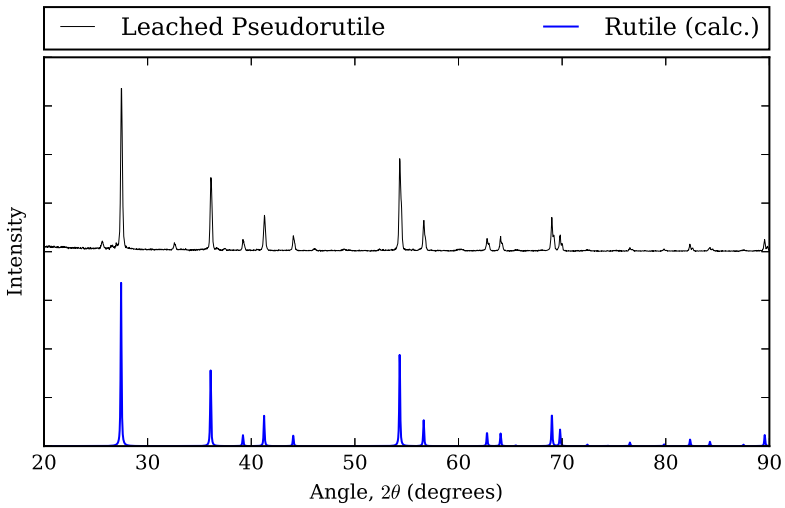

Figure 9.3: XRD Pattern of Florida pseudorutile after 8 hour electrochemical leach.

This method of electrochemical leaching could be improved in multiple ways. One would be to introduce mechanical mixing to the system, as inadvertent jolts to the electrodes previously showed momentary increases in current due to incidental mixing due to the motion

Table 9.1: Composition (in mass percent) of electrochemically leached pseudorutile compared to original concentrate.

Material	Pseudorutile	Leached
TiO_2	77.5	89.1
Fe_2O_3	17.51	6.63
Al_2O_3	0.27	0.30
CaO	0.18	—
Cr_2O_3	0.40	0.15
MgO	0.04	0.02
MnO	0.93	0.04
SiO_2	1.64	1.92
V_2O_5	1.37	1.37
ZrO_2	0.11	0.21

of the electrodes in the electrolyte. Mixing is expected to aid iron removal because of low solubility of iron oxide would lead to mass transfer control of the rate of transfer of iron oxide from the mineral particles through the salt to the cathode. Another is to use a different electrolyte that has a higher solubilities for oxides, such as calcium chloride. However as seen in Section 8.2, care must be taken for calcium chloride to be anhydrous, as the presence of calcium oxide will promote the formation of perovskite ($CaTiO_3$). Alternatively, longer leaching times would be required to remove more iron, as the reaction was not complete after the 8 hour procedure. However, doing so may not be practical for industrial purposes.

If the reference electrode is not regenerated every few hours or so, the result is that the silver chloride will slowly diffuse out of the reference electrode tube and be plated out. The result is that the reference electrode potential will drift over time. In one early experiment, the reference was not regenerated and the potential of the cathode drifted, likely to the point of electrolyte decomposition. Analysis of the mineral sand after leaching showed that instead of rutile, there was another compound present (in addition to ilmenite and rutile), as seen in the XRD pattern in Figure 9.4. The new compound was identified as being $K_xTi_8O_{16}$ ($0 < x < 1$). This compound is a rutile-like structure with intercalated potassium atoms [67]. While this is interesting, further investigation was beyond the scope of this project.

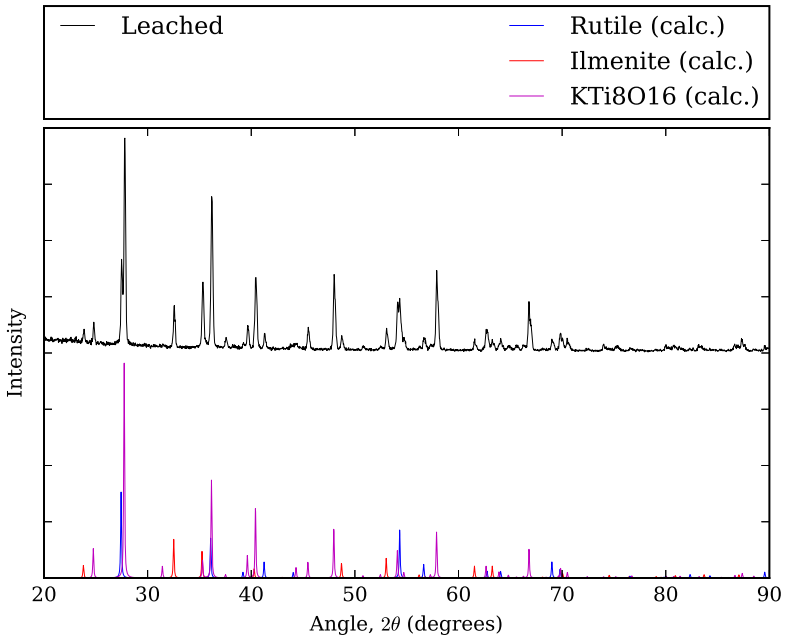

Figure 9.4: XRD Pattern of Florida pseudorutile after electrolyte decomposition showing the presence of $K_xTi_8O_{16}$.

It should also be noted that while iron in this ore is mostly already iron(III) oxide (due to it being a pseudorutile mineral sand), there are detectable levels of ilmenite present. If the experiment is repeated without oxidation of the ore, the ilmenite will remain after the leaching is complete, as shown in the XRD pattern in Figure 9.5, and the SEM and EDS image in Figure 9.6.

9.2 Electrochemical "Upgrading" of Reduced Ilmenite Mineral Sand (South Africa)

Based on the tests performed in this work, the iron content of iron-rich (greater than 20%) mineral sands is too high to be leached in any reasonable time by the oxidized ore leach discussed in Section 9.1. Therefore, a different method was investigated. It was proposed that if an electrically conductive path could be made between metallic iron in a reduced

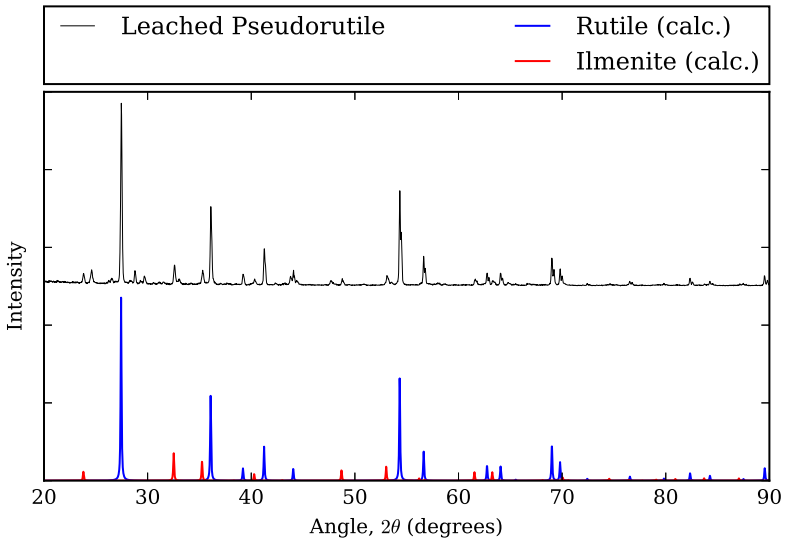

Figure 9.5: XRD Pattern of non-oxidized Florida pseudorutile after 12 hour electrochemical leach showing remaining ilmenite from the original ore.

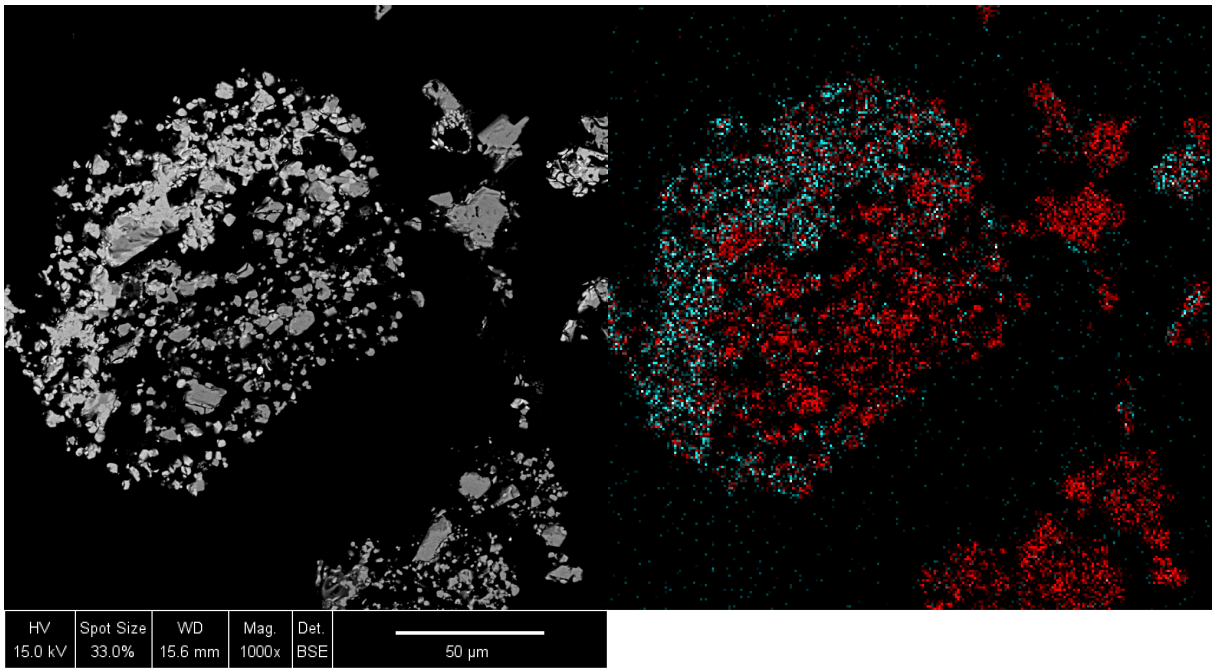

Red = Titanium, Cyan = Iron

Figure 9.6: Backscattered SEM image and EDS map of non-oxidized Florida pseudorutile after 12 hour electrochemical leach.

ilmenite—such as the feed for the Becher process, the result of Reaction (8.1)—then the metallic iron can be leached by electrochemical means.

First, a conductive binder had to be selected. Drawing from the work of Chun and Whitacre [68], a conductive binder was produced from carbonized dextrose. First, dextrose was caramelized at 185 °C for 12 hours in air. The resulting caramel was then ground with a mortar and pestle, and the fraction larger than 400 µm was removed. This caramel was pressed with ilmenite mineral sand (5 grams of caramel per 2 grams of ilmenite) into a 0.75 inch die under 9 metric tons of force for 2 minutes. This pellet was then fired at 1200 °C under argon for 2 hours to both carbonize the caramel to form graphite, and to reduce the iron in the ilmenite to metallic form. The x-ray diffraction pattern of the pellet material (Figure 9.7) shows that the sample has mostly been converted from ilmenite to a rutile and metallic iron. However, the reaction is not complete, and there is still ilmenite present.

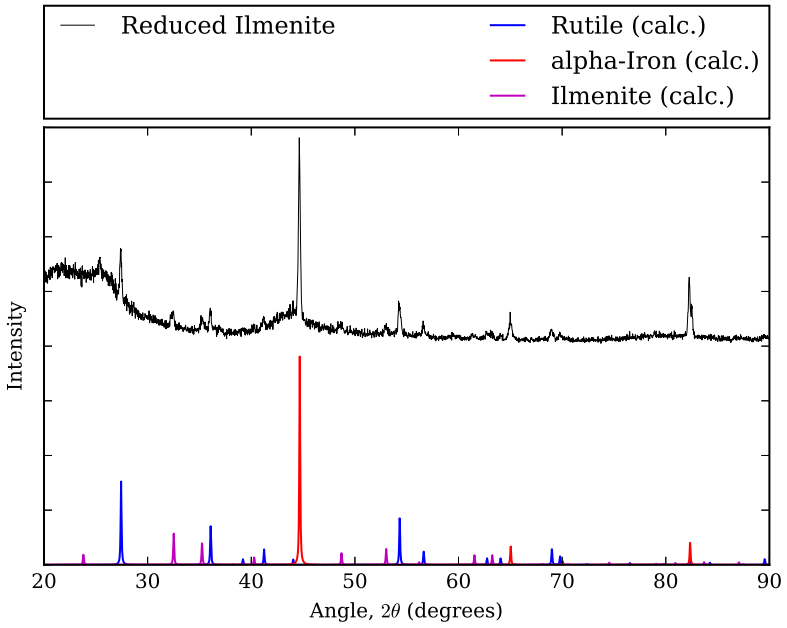

Figure 9.7: XRD Pattern of the reduced ilmenite pellet compared to pure compounds.

After this, the pellet was placed into the graphite anode basket and then put into the electrochemical reactor. The conditions for the reactor were the similar to the conditions

needed for making titanium for titanium oxycarbide. The electrolyte is doped with Fe^{2+} ions to a molar fraction of 8.66×10^{-5} by mixing dry ferrous chloride ($FeCl_2$) with the electrolyte. The anode basket is used as the working electrode, and an iron or stainless steel strip used as a counter electrode. A potential of +0.5 V_{ref} is applied, and the experiment is run for 8 hours (pausing to recycle and regenerate the electrode after 4 hours).

After 8 hours, the basket was removed and its contents washed with distilled water overnight in a Soxhlet extractor to remove salt. After drying, the sample along with the deposit at the cathode were analyzed was analyzed by XRD in Figure 9.8 and XRF in Table 9.2. The XRF results of the leached sample show insufficient iron removal to be used for oxycarbide production. However in addition to iron, manganese and the radioactive elements have been greatly reduced by electrochemical leaching. Likewise, the concentration of manganese and the radioactive elements at the cathode have greatly increased. This implies that at least for this material, the radioactive elements are likely reduced during the carbothermal reduction step, and can be anodically dissolved and subsequently plated out. This would also seem to imply that if an oxycarbide material has reduced radioactive elements, these may also contaminate the titanium as well.

9.3 Electrochemical Impurity Removal from Natural Titanium Oxycarbides

The results of the leaching of the reduced South African ilmenite mineral sand (Section 9.2) demonstrated that in principle, metallic iron and other metallic impurities can be removed, so long as a conductive path to the iron can be established. However, as TiO_2 is a poor electrical conductor, a conductive path of carbon binder needs to be used to make the metallic impurities electrochemically active.

As titanium oxycarbide is an electrical conductor, it could be a suitable conduction path for

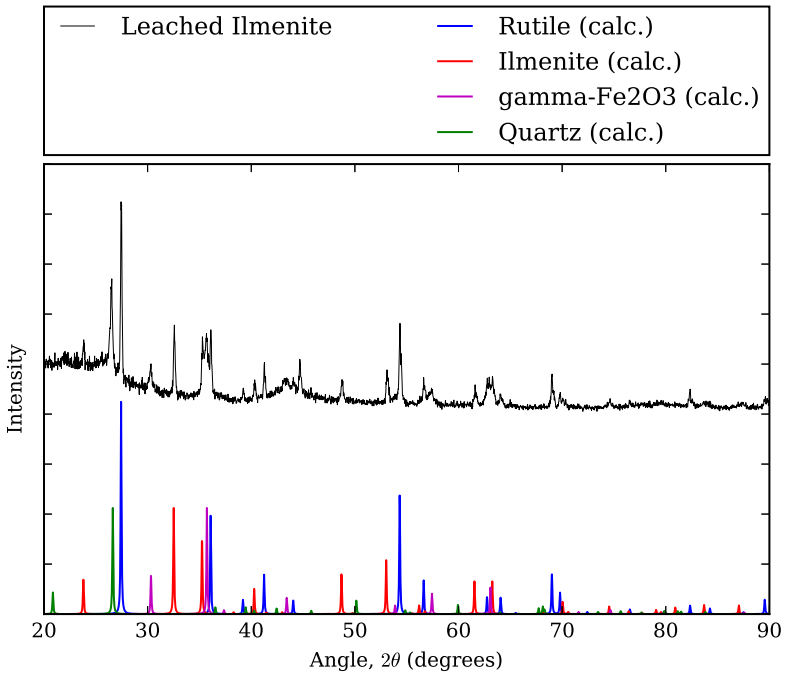

Figure 9.8: XRD Pattern of the leached reduced ilmenite pellet compared to pure compounds showing low iron removal.

Table 9.2: Composition of electrochemically leached Ilmenite (SA) and cathode deposit compared to original concentrate. Products reported as mass percentage of stated oxide.

	Ilmenite (SA)	Leached	Deposit
TiO_2	40.82	52.68	-
FeO	53.66	41.96	99.13
Al_2O_3	0.53	0.33	-
CaO	0.13	0.30	-
Cr_2O_3	0.39	0.86	-
MgO	0.03	0.02	-
MnO	1.27	0.04	0.83
Nb_2O_5	0.09	0.31	-
SiO_2	2.13	1.92	-
V_2O_5	0.89	1.37	-
ZrO_2	0.04	0.21	-
Th+U	63 ppm	23 ppm	485 ppm

removing metallic impurities from titanium oxycarbide. However, doing so would require keeping the dissolution potential below that of titanium oxycarbide (+0.43 V_{ref}). From Table 3.1, this constraint allows for a potential window of approximately 500 millivolts (the difference between the dissolution potentials of iron ($FeCl_2$) and titanium oxycarbide).

The procedure for this process entails carbothermal of the ores (to produce a mixture of titanium oxycarbide and metallic products). This "crude" titanium oxycarbide is then put into a graphite anode basket and put into the electrochemical reactor. An anode potential of +0.2 V_{ref} is applied in a potentiostatic regime, and continues until the current levels out at a low value (<20 milliamperes). The potential of +0.2 V_{ref} is more positive than the iron dissolution potential, but less than for titanium oxycarbide dissolution.

Multiple ores were tested with this regime: natural rutile and leucoxene (Australia), pseudorutile (Florida), and ilmenite (South Africa). All materials were ground for 3 minutes before carbothermal reduction. The "crude" titanium oxycarbide materials were subjected to XRF to determine the relative amounts of titanium and iron, and XRD for phase identification. The same characterization techniques were used on the resulting purified titanium oxycarbides. The XRF results are summarized in Table 9.3.

Secondary electron imaging of crude and purified pseudorutile oxycarbide in the SEM shows that the morphology of the titanium oxycarbide features is unchanged, indicating that it has not been affected by the anodic potential of +0.2 V_{ref}, as shown in Figure 9.9A and B. This is as expected, since the potential was below the oxycarbide dissolution potential. The

Table 9.3: Iron content (mass fraction Fe/(Ti+Fe)) and initial molar Fe/Si ratio for electrochemically leached oxycarbides determined by XRF. Dissolution time of 12 hours.

Ore	Fe/(Ti+Fe)		Initial Fe/Si (molar)
	Crude	Purified	
Leucoxene	0.039	0.037	1.6
Rutile	0.017	0.009	1.6
Pseudorutile	0.126	0.048	8.0
Ilmenite	0.449	0.043	21.0

backscattered electron images (Figure 9.9C and D) show that the significant deposits of iron were removed, and only titanium oxycarbide and non-metallic inert impurities remain (such as zirconia (ZrO_2), seen as a bright particle in Figure 9.9D).

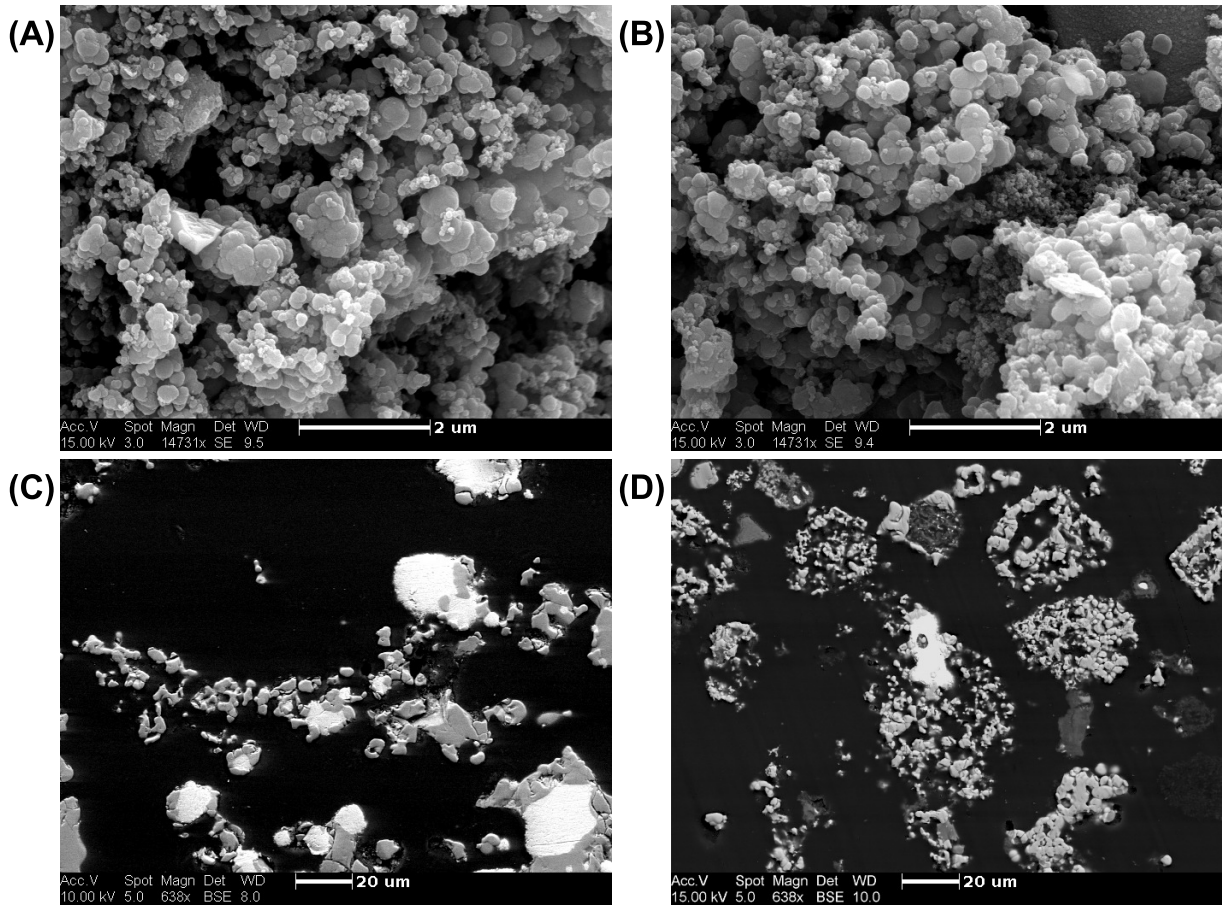

Figure 9.9: SEM images of (A) an iron-containing titanium oxycarbide, (B) an iron-containing oxycarbide after electrochemical iron removal, (C) backscattered electron image of an iron-containing titanium oxycarbide particle, and (D) a backscattered electron image of the electrochemically processed pseudorutile oxycarbide (after magnetic separation).

Table 9.3 shows that incomplete iron removal was found in all cases, and some oxycarbides (leucoxene and rutile oxycarbides) showed almost no iron removal. A magnet indicated that the purified oxycarbides all contained some magnetic particles. The magnetic particles of a purified pseudorutile oxycarbide were separated and examined in detail by backscattered imaging in the SEM, shown in Figure 9.10. EDS of the bright particles indicated that they were composed of η-phase Fe-Si, or Fe_5Si_3. It should be noted that this is the same

phase observed in the reduction of low-iron ores such as natural rutile and leucoxene mineral sands—discussed in more detail in Section 7.2. However, the Fe_5Si_3 was not present in the as-reduced oxycarbide before dissolution; it formed during electrolysis. The rings around these Fe_5Si_3 particles (determined by EDS to be mostly silicon) seem to indicate that Fe_5Si_3 undergoes anodic dissolution at +0.2 V_{ref}, but this decomposition is slow.

Closer examination of this surface layer of Fe_5Si_3 particles subjected to anodic dissolution (Figure 9.11) shows the surface is a de-alloyed and nanoporous consisting of silicon. The morphology of the surface of Fe_5Si_3 looks similar to other de-alloyed materials from literature, such as silver-gold [69]. Potentiodynamic tests on pure iron and Fe_5Si_3 shows that the current density (and therefore anodic dissolution rate) for pure iron is approximately 10 times faster than that of Fe_5Si_3 at +0.2 V_{ref}, indicating this silicon surface layer is inhibiting dissolution of Fe_5Si_3. The behavior of different phases in anodic dissolution is discussed later in Section 10.4.

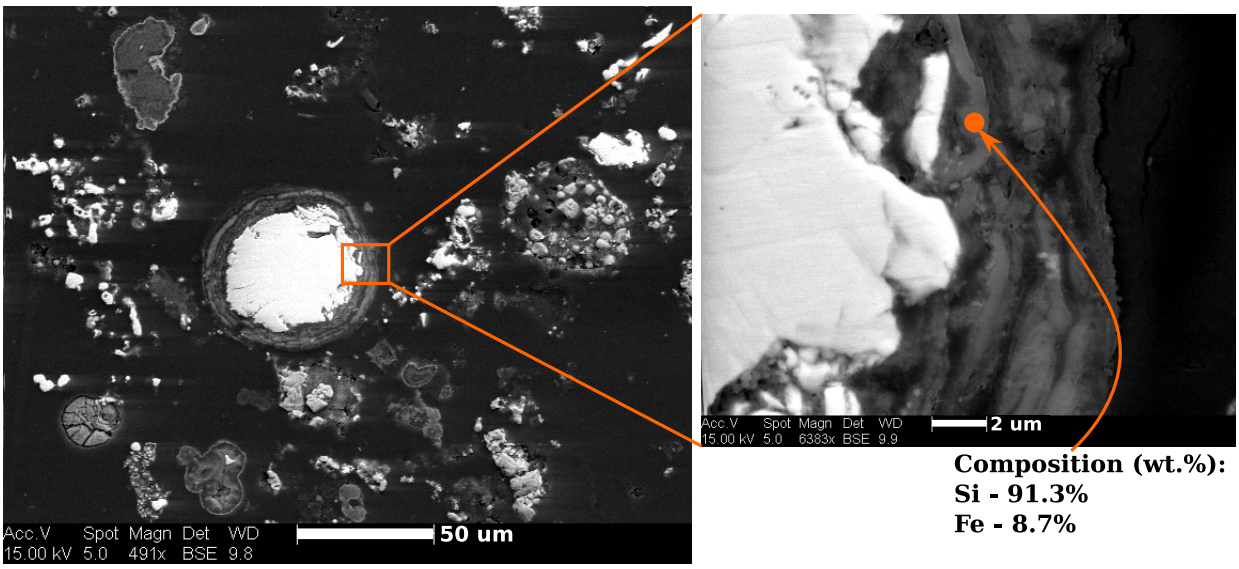

Figure 9.10: Backscattered SEM image of the magnetically separated fraction of the processed titanium oxycarbide, with zoomed in image of Fe_5Si_3 particle surface and EDS analysis of surface features. Bright particles are Fe_5Si_3.

In order for all the iron to be removed from inside of a titanium oxycarbide particle, it needs to have an open pore to the outside of the particle in order to make contact with

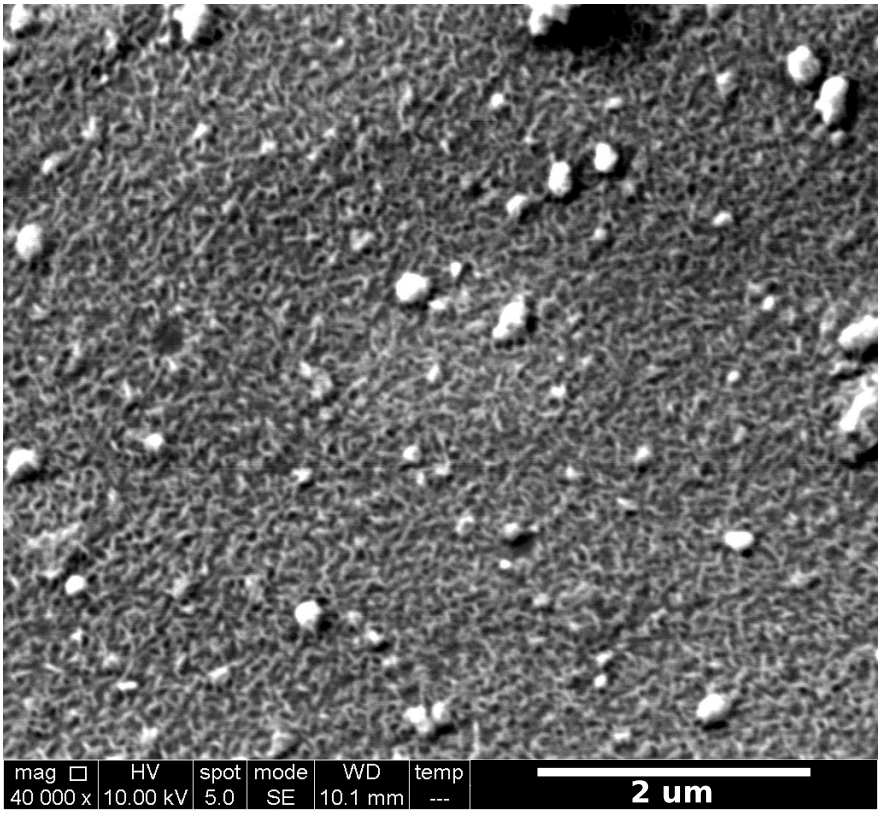

Figure 9.11: Secondary electron SEM image of the surface morphology of Fe_5Si_3 subjected to anodic dissolution showing de-alloyed surface consisting of nanoporous silicon.

the electrolyte. Based on percolation theory, an infinite face-centered cubic (FCC) or body-centered cubic (BCC) crystal lattice would need 19.8% or 24.5% missing sites respectively, to have continuous percolation throughout the volume [70]. Given that the volumetric porosity of titanium oxycarbide produced from rutile and ilmenite is 26.1% and 55.9% (from density calculations) respectively, continuous percolation of pores in titanium oxycarbide is likely. Therefore, all the metallic iron has access to the electrolyte.

The slower dissolution rate of Fe_5Si_3 explains why iron is still detected by XRF in the purified titanium oxycarbide products (Table 9.3) after the current drops to a low value at the end of the electrochemical purification. However, in the iron rich ores, the initial iron to silicon molar ratio is much higher than that of Fe_5Si_3 (Fe/Si molar ratio of 5/3) as shown in Table 9.3. If the iron and silicon in the metallic impurities dissolved at similar rates, then the iron to silicon ratio should remain constant, and Fe_5Si_3 should never form. The fact Fe_5Si_3 forms in these oxycarbides after purification indicates that the silicon is dissolving more slowly than iron. Because the iron dissolves more quickly than silicon, so the alloy composition becomes more enriched in silicon over the course of anodic dissolution. Once the molar ratio of iron to silicon reaches 5/3, then Fe_5Si_3 can form, and the overall dissolution rate decreases to the Fe_5Si_3 rate.

One potential reason for silicon's lower dissolution rate may be the activity of the silicon in the iron. In titanium oxycarbide made from iron-rich ores, the form of the metallic impurities is α-ferrite (silicon is a ferrite stabilizer, so despite the high temperature of the reactor the metallic impurities remain as ferrite). The other metallic impurities of silicon, manganese, and chromium go into solution in the ferrite in their respective ratios. For example, in pseudorutile oxycarbide the metallic impurities should have an approximate composition of 86.5 wt. % Fe, 6.0% Si, 5.2% Mn, 2.3% Cr (by weight). The activities of these different impurity metals in the ferroalloy would affect their anodic dissolution potentials. Using FactSage (with the FSstel database), the activities of each of these components was estimated

and used to determine the actual anodic dissolution potentials, shown in Table 9.4.

The largest change in potential due to activity is with silicon. The activity of silicon in iron has a significant negative deviation from the ideal solution case [71], shown in Figure 9.12. This results in a significant increase in the anodic potential for Si dissolution of 270 millivolts, putting it above the anodic dissolution potential of iron. Thus, while all the metal dissolution reactions are possible at the applied potential (+0.2 V_{ref} = -0.85 V_{Cl_2}), the silicon reaction has the lowest overpotential, potentially leading to a lower dissolution rate.

Table 9.4: Change in potentials due to activity of metallic elements in ferroalloy impurities formed in Pseudorutile oxycarbide. Calculated with FactSage using FSstel database; Reference state: pure solid elements.

Reaction	E_{Cl_2}, V (pure)	E_{Cl_2}, V (Pseudorutile)	Activity
$FeCl_2 + 2\,e^- \longrightarrow Fe + 2\,Cl^-$	-1.11	-1.09	6.66×10^{-1}
$SiCl_4 + 4\,e^- \longrightarrow Si + 4\,Cl^-$	-1.23	-0.96	9.40×10^{-6}
$CrCl_2 + 2\,e^- \longrightarrow Cr + 2\,Cl^-$	-1.36	-1.25	9.73×10^{-2}
$MnCl_2 + 2\,e^- \longrightarrow Mn + 2\,Cl^-$	-1.81	-1.65	3.26×10^{-2}

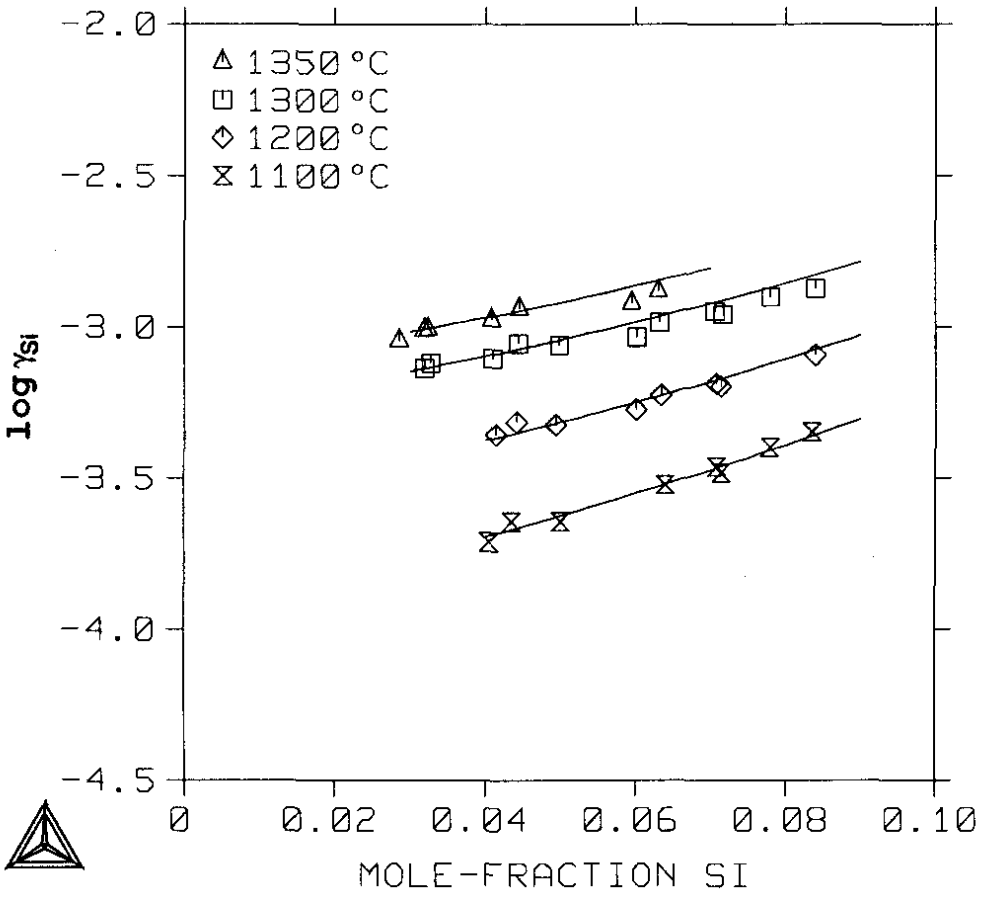

Figure 9.12: Plot of silicon activity coefficient in α-Fe as a function of silicon mole fraction for various temperatures [71]

Chapter 10

Electrochemical Characterization

Electrochemical characterization was performed on a wide variety of anode materials to establish their electrochemical behavior during electrolysis, as well as experiments to characterize the behavior of plating on the cathode. This was performed by a combination of electrochemical impedance spectrometry (EIS) and polarization.

10.1 Calculations from Geometry

Without any characterization at all, the cell used in these experiments can be modeled. Factors such as the shape of the electrodes are important. The simplest type of cell to model was a simplified version of the cell used to perform electrochemical leaching of oxidized pseudorutile, described in 9.1. In this case, the working electrode was a strip of steel (1 centimeter in width, and immersed to a depth of 3 centimeters into the melt), and The counter electrode was a graphite rod (1.25 cm in diameter, immersed to a depth of 3 centimeters).

For this cell, the ohmic resistance term was estimated with shape factors [72]. The solution resistance from the surface of an electrode is given by $1/(\kappa S)$, where κ is the conductivity of the electrolyte and S is the shape factor of the electrode. The conductivity of molten NaCl-

KCl eutectic at 800 °C is approximately 2.4 S/cm [73]. The shape factor can be estimated using the relationships reported by Yovanovich [74, 75], who showed that for many convex surfaces, the shape factor is given by $c(A)^{0.5}$, where A is the (wetted) electrode area, and c is a constant which depends weakly on geometry, and is generally in the range 3-4. In this calculation, it is assumed that the working and counter electrodes are separated by a large enough distance that the relationships for conduction to a semi-infinite medium holds; this would be the case if the separation of the electrodes is larger than the characteristic dimension of the electrode.

For a thin rectangular electrode, $c = 3.3$ [75]. Taking into account the effect of the insulating electrolyte-gas interface, the shape factor for conduction from both sides of the electrode is $3.3(2LW)^{0.5} = 11.4$ cm. Using these values, the ohmic resistance from the working electrode is then estimated as 36 mΩ. For the graphite counter electrode, $c \approx 3.5$ [75], giving a similar solution resistance at the counter electrode of approximately 33 mΩ. It should be noted that the solution resistance at the counter electrode would not affect potentiostatic measurements, but would affect the total applied cell potential.

The capacitance associated with the electrode-molten salt interface was also estimated. From the literature, the actual value of the interfacial capacitance varies with the molten salt and temperature [76, 77] but is generally on the order of magnitude of 1-10 μF/cm^2.

The measured resistance and capacitance are reported in 10.2. The ohmic resistance was generally much higher (around 1 Ω) than that estimated from the solution conductivity (typically less than 0.1 Ω), likely because of contact resistance in the leads to the working electrode.

10.2 Cell Impedance (EIS)

To experimentally determine the impedance of the cell, we used electrochemical impedance spectrometry (EIS). This impedance data was used to determine the resistance and capacitance of the working electrode. Four different electrodes were tested (as powders in a graphite anode basket): titanium oxycarbide, vanadium oxycarbide, iron, and η-ferrosilicon (Fe_5Si_3). This information is summarized in Table 10.1, and bode and capacitance plots are given in Figures B.1 to B.8.

Table 10.1: Summary of EIS experiments, showing material, mass, particle size and estimated specific area, estimated polarization resistances, and measured ohmic resistances.

Electrode material	Mass (g)	Particle morphology	Estimated specific area (cm^2/g)	C/A ($\mu F/cm^2$)	$R_\Omega^{meas.}$ (Ω)
Ti(O,C)	1.50	Flaky	7929	5.07	0.43
V(O,C)	0.83	Flaky	9983	1.10	0.27
Fe	6.00	Flaky	932	1.96	1.75
Fe_5Si_3	3.00	Angular	246	18.5	1.45

The resistances measured were generally higher than what was expected from the shape factor calculations from Section 10.1. This is likely due to contact resistance between the actual anode to the potentiostat (the anode material makes contact with the graphite anode, to the platinum wire, to the graphite rod, to the Kanthal wire, to the stainless steel rod, to the potentiostat voltage lead).

It should be noted that these capacitance measurements may not be very accurate, as the magnitude of the imaginary component is very small, and is affected by the inductance of the leads, making calculations subject to considerable error. However, the specific capacitance values are reasonably close to values in the literature (on the order of 1-10 $\mu F/cm^2$ for NaCl and KCl in contact with a liquid metal electrode) [76, 77]. The capacitance of Fe_5Si_3 is higher than the other materials tested, but this higher capacitance is probably due to the very high surface area of the de-alloyed nanoporous surface of Fe_5Si_3 subjected to anodic dissolution

(discussed in Section 9.3). This additional nanoporosity would contribute significantly to the surface area of the material, and is not accounted for in the surface area estimates for Fe_5Si_3 by SEM.

10.3 Polarization Curves

Polarization curves were obtained from different anode powder materials. These experiments were performed after at least one hour of electrolysis in order to remove water and dope the electrolyte with the relevant ion species. The parameters of the different experiments are summarized in Table 10.2, and the actual polarization curves are shown in Figures 10.1 through 10.4. Potentials are relative to the Ag/AgCl reference electrode. Current densities were calculated by dividing the current by the anode area, estimated from the particle sizes and sample mass. Polarization resistance ($R_{\text{pol.}}$) was calculated from the polarization curves using Equation 10.1:

$$R_{\text{pol.}} = \left(\frac{dE}{dI}\right)_{I=0} \tag{10.1}$$

Table 10.2: Summary of polarization experiments, showing material, mass, particle size and estimated specific area, estimated polarization resistances, and measured ohmic resistances.

Electrode material	Mass (g)	Particle morphology	Estimated specific area (cm^2/g)	$R_{\text{pol.}}$ (Ω)	$R_{\Omega}^{\text{meas.}}$ (Ω)
Ti(O,C)	1.50	Flaky	7929	1.53	0.43
V(O,C)	0.83	Flaky	9983	0.94	0.27
Fe	6.00	Flaky	932	0.69	1.75
Fe_5Si_3	3.00	Angular	246	1.28	1.45

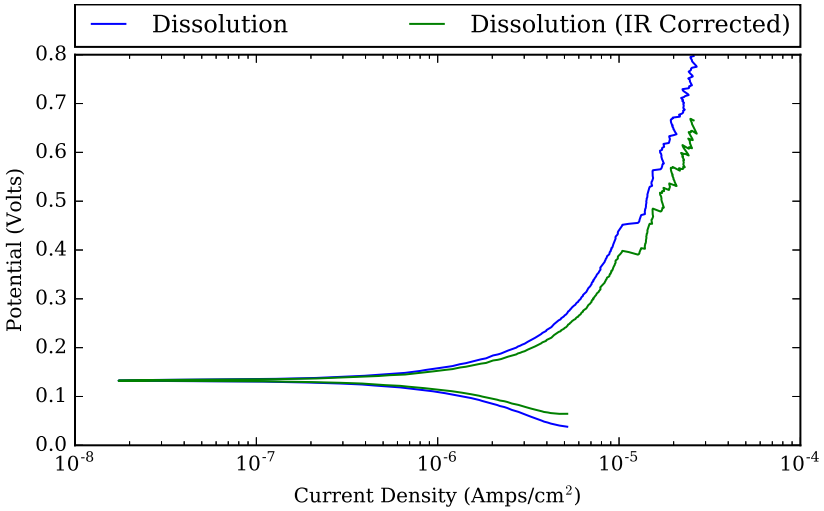

Figure 10.1: Polarization curve for titanium oxycarbide anode (surface area = 11893 cm^2).

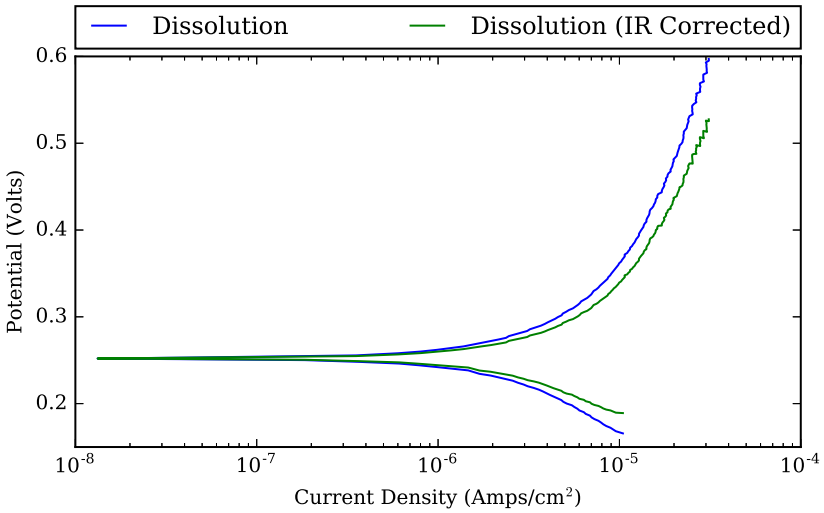

Figure 10.2: Polarization curve for vanadium oxycarbide anode (surface area = 8286 cm^2).

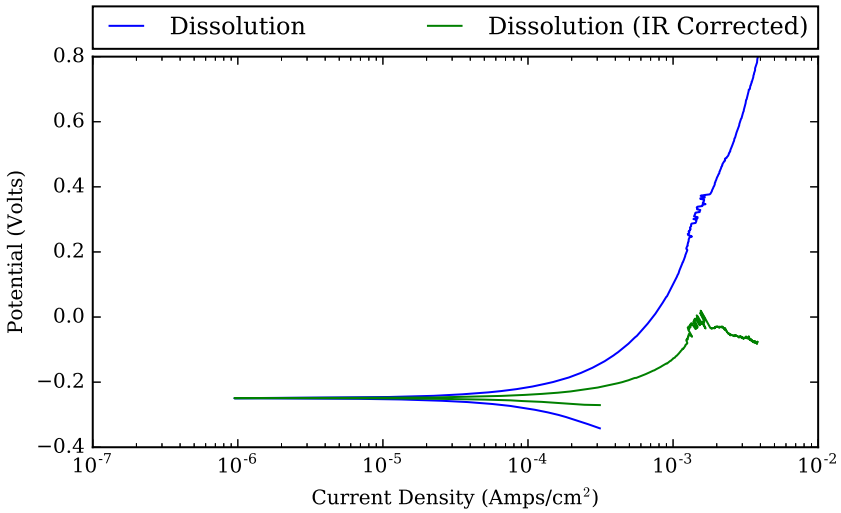

Figure 10.3: Polarization curve for iron powder anode (surface area = 5590 cm^2).

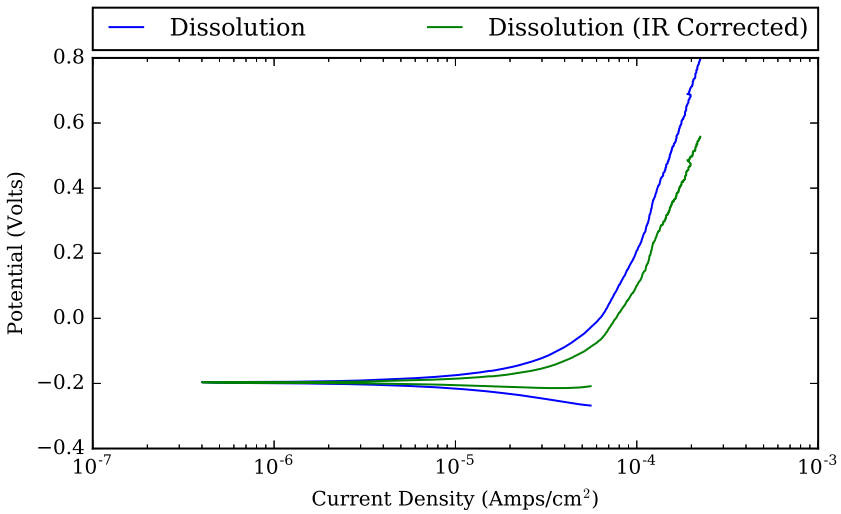

Figure 10.4: Polarization curve for Fe_5Si_3 powder anode (surface area = 737 cm^2).

10.3.1 Vanadium Oxycarbide Polarization (anodic)

The solution thermodynamics of the vanadium oxycarbide system are not very well characterized, but the ideal solution model can be used to make a first order approximation of the Gibbs free energy of V_2OC, and therefore its anodic dissolution potential. The ideal solution model of V_2OC indicated that the anodic dissolution potential is +0.15 V_{ref}.

The measured polarization curve (Figure 10.2) does not appear to show any inflections or discontinuities that would indicate that a reaction is beginning, but does show a very high rest potential. If the anodic potential were at this rest potential, then that would mask the anode dissolution potential as the rest potential is in itself a discontinuity on a log scale plot. Based on this reasoning, we have determined that the anodic dissolution potential of vanadium oxycarbide is approximately +0.25 V_{ref} or -0.81 V_{Cl_2}.

This experimentally determined anode potential could be used to provide us with a better approximation of the solution thermodynamics of the vanadium oxycarbide system, using the regular solution model. Using the Nernst equation (Equation 3.1), we found the Gibbs free energy of the vanadium oxycarbide dissolution reaction, and this was used to calculate the activity of VO and VC in V_2OC (if we assume the composition is equimolar VO and VC, then the activities would be equal), which can be used to produce the necessary extra term for the regular solution model (Ω). This model is by no means accurate, but it does provide a useful second-order approximation, and is an improvement over the ideal solution model.

$$E = \frac{\Delta G}{zF} \qquad \text{(3.1 revisited)}$$

$$-0.81\ \text{V} = \frac{\Delta G}{(4)(96485\ \text{C/mol})}$$

$$\Delta G = -312499\ \text{J/mol}$$

$$VCl_2 + CO \longrightarrow 2\,Cl_2 + VO + VC$$

$$\Delta G^0 = 363974 \text{ J/mol}$$

$$\Delta G_{\text{exp}} = 312499 \text{ J/mol}$$

$$= \Delta G^0 + RT \ln(a_{\text{VO}} a_{\text{VC}})$$

$$a_{\text{VO}} = a_{\text{VC}} = 0.0559$$

$$\gamma_{\text{VO}} = \frac{a_{\text{VO}}}{X_{\text{VO}}}$$

$$= e^{\Omega(1-X_{\text{VO}})/RT}$$

$$\Omega = -78216 \text{ J/mol}$$

10.4 Dissolution Rates

As previously discussed in Section 9.3, electrochemical removal of impurities from titanium oxycarbide was hampered by the formation of Fe_5Si_3—which while electrochemically active—dissolved very slowly. However, if the dissolution rate of Fe_5Si_3 was slow enough compared to titanium oxycarbide plating, ASTM Grade 2 titanium could be made with titanium oxycarbide which contains Fe_5Si_3.

To test this idea, polarization curves for titanium oxycarbide and Fe_5Si_3 dissolution determined in Section 10.3—which were normalized to the surface areas of the anode material used—were "un-normalized" with the surface areas of Ti_2OC and Fe_5Si_3 from leucoxene oxycarbide.

Leuxocene oxycarbide SEM images were analyzed to determine the specific surface areas of both the titanium oxycarbide and Fe_5Si_3. This was multiplied by the mass of each phase (one gram of leucoxene oxycarbide yields 705 milligrams of Ti_2OC and 20 milligrams of Fe_5Si_3) to produce total surface area, which was used to convert the polarization curve from current density to current. It should be noted that compared to other iron-containing systems, the surface area of leucoxene oxycarbide is lower and its Fe_5Si_3 particles smaller, providing a

more conservative estimate for dissolution rates). Based on the total surface areas of the titanium oxycarbide and Fe_5Si_3 systems (5590 cm^2 and 4 cm^2 respectively), the polarization curve shown in Figure 10.5 was obtained.

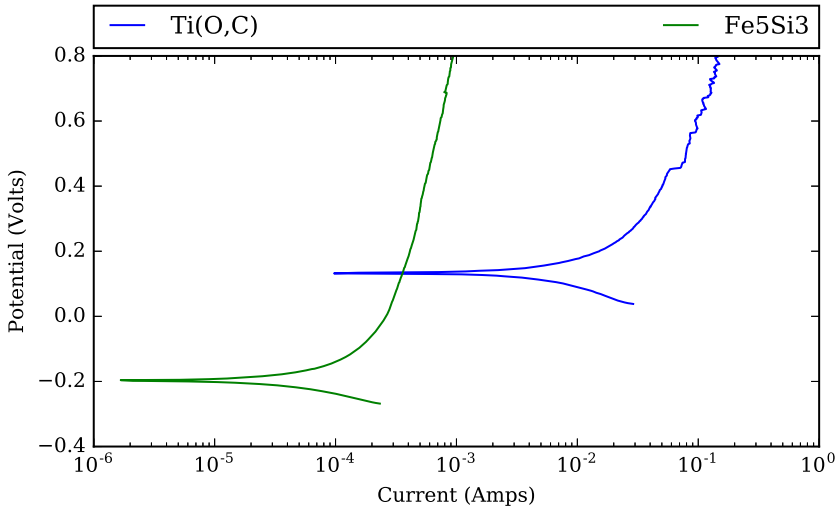

Figure 10.5: Polarization curves for 0.703 grams of titanium oxycarbide and 0.02 grams of Fe_5Si_3 using leucoxene oxycarbide surface areas.

On average, the titanium oxycarbide curve shows currents that are two orders of magnitude larger than the Fe_5Si_3 curve (at +0.71 V_{ref} the current for titanium oxycarbide is 160 times higher than that of Fe_5Si_3). From this analysis, the resulting alloy would be 0.33% Fe and 0.05 % Si by weight (balance Ti). This does not meet ASTM Grade 2 specifications (0.3% Fe and 0.1% Si), but as noted previously this would be different for a titanium oxycarbide produced from a low-grade ore and electrochemically purified (which would have higher titanium oxycarbide surface area and lower Fe_5Si_3 surface area)—it seems likely that a titanium oxycarbide and Fe_5Si_3 mixture from an electrochemically purified ilmenite oxycarbide would be able to meet the ASTM Grade 2 specification.

10.5 Cathode Monitoring

One of the advantages of the MER process is that the cathodic product morphology can be controlled: higher current densities give finer dendritic deposits. In principle, the cathode capacitance can be used to monitor the cathode morphology. To test this cathode impedance was monitored for high and low anode overpotentials, and at 3 different temperatures (700, 800, and 900 °C), while producing titanium from Ti_2OC (produced from TiO_2 pigment).

As this was a long multi-part experiment, the procedure has been summarized in the list below:

1. A graphite anode basket was filled completely with pure Ti_2OC.
2. The electrolyte was prepared and pre-electrolyzed per standard procedure.
3. The furnace was taken to new working temperature (initially 700 °C).
4. A new titanium cathode was inserted (old cathode removed if applicable).
5. The reference electrode tube was removed from the molten salt for 5 minutes, then reinserted and 4% AgCl was generated galvanostatically.
6. EIS was performed on the cathode.
7. The system was run potentiostatically at low overpotential (+0.5 V_{ref}) for 1.5 hours.
8. EIS was performed on the cathode.
9. The system was run potentiostatically at the same potential for an additional 1.5 hours.
10. EIS was performed on the cathode.
11. This procedure was repeated from Step 4 for high overpotential (+0.8 V_{ref}).
12. Cathode was removed and the furnace was cooled down to 400 °C (under flowing argon gas) overnight.
13. The next day, repeat procedure from Step 3, with 800 °C and 900 °C.
14. Upon conclusion of the experiment, shut down reactor per standard procedure.

It immediately became evident that the cathode thickness is not something that can be

easily analyzed, as most of the titanium deposit fell off the cathode upon removal from the electrolyte. As such only the "stubs" of the deposit on the cathode surface could be analyzed after the measurements for an indication of the deposit morphology.

During these runs, the system was operated potentiostatically to ensure that the anode potential remained above +0.45 V_{ref} (to put titanium into solution), and below +1.00 V_{ref} (to prevent electrolyte decomposition).

The average current during the potentiostatic runs is shown in Table 10.3. The capacitance was determined from the EIS measurements, and is shown in Table 10.4.

The capacitance would increases if the electrode area increased, which would be the case when the titanium deposit (which we expect to be dendritic in nature) grows. The capacitance was generally lower at the higher temperatures, despite increasing current density. This could be indicative of a change in microstructure with temperature (sintering of the dendrites), and possible loss of fine dendritic deposits from the electrode surface. It is expected that a high enough current density would lead to dendrites that are so fine that they would fall off the cathode immediately, forming a powder. This is actually observed in the case which had the highest current density overall current density (+0.5 V_{ref} at 900 °C)—the capacitance was too low to measure in any of the three measurements.

The expected value for capacitance based on data in the literature varied from 1-10 microfarads per square centimeter [77]. However, none of the blank electrodes showed any measurable capacitance, this was likely because of the low polarization resistance caused by the rapid cathodic reaction.

Attempts to remove the salt off the surface of the cathodes without disturbing the titanium deposit were unsuccessful, as any washing of the deposit would remove whatever was on the surface of the cathode (resulting in the loss of dendrites on the +0.5 V_{ref} at 700 °C sample before imaging). As such, the only imaging was with optical microscopy of unwashed samples. The images are shown in Figure 10.6.

Table 10.3: Average cathode current density (in mA/cm^2) at different temperatures.

T = 700 °C		
Time (hr)	+0.5 V_{ref}	+0.8 V_{ref}
0 - 1.5	15.34	25.57
1.5 - 3	4.61	8.73

T = 800 °C		
Time (hr)	+0.5 V_{ref}	+0.8 V_{ref}
0 - 1.5	9.30	30.71
1.5 - 3	18.02	19.23

T = 900 °C		
Time (hr)	+0.5 V_{ref}	+0.8 V_{ref}
0 - 1.5	102.33*	70.77
1.5 - 3	41.37	35.37

* Run was stopped prematurely due to hitting current limit (< 2 A)

Table 10.4: Cathode capacitance (in F/cm^2) at different temperatures, based on a projected electrode area of 12 cm^2. The potentials in the heading are those at the oxycarbide anode, and potentials listed in parentheses are the cathode potentials at which potentiostatic EIS was performed (rest potential).

T = 700 °C		
Time (hr)	+0.5 V_{ref}	+0.8 V_{ref}
0	— (-1.03 V_{ref})	— (-0.96 V_{ref})
1.5	1.65×10^{-5} (-1.50 V_{ref})	3.20×10^{-5} (-1.62 V_{ref})
3	2.90×10^{-5} (-1.48 V_{ref})	5.57×10^{-5} (-1.38 V_{ref})

T = 800 °C		
Time (hr)	+0.5 V_{ref}	+0.8 V_{ref}
0	— (-0.96 V_{ref})	— (-1.07 V_{ref})
1.5	1.99×10^{-6} (-0.89 V_{ref})	2.06×10^{-5} (-1.34 V_{ref})
3	1.77×10^{-6} (-0.81 V_{ref})	3.09×10^{-5} (-1.29 V_{ref})

T = 900 °C		
Time (hr)	+0.5 V_{ref}	+0.8 V_{ref}
0	— (-0.62 V_{ref})	— (-0.95 V_{ref})
1.5	— (-0.36 V_{ref})	3.79×10^{-5} (-0.86 V_{ref})
3	— (-0.57 V_{ref})	3.33×10^{-5} (-0.61 V_{ref})

(a) +0.8 V_{ref}, 973 K

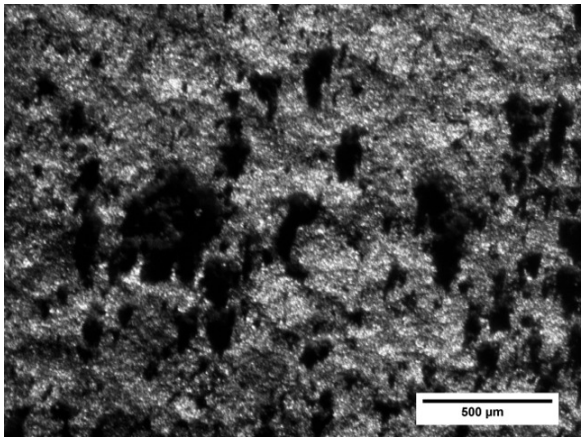

(b) +0.8 V_{ref}, 1073 K

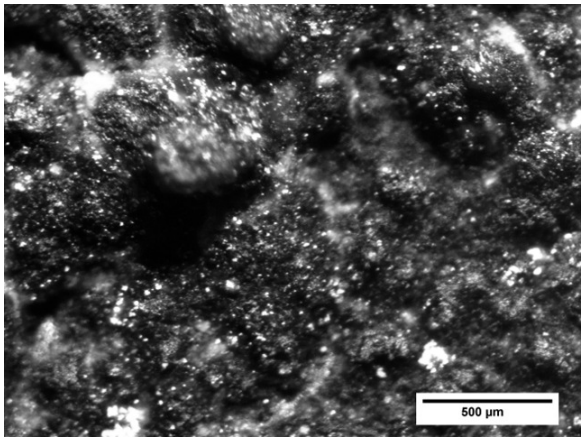

(c) +0.5 V_{ref}, 1073 K

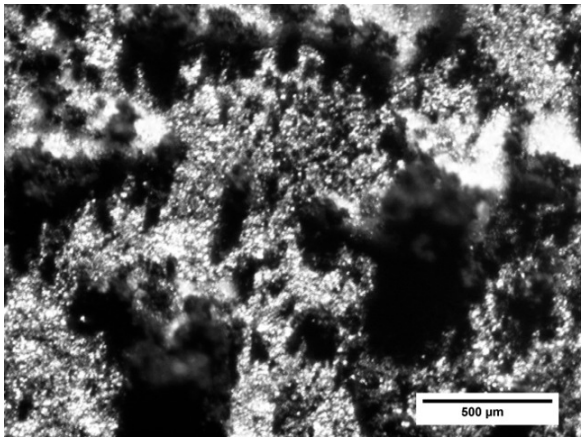

(d) +0.5 V_{ref}, 1073 K (refocus of (c))

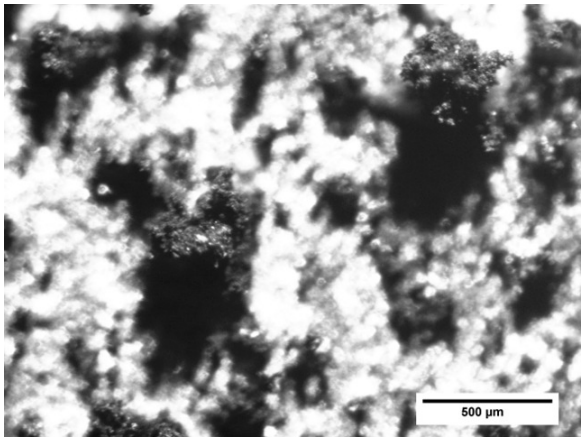

(e) +0.5 V_{ref}, 1173 K

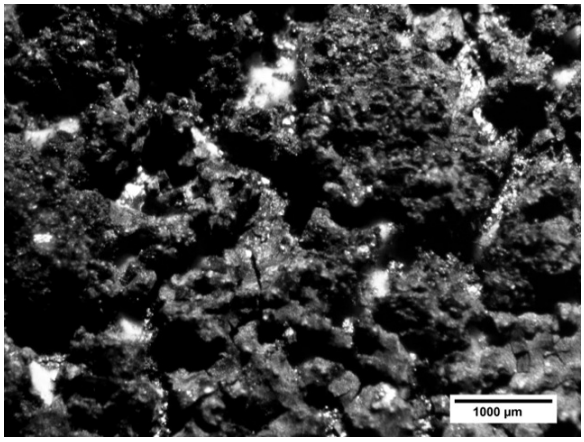

(f) +0.8 V_{ref}, 1173 K

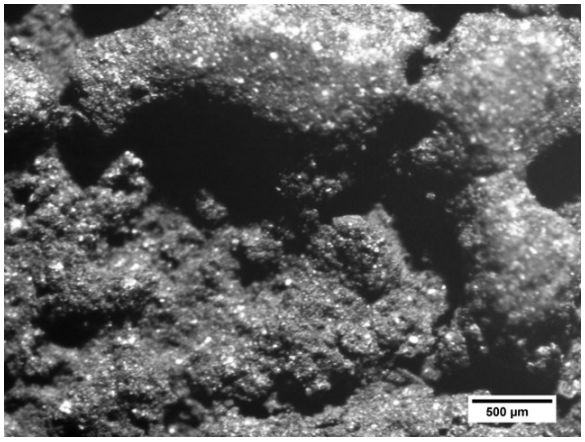

Figure 10.6: Optical microscope images of titanium cathode surfaces after electrolysis under varying conditions.

At +0.8 V_{ref} and 700 °C (Figure 10.6a), the surface of the electrode is largely flat, with protrusions which are likely dendrite "stubs". At +0.5 V_{ref} and 800 °C, the surface is still fairly flat (but rougher), and large dendrite features are visible (Figures 10.6c and d). As temperature and current density increase, the surface of the cathode becomes less flat, and dendrite features begin to disappear (Figures 10.6b, e and f). This reflects the previous capacitance measurements – as current density increases, dendrites become larger and finer, and thus more fragile, so they will be less likely to be seen on the cathodes after removal from the electrolyte.

A separate observation was made regarding anodic behavior (oxycarbide dissolution): there appears to be an "activation" period after the dissolution potential is applied. In general, the current tended to increase before leveling off at a steady-state value, as illustrated by Figure 10.7. The reasons for this are not clear, as the active area is expected to decrease over time due to carbon monoxide bubble formation and oxycarbide dissolution.

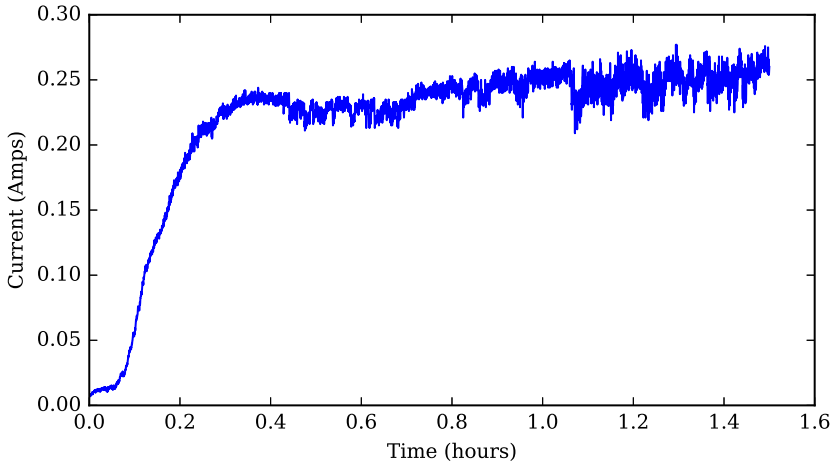

Figure 10.7: Potentiostatic curve of +0.5 Vref, 1073 K, 1.5-3 hours. Illustrates "activation" effect.

10.6 Anode Monitoring

As mentioned in previous chapters, the porosity in each of the titanium oxycarbide particles, coupled with the inherent porosity due to pelletizing, may cause the anode to become buoyant in the electrolyte when carbon monoxide is generated. Therefore, a way of monitoring the reactor to determine whether anode flotation is occurring would be useful. However, events that appeared to be characteristic of anode flotation were not generally observed (even at high currents) and apparent flotation was only observed once.

This was in the case of the conductive ilmenite electrode described in Section 9.2. The binder (carbonized caramel) was very coarse, so the overall pellet density was low. The potentiostatic current plot seems to show erratic behavior when suspected anode flotation was occurring as shown in Figure 10.8. If this behavior is characteristic of anode flotation, then it might be easy to determine when anode flotation is occurring.

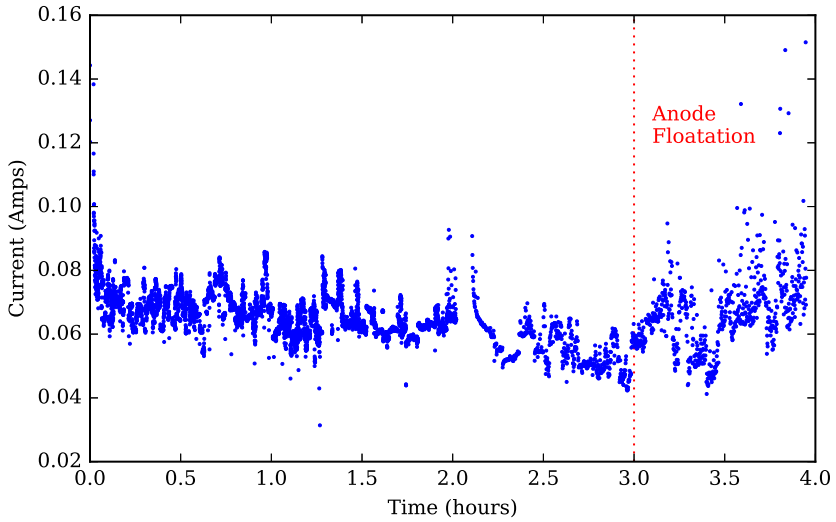

Figure 10.8: Current plot of ilmenite electrode method of iron dissolution. Dotted line denotes approximately when anode flotation likely began.

In principle, another method for determining whether anode flotation is occurring would be to perform EIS in-situ. If an anode pellet begins to float, then it loses electrical contact with

the graphite anode basket, decreasing the active area. As such, EIS should be able to detect flotation as a sudden decrease in capacitance.

Chapter 11

Conclusions

The hypotheses of this project, as set out in Chapter 4, were as follows:

1. Titanium oxycarbide of sufficient purity to meet the ASTM Grade 2 standard can be produced from some low-grade titanium ores by removing all "reducible" impurities before titanium electroplating.

2. The kinetics of carbothermal titanium oxycarbide reduction is limited by pore diffusion.

In this document, it is shown that it is possible to make titanium oxycarbide directly from high-grade natural titanium ores such as rutile and leucoxene, or synthetic materials such as UGS, by carbothermal reduction followed by magnetic separation of the undesired metallic iron (Section 7.2). However, magnetic separation on other titanium oxycarbide materials produced from lower grade ores—such as titaniferous slags, psuedorutile, and ilmenite—is not possible, as magnetic separation would remove most of the oxycarbide with the metallic iron.

Chemical leaching of titanium oxycarbide is impractical, as leaching tends to cause the titanium oxycarbide itself to oxidize, lowering the yield (Section 8.1). A method to "upgrade" the feedstock material prior to carbothermal reduction using a molten salt upgraded a pseu-

dorutile mineral sand to leucoxene levels of purity (Section 9.1). However, this leaching process takes a long time and only works on fully oxidized materials, making it impractical for ilmenite mineral sands.

Using careful control of the anode potential, it was possible to remove most of the iron (some iron and silicon remained as Fe_5Si_3) from iron-bearing titanium oxycarbides produced from lower grade materials such as pseudorutile and ilmenite (Section 9.3). This process was relatively fast, and uses the same electrode configuration and setup as the MER titanium cell. Thus, removal of iron can be performed as an additional process step, without the need for additional equipment. The results of this process lends considerable support to Hypothesis 1.

Electrochemical tests confirmed our calculated equilibrium anodic dissolution potentials. Polarization measurements were used to estimate the rate of dissolution of titanium oxycarbide relative to Fe_5Si_3—an impurity that is difficult to remove by electrochemical means (Section 10.4); in some cases the effect of Fe_5Si_3 on product purity may be negligible due to its very low rate of anodic dissolution. This means that Hypothesis 1 is not entirely true: titanium oxycarbide which can produce ASTM Grade 2 titanium can be produced without removal of all reducible impurities, as Fe_5Si_3 is a metallic impurity and may be ignored in some cases.

Tests of the effect of particle size and type of carbon reductant on the kinetics of the carbothermal titanium oxycarbide reduction reaction (Section 7.8) demonstrated a strong effect of the reductant used, showing that the kinetics of titanium oxycarbide reduction are not dictated by only pore diffusion control—the reactions are clearly governed by mixed control. This effectively refutes Hypothesis 2.

Overall, the use of a lower-grade titanium mineral such as ilmenite as a feedstock to the MER process would be economically favorable, compared to a higher grade titanium oxide feedstock such as rutile. Rough estimates of the cost of production of titanium by the MER process as outlined in this document show that despite the additional energy input required

for titanium oxycarbide purification, the cost of titanium from ilmenite (1.87 USD/kg Ti) would be significantly less than if rutile was used as the feedstock material (2.29 USD/kg Ti). This analysis is explained in more detail in Appendix C.

Appendix A

Shrinking Core Calculations

As discussed in Section 7.8, the equations (7.1 and 7.2) governing shrinking core kinetics involve several variables. But first, the general form of Equation 7.1 is given by Equation A.1:

$$\dot{n}_{CO_2} = X_{CO_2}\dot{n}_{gas}^{out} + D_{eff}\Delta C\frac{4\pi r_o r_i}{r_o - r_i} = -4\pi r_i^2\rho_n Z\frac{dr_i}{dt} \tag{A.1}$$

The term $X_{CO_2}\dot{n}_{gas}^{out}$ is referred to as the "bulk flow term". This accounts for any mismatch between the moles of gas consumed in the reaction compared to the number of moles generated. However, as the value of the term X_{CO_2} is very small (X_{CO_2} is obtained from Figure 3.3), the bulk flow term can be neglected. This results in Equation 7.1 and the integrated equation in 7.2.

$$\dot{n}_{CO_2} = D_{eff}\Delta C\frac{4\pi r_o r_i}{r_o - r_i} = -4\pi r_i^2\rho_n Z\frac{dr_i}{dt} \tag{7.1 revisited}$$

$$\frac{1}{6}r_o^2 + \frac{1}{3r_o}r_i^3 - \frac{1}{2}r_i^2 = \frac{D_{eff}\Delta C}{Z\rho_n}t \tag{7.2 revisited}$$

While some of these variables are relatively simple to understand. r_o corresponds to the particle size (outer radius) of the particle of (initially) Ti_2O_3 being reduced. r_i corresponds

to the radius of the unreacted core of Ti_2O_3, which decreases as the reaction proceeds. While r_i decreases as the reaction proceeds, extent of reaction f is often used, determined from r_o and r_i by Equation A.2:

$$f = 1 - \left(\frac{r_i}{r_o}\right)^3 \tag{A.2}$$

The concentration gradient arises from the difference in concentration of the product gas (in this case CO_2) within the particle itself. This is determined by the equilibrium CO_2 concentration produced by Reactions 3.5 and 3.3. These actual values are shown in Figure 3.3 as a mole fraction (X_{CO_2}) (the difference ΔX_{CO_2} is obtained by subtracting the two constant values from the figure). To convert these values to concentration values ΔC_{CO_2}, we can use Equation A.3:

$$Ti_2O_3 + 4\,CO \longrightarrow Ti_2OC + 3\,CO_2 \tag{3.5 revisited}$$

$$C + CO_2 \longrightarrow 2\,CO \tag{3.3 revisited}$$

$$\Delta C_{CO_2} = \frac{P}{RT}\Delta X_{CO_2} \tag{A.3}$$

The effective diffusion coefficient D_{eff} is determined from a combination of pore and Knudsen diffusion [78]. The Knudsen diffusivity (D_K) deals with diffusion when the mean free path of a gas particle is less than the size of the pore ($d_{\text{pore}} = 3$ μm). This is calculated by Equation A.4. The other diffusion coefficient is pore diffusivity D_{pore}, which is determined by Equation A.5 which is determined from bulk diffusivity D_{bulk} (determined from a fitted binary diffusion equation for CO and CO_2 [79] to be 0.355 cm^2/s) and the tortuosity of the pores, τ—approximated here as the inverse of porosity, ϵ ($\epsilon_{Ti(O,C)} = 0.261$). After the values of D_K and D_{pore} have been determined, we can find effective diffusivity D_{eff} by Equation

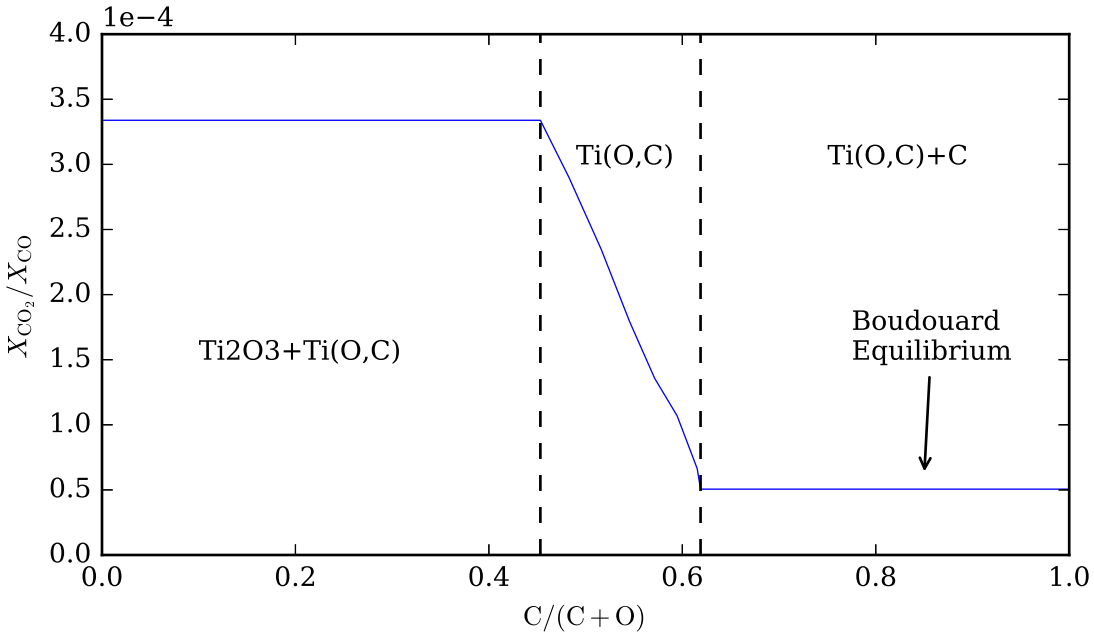

Figure 3.3: Effect of reaction extent on equilibrium CO_2 molar ratio in titanium oxycarbide at T = 1600 °C, P = 1 atm (Calculated with FactSage using database from Cao et al. [30]). The x-axis is the molar ratio C to (C + O) in the solid; zero corresponds to Ti_2O_3 and 1 to TiC (repeated from page 13)

A.6.

$$D_{\mathrm{K}} = \frac{d_{\mathrm{pore}}}{3}\sqrt{\frac{8RT}{\pi M_{\mathrm{CO}}}} \tag{A.4}$$

$$D_{\mathrm{pore}} = D_{\mathrm{bulk}}\left(\frac{\epsilon}{\tau}\right) = D_{\mathrm{bulk}}\epsilon^2 \tag{A.5}$$

$$D_{\mathrm{eff}} = \frac{1}{\frac{1}{D_{\mathrm{K}}} + \frac{1}{D_{\mathrm{pore}}}} \tag{A.6}$$

$$D_{\mathrm{eff}} = \frac{1}{\frac{1}{11.82} + \frac{1}{0.24}} = 0.237\mathrm{cm}^2/\mathrm{s}$$

The factor Z is defined as being the amount of product gas generated per mole of reactant—in our case this is dictated by Reaction 3.5—which shows that $Z = 3$.

Appendix B

Electrochemical Characterization Figures

Many of the plots from Chapter 10 are shown here.

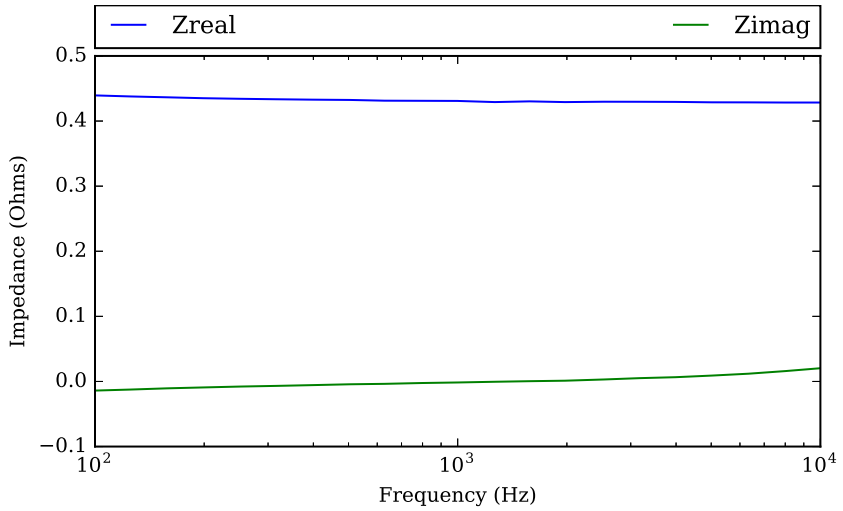

Figure B.1: Real and imaginary components of impedance for a titanium oxycarbide anode in a NaCl-KCl electrolyte.

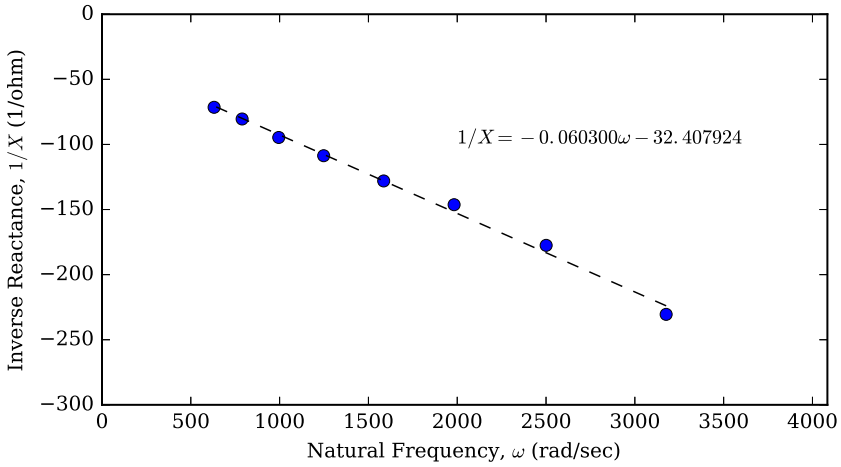

Figure B.2: Plot of inverse reactance (1/X) versus natural frequency for a titanium oxycarbide anode in a NaCl-KCl electrolyte (surface area = 11893 cm^2). Slope is capacitance.

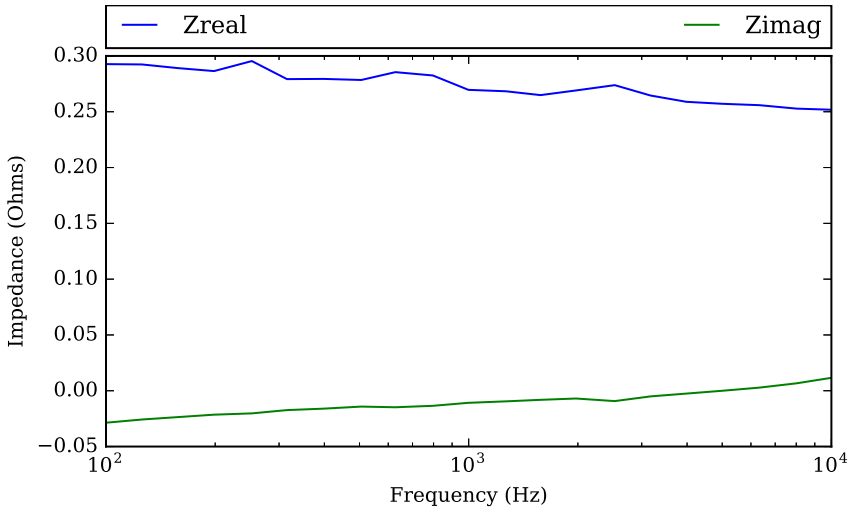

Figure B.3: Real and imaginary components of impedance for a vanadium oxycarbide anode in a NaCl-KCl electrolyte.

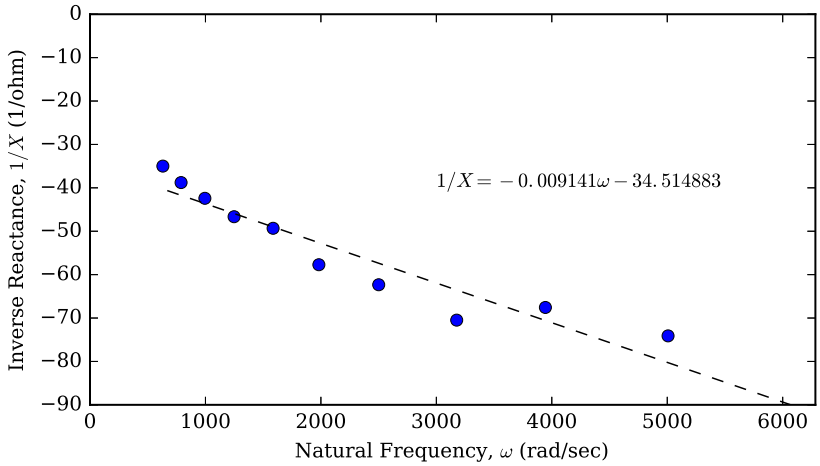

Figure B.4: Plot of inverse reactance (1/X) versus natural frequency for a vanadium oxycarbide anode in a NaCl-KCl electrolyte (surface area = 8286 cm^2). Slope is capacitance.

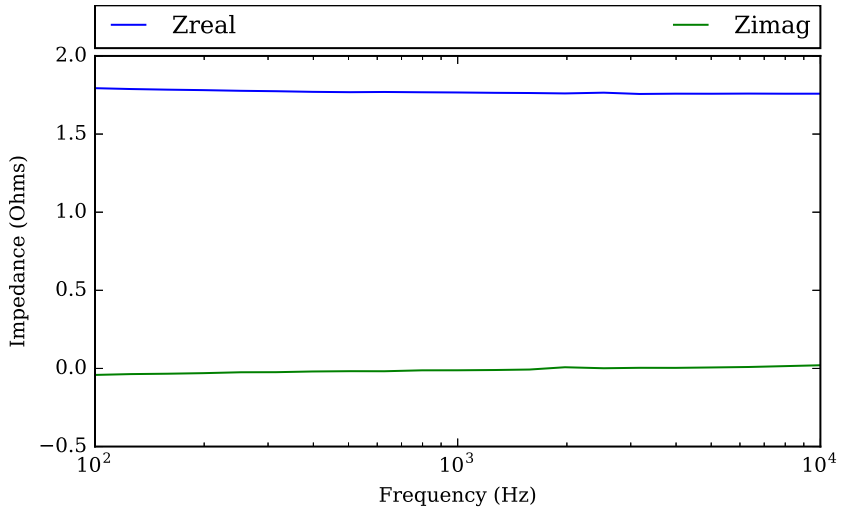

Figure B.5: Real and imaginary components of impedance for an iron powder anode in a NaCl-KCl electrolyte.

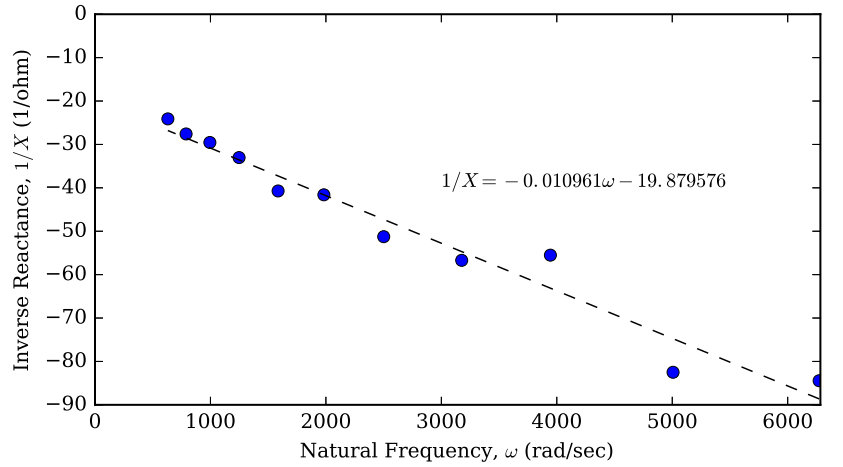

Figure B.6: Plot of inverse reactance (1/X) versus natural frequency for an iron powder anode in a NaCl-KCl electrolyte (surface area = 5590 cm^2). Slope is capacitance.

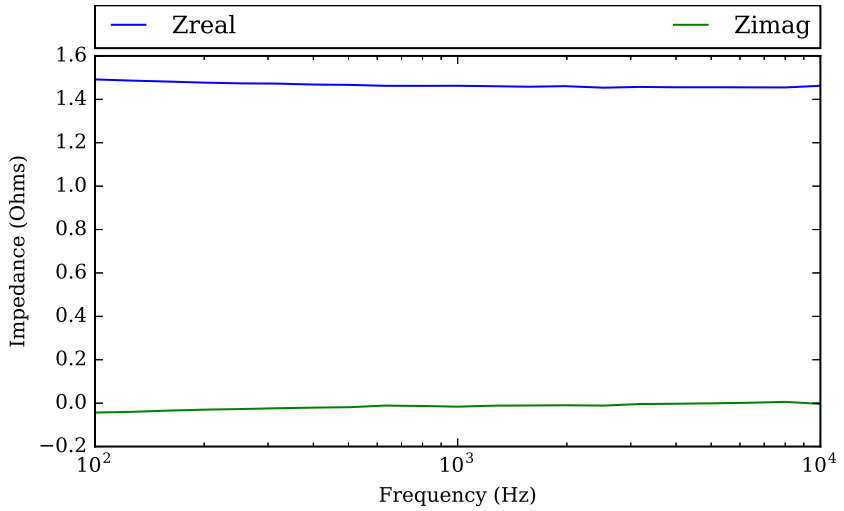

Figure B.7: Real and imaginary components of impedance for an Fe_5Si_3 powder anode in a NaCl-KCl electrolyte.

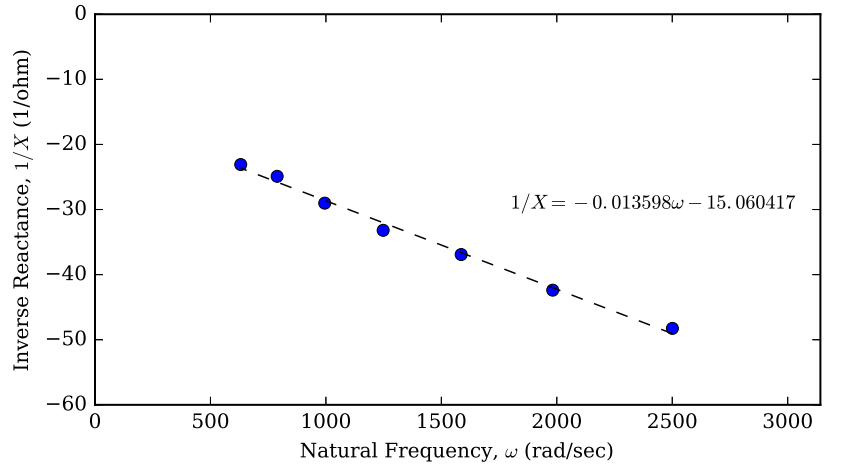

Figure B.8: Plot of inverse reactance (1/X) versus natural frequency for an Fe_5Si_3 powder anode in a NaCl-KCl electrolyte (surface area = 737 cm^2). Slope is capacitance.

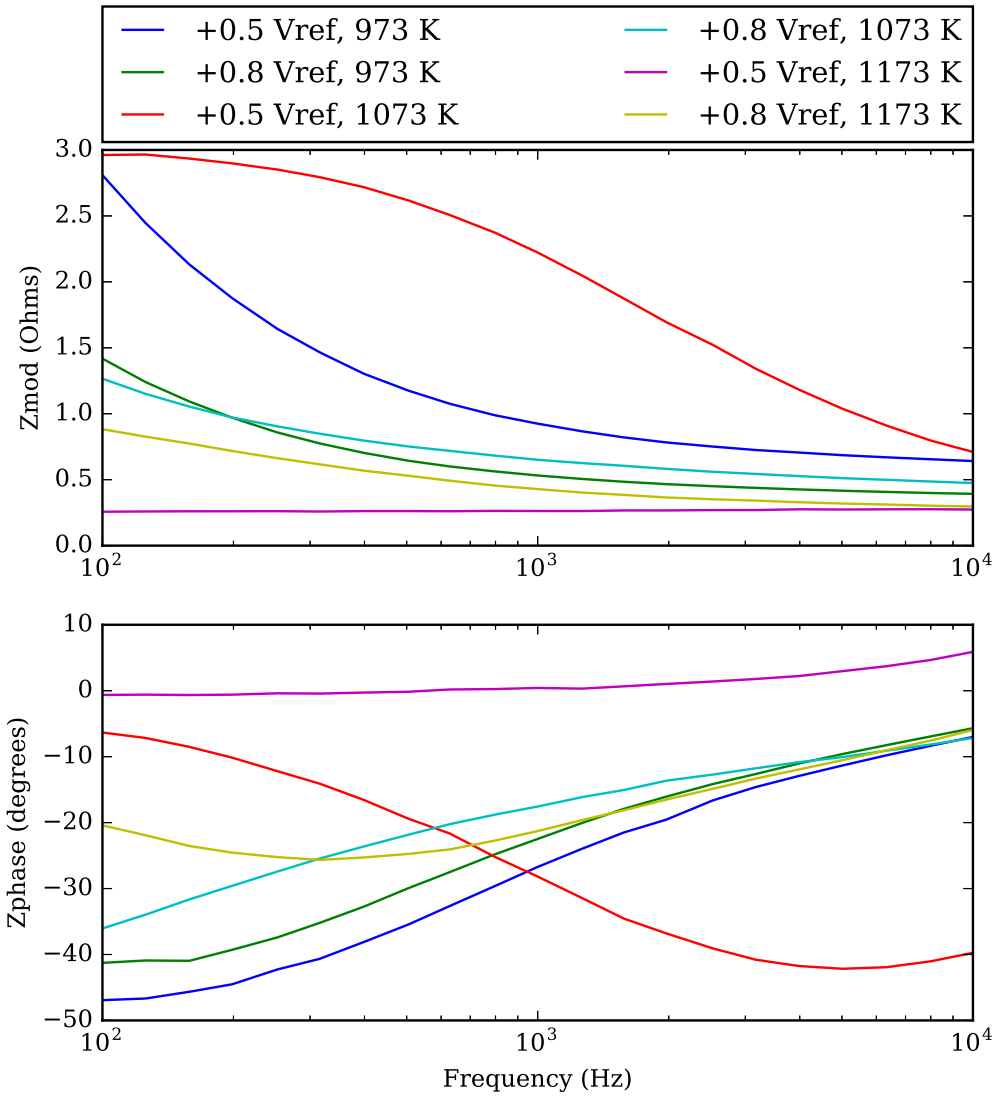

Figure B.9: Bode plot for EIS data for t = 1.5 hours.

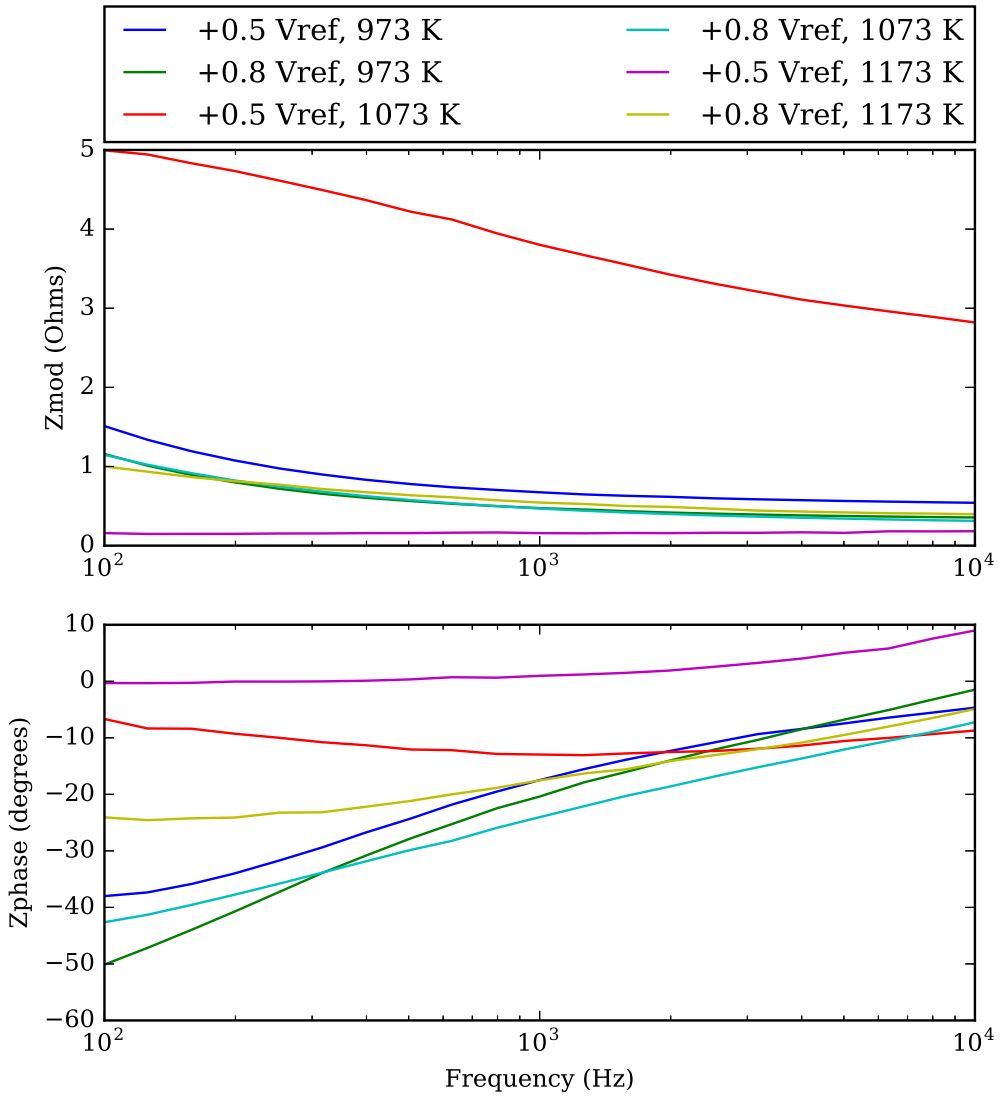

Figure B.10: Bode plot for EIS data for t = 3.0 hours.

Appendix C

Cost of Titanium Production by the MER Process

The true cost of titanium production by the MER process would be the result of a number of factors, including capital costs to build the reactor, labor costs, the design of the reactor, and the exact process parameters. However, rough estimates of the cost of production (and CO_2 intensity) of titanium production by the MER process can be made by making a few general assumptions:

- All heating in the process is done by electrical means.
  - Heat for oxycarbide production produced using electrically-heated furnace.
  - Heat for molten salt is provided by ohmic heating from electrolysis.
- Product gases of the chemical reactions are lost and not recycled.
- Titanium feedstock prices are based on spot prices for 2016 [29].
- Cost of electricity (and associated CO_2 generation) are based on the national average for 2015 [80].

  - Electricity generation is 35% efficient with respect to fuel input [81].

- None of the molten salt electrolyte is lost over time.
- Inert gas losses are negligible.
- All processes yields are 100%.

In addition, we need to make some additional assumptions about the processes themselves:

- All process inputs start at room temperature, and end at process temperature:
  - Process temperature of titanium oxycarbide reduction reaction assumed to be 1873 K.
  - Molten salt reactor temperature assumed to be 1073 K.
  - In the case of titanium oxycarbide purification, the inputs for subsequent titanium electrolysis are also at 1073 K.
- A stoichiometric amount of carbon is used as a reductant.
- The electrochemical reactions are assumed to have a current efficiency of 65%.
  - Full-cell potential of the titanium plating reaction is assumed to be 2 volts.
  - Full-cell potential of the iron-removal reaction is assumed to be 1 volt.

In the cases where pitch was used as the reductant, adjustments needed to be made to the mass balance:

- Pitch was assumed to be a long-chain hydrocarbon compound ($C_{16}H_{34}$, as this was the heaviest n-alkane for which enthalpy data was readily available).
- Based on prior experiments, only 45% of pitch (by mass) is converted to solid carbon. The rest volatilizes into hydrogen and lighter alkanes. Thus, approximately 2.2 times as much pitch needs to be used.

– For the mass balance, the volatile pitch byproduct gases are assumed to be methane and hydrogen gas at 1073 K.

The process energy required for titanium oxide reduction (to titanium oxycarbide) are based on the enthalpy changes between the input reactants and products. For the electrolysis step, the input energy is assumed to be due to the electrolysis only (the ohmic heating is higher than the enthalpy change of the reaction, so excess heat is available to keep the salt at temperature).

Using these assumptions, we can obtain a rough estimate of the cost and CO_2 intensity of titanium production for rutile or ilmenite as the input titanium feedstock, and carbon black or pitch as the reductant. This information is summarized in Table C.1, and each case is detailed in Tables C.2 through C.5. This analysis shows that despite the extra processing that ilmenite mineral sand requires to produce pure titanium oxycarbide, titanium produced from ilmenite is cheaper than titanium produced from rutile. However, the analysis also shows that titanium produced using pitch as a reductant for titanium oxycarbide production will be more expensive than if carbon black was used. Despite the fact that pitch is cheaper than carbon black, the increase in cost is due to the fact that more pitch needs to be used in the carbothermal reduction process as most of the carbon in pitch is lost to volatilization.

Table C.1: Cost and CO_2 intensity of titanium production by the MER process with rutile and carbon black as feedstock.

Estimated Cost of Production (USD/kg Ti)

	Rutile	Ilmenite
Carbon Black	2.29	1.87
Pitch	2.68	2.28

Estimated CO_2 Emissions (kg CO_2/kg Ti)

	Rutile	Ilmenite
Carbon Black	5.32	7.97
Pitch	9.37	12.80

Table C.2: Cost and CO_2 intensity of titanium production by the MER process with rutile and carbon black as feedstock.

Oxycarbide formation, Energy requirement	12743 kJ/kg Ti
	3.5 kWh/kgTi
Oxycarbide formation, Direct CO_2 emissions	1.38 kg CO_2/kg Ti
Titanium electrolysis, Energy requirement	3.4 kWh/kg Ti
Titanium electrolysis, Direct CO_2 emissions	0.46 kg CO_2/kg Ti
Total electricity required	6.98 kWh/kg Ti
CO_2 intensity of electricity generation [80]	0.50 kg CO_2/kWh
CO_2 emissions from electricity generation	3.48 kg CO_2/kg Ti
TOTAL CO_2 EMISSIONS	5.32 kg CO_2/kg Ti
Rutile spot price [29]	725 USD/tonne rutile
	1.27 USD/kg Ti
Carbon black price [82]	1.10 USD/kg carbon
	0.50 kg carbon/kg Ti
	0.55 USD/kg Ti
Electricity price [80]	0.00675 USD/kWh
	0.47 USD/kg Ti
TOTAL COST OF Ti	2.29 USD/kg Ti

Table C.3: Cost and CO_2 intensity of titanium production by the MER process with ilmenite and carbon black as feedstock.

Oxycarbide formation, Energy requirement	19117 kJ/kg Ti
	5.3 kWh/kgTi
Oxycarbide formation, Direct CO_2 emissions	2.30 kg CO_2/kg Ti
Iron removal (electrolysis), Energy requirement	1.7 kWh/kg Ti
Iron removal (electrolysis), Direct CO_2 emissions	0 kg CO_2/kg Ti
Titanium electrolysis, Energy requirement	3.4 kWh/kg Ti
Titanium electrolysis, Direct CO_2 emissions	0.46 kg CO_2/kg Ti
Total electricity required	10.48 kWh/kg Ti
CO_2 intensity of electricity generation [80]	0.50 kg CO_2/kWh
CO_2 emissions from electricity generation	5.22 kg CO_2/kg Ti
TOTAL CO_2 EMISSIONS	7.97 kg CO_2/kg Ti
Ilmenite spot price [29]	105 USD/tonne rutile
	0.33 USD/kg Ti
Carbon black price [82]	1.10 USD/kg carbon
	0.75 kg carbon/kg Ti
	0.83 USD/kg Ti
Electricity price [80]	0.00675 USD/kWh
	0.71 USD/kg Ti
TOTAL COST OF Ti	1.87 USD/kg Ti

Table C.4: Cost and CO_2 intensity of titanium production by the MER process with rutile and pitch as feedstock.

Oxycarbide formation, Energy requirement	18634 kJ/kg Ti
	5.2 kWh/kgTi
Oxycarbide formation, Direct CO_2 emissions	2.99 kg CO_2/kg Ti
Titanium electrolysis, Energy requirement	3.4 kWh/kg Ti
Titanium electrolysis, Direct CO_2 emissions	0.46 kg CO_2/kg Ti
Total electricity required	6.98 kWh/kg Ti
CO_2 intensity of electricity generation [80]	0.50 kg CO_2/kWh
CO_2 emissions from electricity generation	4.29 kg CO_2/kg Ti
TOTAL CO_2 EMISSIONS	7.75 kg CO_2/kg Ti
Rutile spot price [29]	725 USD/tonne rutile
	1.27 USD/kg Ti
Pitch price*	0.75 USD/kg pitch
	1.11 kg pitch/kg Ti
	0.83 USD/kg Ti
Electricity price [80]	0.00675 USD/kWh
	0.58 USD/kg Ti
TOTAL COST OF Ti	2.68 USD/kg Ti

* Based on correspondence with a representative at Koppers, Inc. Price of pitch varies between 600-800 USD/tonne, with an additional 50 USD/tonne for solid pitch.

Table C.5: Cost and CO_2 intensity of titanium production by the MER process with ilmenite and pitch as feedstock.

Oxycarbide formation, Energy requirement	18923 kJ/kg Ti
	5.3 kWh/kgTi
Oxycarbide formation, Direct CO_2 emissions	4.72 kg CO_2/kg Ti
Iron removal (electrolysis), Energy requirement	1.7 kWh/kg Ti
Iron removal (electrolysis), Direct CO_2 emissions	0 kg CO_2/kg Ti
Titanium electrolysis, Energy requirement	3.4 kWh/kg Ti
Titanium electrolysis, Direct CO_2 emissions	0.46 kg CO_2/kg Ti
Total electricity required	10.42 kWh/kg Ti
CO_2 intensity of electricity generation [80]	0.50 kg CO_2/kWh
CO_2 emissions from electricity generation	5.19 kg CO_2/kg Ti
TOTAL CO_2 EMISSIONS	10.37 kg CO_2/kg Ti
Ilmenite spot price [29]	105 USD/tonne rutile
	0.33 USD/kg Ti
Pitch price*	0.75 USD/kg pitch
	1.66 kg pitch/kg Ti
	1.25 USD/kg Ti
Electricity price [80]	0.00675 USD/kWh
	0.70 USD/kg Ti
TOTAL COST OF Ti	2.28 USD/kg Ti

* Based on correspondence with a representative at Koppers, Inc. Price of pitch varies between 600-800 USD/tonne, with an additional 50 USD/tonne for solid pitch.

Bibliography

[1] H Sibum et al. "Titanium, titanium alloys, and titanium compounds". In: *Ullmann's Encyclopedia of Industrial Chemistry*. Vol. 37. Wiley-VCH, 2012, pp. 51–82. DOI: 10.1002/14356007.a27_095.

[2] Gerhard Auer et al. "Pigments , Inorganic , 2. White Pigments". In: *Ullmann's Encyclopedia of Industrial Chemistry, Electronic Release*. Weinheim: Wiley-VCH, 2012, pp. 257–291. DOI: 10.1002/14356007.n20.

[3] Toru H Okabe and Yoshio Waseda. "Producing titanium through an electronically mediated reaction". In: *JOM* 49.6 (1997), pp. 28–32. DOI: 10.1007/BF02914710.

[4] Derek J. Fray, George Zheng Chen, and Tom W. Farthing. "Direct electrochemical reduction of titanium dioxide to titanium in molten calcium chloride". In: *Nature* 407.6802 (2000), pp. 361–364. DOI: 10.1038/35030069.

[5] Carsten Schwandt. "Understanding the electro-deoxidation of titanium dioxide to titanium metal via the FFC-Cambridge process". In: *Mineral Processing and Extractive Metallurgy* 122.4 (2014), pp. 213–218. DOI: 10.1179/0371955313Z.00000000071.

[6] EHK Technologies. *Summary of Emerging Titanium Cost Reduction Technologies*. Vancouver, WA, 2004. ISBN: 3608960031.

[7] Ryosuke O. Suzuki, Katsutoshi Ono, and Koh Teranuma. "Calciothermic reduction of titanium oxide and in-situ electrolysis in molten CaCl2". In: *Metallurgical and Materials Transactions B* 34.3 (2003), pp. 287–295. DOI: 10.1007/s11663-003-0074-1.

[8] PC Pistorius and DJ Fray. "Formation of silicon by electro-deoxidation, and implications for titanium metal production". In: *The Journal of The South African Institute of Mining and Metallurgy* 106.1 (2006), pp. 31–42. ISSN: 0038-223X.

[9] L. L. Benson, I. Mellor, and M. Jackson. "Direct reduction of synthetic rutile using the FFC process to produce low-cost novel titanium alloys". In: *Journal of Materials Science* 51.9 (2016), pp. 4250–4261. DOI: 10.1007/s10853-015-9718-1.

[10] James C Withers and Raouf O Loutfy. *Thermal and electrochemical process for metal production*. US Patent Application 10/828,641. 2001. URL: https://www.google.com/patents/US20050166706.

[11] James C Withers and Raouf O Loutfy. *Thermal and electrochemical process for metal production*. US Patent Application 11/294,872. 2006. URL: https://www.google.com/patents/US20060237327.

[12] James C. Withers, R. O. Loutfy, and J. P. Laughlin. "Electrolytic process to produce titanium from TiO2 feed". In: *Materials Technology* 22.2 (2007), pp. 66–70. DOI: 10.1179/175355507X214078.

[13] James C Withers, John P Laughlin, and Raouf O Loutfy. "The Production of Titanium from a Composite Anode". In: *Innovations in Titanium Technology*. 2007, pp. 117–125. ISBN: 978-0-87339-665-3.

[14] James C Withers and Raouf O Loutfy. *Thermal and electrochemical process for metal production*. US Patent Application US 11/536,599. 2007. URL: https://www.google.com/patents/US20070029208.

[15] James C Withers et al. "Recent Improvements for Electrowinning Titanium Metal from Composite Anodes". In: *International Round Table on Titanium Production in Molten Salts*. 2008, pp. 1–5.

[16] James C Withers and Raouf O Loutfy. *Thermal and electrochemical process for metal production*. US Patent 7,985,326 B2. 2011. URL: https://www.google.com/patents/US7410562.

[17] Ole S. Kjos, Geir Martin Haarberg, and Ana Maria Martinez. "Titanium Production from Oxycarbide Anodes". In: *ECS Transactions*. Vol. 16. 49. 2009, pp. 229–237. DOI: 10.1149/1.3159327.

[18] Ole Sigmund Kjos, Geir Martin Haarberg, and Ana Maria Martinez. "Electrochemical Production of Titanium from Oxycarbide Anodes". In: *Key Engineering Materials* 436 (2010), pp. 93–101. DOI: 10.4028/www.scientific.net/KEM.436.93.

[19] Ana Maria Martinez et al. "New Method for Low-Cost Titanium Production". In: *Key Engineering Materials* 436 (2010), pp. 41–53. DOI: 10.4028/www.scientific.net/KEM.436.41.

[20] Derek J Fray and Shuqiang Jiao. *Treatment of titanium ores*. US Patent 9,181,604. 2015. URL: https://www.google.com/patents/US9181604.

[21] Shuqiang Jiao and Hongmin Zhu. "Novel metallurgical process for titanium production". In: *Journal of materials research* 21.09 (2006), pp. 2172–2175.

[22] Chengjun Gao et al. "Preparation of titanium oxycarbide from various titanium raw materials: Part I. Carbothermal reduction". In: *Rare Metals* 29.6 (2010), pp. 547–551. DOI: 10.1007/s12598-010-0166-4.

[23] Xiaohui Ning et al. "Preparation of Titanium Deposit in Chloride Melts". In: *Metallurgical and Materials Transactions B* 42.6 (2011), pp. 1181–1187. DOI: 10.1007/s11663-011-9559-5.

[24] BN Popov et al. "Electrochemical behaviour of titanium (II) and titanium (III) compounds in molten lithium chloride/potassium chloride eutectic melts". In: *Journal of Applied Electrochemistry* 21 (1991), pp. 351–357. DOI: 10.1007/BF01020221.

[25] T.P. Boyarchuk, E.G. Khailova, and V.L. Cherginets. "Potentiometric measurements in molten chlorides. Solubilities of metal oxides in the molten eutectic mixture CsCl-KCl-NaCl at 600°C". In: *Electrochimica Acta* 38.10 (1993), pp. 1481–1485. DOI: 10.1016/0013-4686(93)80086-F.

[26] ARPA-E. *Modern Electro/Thermochemical Advances in Light Metal Systems (METALS) FOA (DE-FOA-0000882)*. 2013. URL: https://arpa-e-foa.energy.gov/Default.aspx?Archive=1#FoaId7494c8b3-e88e-48f2-b4c8-e4c093bbe077.

[27] K J Stanaway. "Overview of titanium dioxide feedstocks". In: *Min. Eng.* 46.12 (1994), pp. 1367–1379. ISSN: 00265187.

[28] Thomas P. Battle, Dat Nguyen, and James W. Reeves. "The processing of titanium-containing ores". In: 1 (1993), pp. 925–943.

[29] U.S. Geological Survey. *USGS Mineral Commodity Summaries*. Washington DC, 2017. URL: http://minerals.usgs.gov/minerals/pubs/mcs/.

[30] Zhanmin Cao et al. "Critical Evaluation and Thermodynamic Optimization of the Ti-C-O System and Its Applications to Carbothermic TiO2 Reduction Process". In: *Metallurgical and Materials Transactions B* 46.4 (2015), pp. 1782–1801. DOI: 10.1007/s11663-015-0344-8.

[31] J.B. Farrow, I.M. Ritchie, and P. Mangano. "The reaction between reduced ilmenite and oxygen in ammonium chloride solutions". In: *Hydrometallurgy* 18 (1987), pp. 21–38. DOI: 10.1016/0304-386X(87)90014-4.

[32] Hong Yong Sohn. "Process Modeling in Non-Ferrous Metallurgy". In: *Treatise on Process Metallurgy: Industrial Processes, Part A*. Ed. by Seshadri Seetharaman. Elsevier, 2013. Chap. 2.4, pp. 758–771. ISBN: 9780080969886.

[33] D.R. Burgess. *Thermochemical Data*. Ed. by P.J. Linstrom and W.G. Mallard. URL: http://webbook.nist.gov.

[34] C.W. Bale et al. "FactSage thermochemical software and databases, 2010–2016". In: *Calphad* 54 (2016), pp. 35–53. DOI: 10.1016/j.calphad.2016.05.002.

[35] Xiaohui Ning et al. "Dissolution behavior of TiC x O 1-x solid solutions in chloride melt". In: *Electrochemistry* 78.6 (2010), pp. 513–516.

[36] *ASTM B265: Standard Specification for Titanium and Titanium Alloy Strip, Sheet, and Plate*. 2015. DOI: 10.1520/B0265-15.

[37] S. N. Flengas and T. R. Ingraham. "Voltaic Cells in Fused Salts: Part I. The Silver - Silver Chloride, Cobalt - Cobaltous Chloride System". In: *Canadian Journal of Chemistry* 35.10 (1957), pp. 1139–1149. DOI: 10.1139/v57-154.

[38] J. Guion et al. "Thermodynamic treatment and electromotive force measurements of the ternary molten salt systems silver chloride-sodium chloride-potassium chloride and silver chloride-sodium chloride-cesium chloride". In: *The Journal of Physical Chemistry* 72.6 (1968), pp. 2086–2095. DOI: 10.1021/j100852a035.

[39] B Eichler. "Aufbau und Wirkungsweise der Ag/AgCl, KCl-NaCl/SUPREMAX/...-Bezugselektrode in äquimolarer KCl-NaCl-Schmelze". In: *Chemischer Informationsdienst* 3.26 (1972), pp. 195–201.

[40] Angela Altomare et al. "QUALX2.0 : a qualitative phase analysis software using the freely available database POW_COD". In: *Journal of Applied Crystallography* 48.2 (2015), pp. 598–603. DOI: 10.1107/S1600576715002319.

[41] G Neumann, R Kieffer, and P Ettmayer. "Über das System TiC-TiN-TiO". In: *Monatshefte für Chemie* 103.4 (1972), pp. 1130–1137. DOI: 10.1007/BF00905189.

[42] Caroline A Schneider, Wayne S Rasband, and Kevin W Eliceiri. "NIH Image to ImageJ: 25 years of image analysis". In: *Nature Methods* 9.7 (2012), pp. 671–675. DOI: 10.1038/nmeth.2089.

[43] Ian E. Grey and John A. Watts. "Mineralogical Nomenclature: Pseudorutile Revalidated and Neotype Given". In: *Mineralogical Magazine* 58.393 (1994), pp. 597–600. DOI: 10.1180/minmag.1994.058.393.07.

[44] A Mücke and J.N. Bhadra Chaudhuri. "The continuous alteration of ilmenite through pseudorutile to leucoxene". In: *Ore Geology Reviews* 6.1 (1991), pp. 25–44. DOI: 10.1016/0169-1368(91)90030-B.

[45] Petrus Christiaan Pistorius and C Coetzee. "Physiochemical Aspects of Titanium Slag Production and Solidification". In: 34.5 (2003), pp. 581–588. DOI: 10.1007/s11663-003-0027-8.

[46] Krzysztof Borowiec et al. *Method to Upgrade Titania Slag and Resulting Product*. US Patent 5,830,420. 1998. URL: https://www.google.com/patents/US5830420.

[47] Stephen E. Haggerty. "Oxide Mineralogy of the Upper Mantle". In: *Reviews in Mineralogy and Geochemistry* 25.1 (1991), pp. 355–416. ISSN: 1529-6466.

[48] Farzin Fatollahi-Fard and Petrus Christiaan Pistorius. "Production of Titanium Oxycarbide from Titania-Rich Mineral Sands". In: *EPD Congress (TMS 2015)*. 2015, pp. 297–304. DOI: 10.1002/9781119093503.ch34.

[49] Nathalie Lebrun. "Carbon - Iron - Silicon". In: *Iron Systems, Part 5*. Ed. by Günter Effenberg and Svitlana Ilyenko. Vol. 11D5. Landolt-Börnstein - Group IV Physical Chemistry. Berlin, Heidelberg: Springer Berlin Heidelberg, 2009, pp. 1–18. ISBN: 978-3-540-70885-8. DOI: 10.1007/978-3-540-70890-2.

[50] Vancliff Johnson et al. "Magnetic and Mössbauer effect studies of Mn5Si3:Fe5Si3 solid solutions". In: *Journal of Solid State Chemistry* 4.2 (1972), pp. 311–323. DOI: 10.1016/0022-4596(72)90122-3.

[51] O Kubaschewski. "Fe-Si (Iron - Silicon)". In: *ASM Handbook - Volume 3: Alloy Phase Diagrams*. Ed. by F.C. Campbell. Vol. 3. ASM International, 1992, pp. 2.194–2.207. ISBN: 0-87170-381-5. URL: http://products.asminternational.org/hbk/do/section/content/V03/D02/A22/s0038825.htm.

[52] Farzin Fatollahi-Fard and Petrus Christiaan Pistorius. "Production of Titanium Oxycarbide from Iron-Rich Titanium Ores". In: *Extraction and Powder Production (Ti-2015: The 13th World Conference on Titanium)*. 2015, In Press, CD–ROM.

[53] "Al2O3-MgO-SiO2". In: *Slag Atlas*. Dusseldorf: Verlag Stahleisen, 1995, pp. 113–114.

[54] M.L. de Vries, I.E. Grey, and J.D. Fitz Gerald. "Crystallographic Control in Ilmenite Reduction". In: *Metallurgical and Materials Transactions B* 38.2 (2007), pp. 267–277. DOI: 10.1007/s11663-006-9015-0.

[55] John Hugh Chesters. *Refractories: Production and Properties*. London: Iron and Steel Institute, 1973, p. 553.

[56] Kôichirô Kôyama, Yasuhiko Hashimoto, and Hidekazu Hata. "Phase Relationship in the V-C-O Ternary System". In: *Transactions of the Japan Institute of Metals* 20.7 (1979), pp. 371–376. DOI: 10.2320/matertrans1960.20.371.

[57] E.T. Turkdogan, R.G. Olsson, and J.V. Vinters. "Pore characteristics of carbons". In: *Carbon* 8.4 (1970), pp. 545–564. DOI: 10.1016/0008-6223(70)90016-3.

[58] T. Coetsee, P.C Pistorius, and E.E de Villiers. "Rate-determining steps for reduction in magnetite-coal pellets". In: *Minerals Engineering* 15.11 (2002), pp. 919–929. DOI: 10.1016/S0892-6875(02)00120-6.

[59] RG Becher et al. "A new process for upgrading ilmenitic mineral sands". In: *Australasian Inst Mining Met Proc* 214.June (1965), pp. 21–44.

[60] Farzin Fatollahi-Fard and Petrus Christiaan Pistorius. "Upgrading of Iron-Rich Titanium Minerals Using a Molten Salt Process". In: *7th International Symposium on High-Temperature Metallurgical Processing (TMS 2016)*. 2016, pp. 19–26. DOI: 10.1002/9781119274643.ch3.

[61] Donald Fergusson Stewart and Leslie John Pollard. *Process for Producing Metallic Iron Concentrates and Titanium Oxide Concentrates from Titaniferous Ores*. US Patent 3,816,099. 1974. URL: https://www.google.com/patents/US3816099.

[62] Donald Fergusson Stewart and Leslie John Pollard. *Process of Beneficiating Titaniferous Ores in the Presence of Hydrogen Chloride*. US Patent 3,854,929. 1974. URL: https://www.google.com/patents/US3854929.

[63] Leslie John Pollard and Donald Fergusson Stewart. *Beneficiation of the Non-Ferrous Metal Values of Oxide-Containing Materials*. US Patent 4,047,934. 1977. URL: https://www.google.com/patents/US4047934.

[64] Tetsuo Ishitsuka and Koichi Nose. "Stability of protective oxide films in waste incineration environment—solubility measurement of oxides in molten chlorides". In: *Corrosion Science* 44.2 (2002), pp. 247–263. DOI: 10.1016/S0010-938X(01)00059-2.

[65] Farzin Fatollahi-Fard and Petrus Christiaan Pistorius. "Electrochemical Upgrading of Iron-rich Titanium Ores". In: *Molten Slags, Fluxes, and Salts 2016: Proceedings of the 10th International Conference (MOLTEN16)*. 2016, Accepted.

[66] Kevin J. Leary. *Molten salt electrolytic beneficiation of iron oxide-containing titaniferous ores to produce iron and high-grade TiO2*. US Patent 5,194,124. 1993. URL: https://www.google.com/patents/US5194124.

[67] T. Sasaki, M. Watanabe, and Y. Fujiki. "Structure of K1.0Ti8O16 and K0.0Ti8O16". In: *Acta Crystallographica B* 49.5 (1993), pp. 838–841. DOI: 10.1107/S0108768193004677.

[68] Sang-Eun Chun and J.F. Whitacre. "The evolution of electrochemical functionality of carbons derived from glucose during pyrolysis and activation". In: *Electrochimica Acta* 60 (2012), pp. 392–400. DOI: 10.1016/j.electacta.2011.11.082.

[69] Adrián A Vega and Roger C Newman. "Nanoporous Metals Fabricated through Electrochemical Dealloying of Ag-Au-Pt with Systematic Variation of Au:Pt Ratio". In: *Journal of the Electrochemical Society* 161.1 (2013), pp. C1–C10. DOI: 10.1149/2.003401jes.

[70] Dietrich Stauffer. *Introduction to Percolation Theory*. London: Taylor & Francis, 1985. ISBN: 0-85066-315-6.

[71] Jacques Lacaze and Bo Sundman. "An assessment of the Fe-C-Si system". In: *Metallurgical Transactions A* 22.10 (1991), pp. 2211–2223. DOI: 10.1007/BF02664987.

[72] RV Andrews. "Solving Conductive Heat Transfer Problems with Electrical-Analogue Shape Factors". In: *Chemical Engineering Progress* 51.2 (1955), pp. 67–71. URL: http://www.osti.gov/scitech/biblio/4382113.

[73] K Matiašovský et al. "Electrical conductivity of molten LiCl-NaCl-KCl and LiCl-NaCl-KCl-AlCl3 mixtures". In: *Chemické Zvesti* 34.4 (1980), pp. 433–440. URL: http://www.chempap.org/index.php?id=7&paper=4979.

[74] MM Yovanovich. "Dimensionless shape factors and diffusion lengths of three-dimensional bodies". In: *Proceedings of the ASME/JSME Thermal Engineering Joint Conference*. Vol. 1. 1995, pp. 103–114. URL: http://www.mhtl.uwaterloo.ca/pdf_papers/mhtl95-8.pdf.

[75] M. Yovanovich, P. Teertstra, and J. R. Culham. "Modeling transient conduction from isothermal convex bodies of arbitrary shape". In: *Journal of Thermophysics and Heat Transfer* 9.3 (1995), pp. 385–390. DOI: 10.2514/3.678.

[76] Adolf Kisza. "The capacitance of the electric double layer of electrodes in molten salts". In: *Journal of Electroanalytical Chemistry* 534.2 (2002), pp. 99–106. DOI: 10.1016/S0022-0728(02)01148-8.

[77] Adolf Kisza. "The capacitance of the diffuse layer of electric double layer of electrodes in molten salts". In: *Electrochimica Acta* 51.11 (2006), pp. 2315–2321. DOI: 10.1016/j.electacta.2005.03.093.

[78] W. G. Pollard and R. D. Present. "On Gaseous Self-Diffusion in Long Capillary Tubes". In: *Physical Review* 73.7 (1948), pp. 762–774. DOI: 10.1103/PhysRev.73.762.

[79] R Byron Bird, Warren E Stewart, and Edwin N Lightfoot. "Diffusivity and the Mechanisms of Mass Transport". In: *Transport Phenomena*. 2nd ed. New York: John Wiley & Sons, Inc., 2007. Chap. 17, pp. 513–542. ISBN: 978-0-470-11539-8.

[80] U.S. Energy Information Administration. *Electricity - Data*. URL: https://www.eia.gov/electricity/data.cfm.

[81] T.E. Norgate, S. Jahanshahi, and W.J. Rankin. "Assessing the environmental impact of metal production processes". In: *Journal of Cleaner Production* 15 (2007), pp. 838–848. DOI: 10.1016/j.jclepro.2006.06.018.

[82] ICIS. *Indicative Chemical Prices A-Z*. URL: https://www.icis.com/chemicals/channel-info-chemicals-a-z/ (visited on 05/02/2017).